STRUCTURE-DEPENDENT ELECTRONIC PROPERTIES OF OXIDES FROM FIRST PRINCIPLES

BY YUANJUN ZHOU

A dissertation submitted to the

Graduate School—New Brunswick

Rutgers, The State University of New Jersey

in partial fulfillment of the requirements

for the degree of

Doctor of Philosophy

Graduate Program in Physics and Astronomy

Written under the direction of

Professor Karin M. Rabe

and approved by

_____

_____

_____

_____

_____

New Brunswick, New Jersey

October, 2015

ABSTRACT OF THE DISSERTATION

Structure-dependent electronic properties of oxides from first principles

by Yuanjun Zhou

Dissertation Director: Professor Karin M. Rabe

This thesis contains several investigations on the structure dependent electronic properties of oxides, studied via first-principle calculations or tight-binding models. We start by reviewing the background of structure correlated properties and functionalities in transition metal oxides, followed by the introduction of the density functional theory which will be used throughout this thesis. We next consider the spin-phonon coupling effect for $SrMnO_3/LaMnO_3$ superlattice with epitaxial strain. We explain the origin of the intriguing emergence of the large spin-phonon coupling effect for tensile strain. As the study of superlattice goes on, we realize the emergent need of a systematic way to determine the ground state structure for superlattices. Thus we develop the "stacking method" to solve this problem, and test it using $PbTiO_3/SrTiO_3$ whose structure is known to be complicated. We then use the stacking method for the further study on epitaxially strained $SrCrO_3/SrTiO_3$ superlattice, and find a nonpolar-polar structural transition along with a metal-insulator transition. We conclude that the polar structure induces an orbital ordering, leading to the insulating state. We also study the interband transition effect in the epitaxially strained $SrVO_3$, and show that the suppressed interband transitions lead to the significant transmittance for $SrVO_3$ thin films. Finally we

define the surface polarization effect for those surfaces where in-plane inversion symmetry is broken. We extend the Berry-phase theory of the bulk polarization to the case of surface polarization by formulating the problem in the hybrid Wannier representation. The surface polarization is in agree with the accumulating charge at the common edge of two facets as expected.

Acknowledgements

It has been six years since I came to Rutgers. I just do not realize it because the period feels to me even shorter than my college time. However, it is a long time. I have seen the changes of the University, new president of the University, new chairmen and directors of our program, those new buildings in Livingston campus; I have seen many friends leaving here for graduation or getting new positions; I have changed my address five times; I have tried every Chinese restaurant within 40 miles; and, I have become a husband. I met a lot of great people during the time at Rutgers, and there are many names in my mind that I want to acknowledge.

I am very grateful to Professor Karin Rabe, for her scientific guidance and support during my PhD study. From Karin I learned knowledge, ways of doing research and most importantly the scrupulous and prudent attitude towards research. Each discussion with Karin is very delightful and inspiring that I always feel that I do not have change to discuss with her every day. I thank Karin also for her help and patience when I was looking for postdoc positions. It is, and always will be, my honor to be her student.

I also want to thank Professor David Vanderbilt for his helpful and inspiring suggestions, advice and ideas, from group meetings, lectures and discussions. Also I appreciate the the opportunity he gave me to collaborate with him for the surface polarization paper. He is very organized and intelligent and it feels excellent to work with him.

Before I joined Karin's group, I started my PhD research at Rutgers in Professor Eva Andrei's group. During the one-year study, I learned a lot on nanostructure fabrications and transport measurement. I want to thank Prof. Andrei for her guidance in my research and the opportunity she gave me to carry out experiments in the National High Magnetic Field Laboratory. Also I would like to thank Guohong Li, Ivan Skachko, Adina Luican-Meyer in Eva's group for their help.

I would like to thank Professor Kristjan Haule because he agreed to put an iMac, which is under his grant, in my office. That makes me much more convenient in research.

I thank my PhD dissertation committees, Prof. Premala Chandra, Prof. Jolie Cizewski, Prof. Daniel Friedanfor their patience and valuable questions and advices during the committee meetings.

Thanks go to directors of the graduate program, Prof. Ronald Ransome, Prof. Ted Williams, Prof. Jolie Cizewski, and Prof. Ronald Gilman. They gave me kind advices to finish the program and helped me a lot for courses registration.

I thank Shirley Hinds and Frances DeLucia for their help in sorting out all the administrative forms and arranging all the committee meetings for me.

My researches cannot be performed without simulations, and I want to thank our computer cluster for the unlimited computation time and thank Viktor Oudovenko for making good maintenance to the cluster and helping me solve software problems.

I sincerely thank a lot of professors and senior colleagues, Prof. Marivi Fernandez-Serra, Prof. Donald Harman, Prof. Premala Chandra, Prof. Mathew Dawber, Prof. Roman Engel-Herbert, Dr. Joseph, Bennett, Dr. Kevin Garrity, Dr. Hongbin Zhang, Dr. Sergey Artyukhin, Dr. Se Young Park, Dr. Jialan Zhang, Dr. Yanpeng Yao and Dr. Jiawang Hong, with whom those enlightening discussions helped me a lot.

I always owe my parents, for their love and support on me, and for their encouragements during these years.

Thanks go to my wife Jie Liu, she worked hard to get the admission from Rutgers, making us live together after a four-year relationship over the Pacific Ocean. Thanks for her company and encouragements.

Finally I want to thank all of my friends at Rutgers, Wenhu Xu, Qibin Zhou, Sebastian Reyes-Lillo, Wei Dai, Xueyun Wang, Zhexun Sun, Bin Gao, Can Xu, Yixin Xu, Zhan Li, Juan Wei, Wenbo Wang, Jianpeng Liu, He Chen, for the help they offered, and for the happiness we shared together.

Table of Contents

List of Tables

List of Figures

Chapter 1

Introduction

Transition metal oxides (TMOs) [1, 2] are the subject of extensive research in condensed matter physics. They exhibit a range of correlated phenomena due to the complex interplay between the charge, spin and orbital degrees of freedom. The nature of the interplay is dependent on the structure of the material, as illustrated in Fig. 1.1. Various correlated electronic phases are not only fundamental in physics, but can also be used for applications. Colossal magnetoresistance, ferroelectricity, high T_c superconductivity, various orbital orders, spin orders and charge orders are good examples of correlated electronic phases in TMOs. In addition, tuning the correlated phases may give rise to novel devices. For example, tuning magnetic states may lead to memory devices, and switching the metallic/insulating states may lead to logic devices.

Among TMOs, perovskite is one of the most important classes, and in this thesis perovskite is the prototype system where we study various correlated properties. Perovskite represents the class of compounds that have the $CaTiO_3$ like pseudo-cubic structure and the ABO_3 formula, as shown in Fig. 1.2. Typical perovskites include $SrTiO_3$, $SrVO_3$, $LaMnO_3$. The A site cation is usually an alkaline or a rare earth atom, and the B site cation is usually a transition metal atom whose d shell is not fully filled. The six oxygens nearest to the B site atom form an octahedron. The octahedral crystal field breaks the spherical symmetry of the B atom into an O_h symmetry, and the five d orbitals of the B atom split into doubly degenerated e_g and triply degenerated t_{2g} orbitals, as shown in Fig. 1.3.

Perovskites are of particular interests for several reasons. First, as a typical transition metal oxide, many remarkable phenomena and functional properties that have been observed in perovskites[3, 4] need to be understood for condensed matter physics from

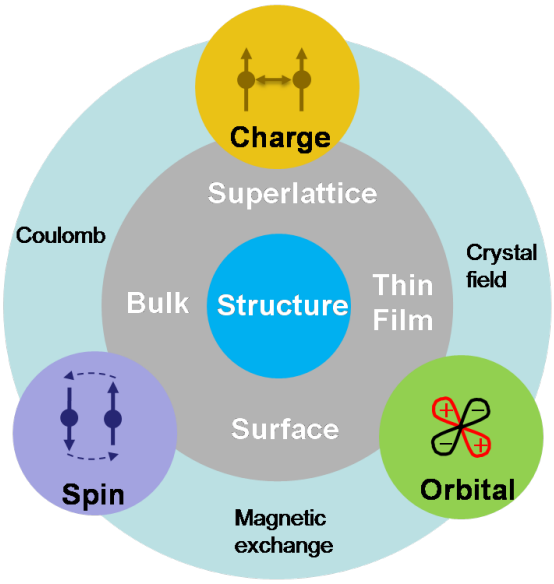

Figure 1.1: Complex interplay of charge, spin, and orbital, associated with different structures for transition metal oxides.

the fundamental point of view. For example, colossal magnetoresistance, spin-phonon coupling effect, piezoelectricity, ferroelectricity, multiferroic effects, metal-insulator transitions that have been found in perovskites all attract tremendous interests. The rich properties are related to the d shell electrons of the B site atom. Partially filled d shell may give rise to the magnetic properties. The hopping effect between the d orbital and the O p may lead to the B site displacements relative to the O octahedron, and give rise of ferroelectricity related effects. The localization of d orbitals may induce various strongly correlated properties, and even the Mott metal-insulator transition where the energy levels of two degenerated spins are distinguished by the strong Coulomb repulsion. Charge ordering and orbital ordering are also common reasons for metal-insulator transitions, and both of them are orbital selection effects due to the partially filled d orbitals.

Furthermore, many of these properties are closely related to the structure of the perovskite. The spin-phonon coupling effect occurs in magnetic materials where different magnetic states result in different frequencies for the same phonon displacement

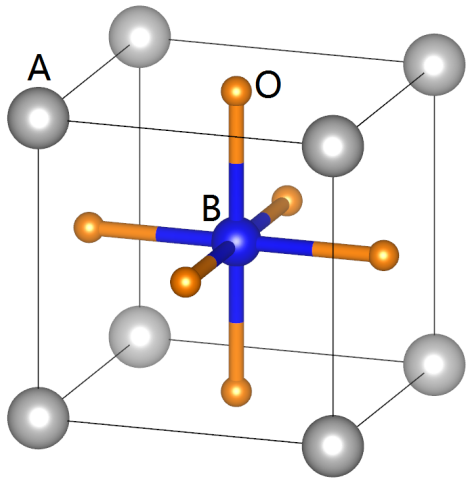

Figure 1.2: A cubic ABO_3 perovskite unit cell.

pattern. The coupling strength can be further coupled to structural changes, for example, epitaxial strain. Piezoelectricity broadly exists in insulators without inversion symmetry, and is a linear interaction between mechanical stress and electronic charge accumulation. Ferroelectricity is associated with a spontaneous polar distortion of the crystalline structure, and can be switched to the negative polar state that is symmetrically equivalent. Multiferroics are defined as materials that exhibit more than one primary ferroic order parameter simultaneously, usually ferroelectricity with magnetic ordering. Metal-insulator transitions can result from many mechanisms, including structural distortions. For instance, the Jahn-Teller (JT) distortion, which is associated with the local bond length changes between the B site atom and O, occurs to lift the degeneracy of t_{2g} or e_g orbitals when they are partially occupied, possibly leading to a metal-insulator transition, with the formation of orbital ordering or charge ordering. Oxygen octahedral rotations will change the B atom-oxygen bond angles, and thus $d-p$ band widths near the Fermi level, and possibly induce a metal-insulator transition.

There are currently many ways to systematically tune the structure of a perovskite. Thus, it is possible to engineer the functional properties and design novel devices. The synthesis of bulk perovskites are now well developed and high quality single crystals

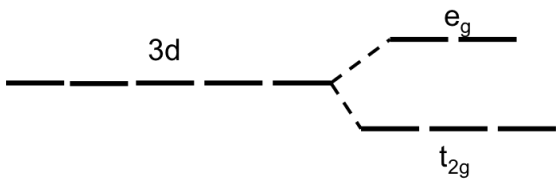

Figure 1.3: The $e_g - t_{2g}$ splitting of 3d orbitals in octahedral crystal field.

have been routinely grown for years[5, 6]. Substituting or doping the cations is one of the most convenient ways to change the structure of a bulk perovskite by changing the ionic radii tolerance factor. The ionic radii tolerance factor is defined as $t = \frac{r_A + r_0}{\sqrt{2}(r_B + r_0)}$, where r_A, r_B and r_0 represent the radii of the A site, B site cation and O anion, respectively. Usually for a perovskite the tolerance factor $0.71 < t < 1$. When $0.9 < t < 1$ the structure tends to be cubic or tetragonal. When $0.71 < t < 0.9$, the structure tends to be orthorhombic or rhombohedral, meaning oxygen octahedral rotations are preferred. Other tuning parameters such as pressure, temperature are also effective at driving bulk perovskites through structrual phase transitions, and further tuning the electronic properties.

Different structures and properties exist in other states of perovskites. Perovskites can also be synthesized using the atomic size layered growth methods such as Pulsed laser deposition (PLD) and Molecular beam epitaxy (MBE)[7]. Electronic properties of layered structures including thin films and superlattices can be significantly different from their bulk state because of the two-dimensional confinement effect. Moreover, for these epitaxial methods, large scale epitaxial strain can be addressed due to the lattice mismatch between epitaxial layers and substrates. Epitaxial strain has recently become an important tuning parameter for structural changes in thin films and superlattices, and it leads to many exotic phases and electronic properties that are not as easily accessible for the bulk state. Examples include the epitaxial strain coupled multiferroic state[8, 9] and metal-insulator transition[10].

Superlattices recently attract a great deal of attention. They are a class of periodic layered structures, exhibiting many degrees of freedom that can be tuned for novel

properties. Obviously, the charge transfer, and correlations between the constituents may give rise to novel properties, especially at the interface[11, 12]. Also, the epitaxial strain effect, compositional tuning of both A and B sites cations, and layering or confinement effects may dramatically change the crystalline and electronic structures of a superlattice.

These degrees of freedom make superlattices a great innovative platform for the design of new functional materials. On the other hand, the synthesis of superlattice is time consuming and the degrees of freedom make it difficult for experimentalists to decide the composition and epitaxial strain required for realizing desirable properties. First-principles calculations can be used to accelerate the process of materials searching, particularly in the sphere of complex oxide systems. In modern condensed matter physics, first-principles studies play an important role: they connect theoretical formalisms to experiments. Density Functional Theory (DFT) is widely used for first-principles calculations in solid state physics. It is a successful approach to access many-body problems in real materials. As will be introduced in the next chapter, DFT calculations do not make assumptions of models and fitting parameters. They start from the fundamental many-body quantum physics of electrons and atoms in a crystal. Thus, first-principles calculations can directly compare with and explain the experimental results, and in addition, they provide the possibility to design novel materials. By varying the chemical and structural complexity, first-principles calculations may easily assess hypothetical materials (superlattices, thin films) or well-known materials under extreme conditions (high pressure, large epitaxial strain) that have not been studied. Reasonable calculations from first-principles provide good evidence or hints for experimentalists. Recently this type of theory-experiment collaboration has been more successful. Multiferroics due to epitaxial strain[13, 8] and hybrid improper ferroelectrics are good examples[14] that were predicted by first-principles studies first and then realized by experiments. This is one reason why the US government launched the Materials Genome Initiative, to utilize the computational resources and first principles studies to at least double the current speed of new material discovery. In this thesis, DFT is mainly used to study the structural, electronic, magnetic and optical properties

of perovskites for their strained bulk and superlattice states.

In this thesis I focus on both the structures and coupled properties of epitaxial strain on different perovskites and their heterostructures using first-principles methods. I also describe the fundamental formalism of surface polarization. Chapter 2 reviews the basic theoretical background. The results and discussions are contained in Chapter 3 to 7.

In Chapter 3 I will discuss the spin-phonon coupling effect in the 1:1 $SrMnO_3/LaMnO_3$ superlattice. Spin-phonon couplings have recently been the subject of active experimental and theoretical interest, especially with the discovery of a novel multiferroic phase in $EuTiO_3$ resulting from spin-phonon coupling for a low-frequency polar mode. Artificial structuring, specifically superlattice layering, is well known to affect crystal structure, magnetic ordering and phonons, and therefore could also in principle be used to enhance spin-phonon coupling. In this Chapter, I use first-principles methods to study magnetic ordering and spin-phonon coupling in a 1:1 SMO/LMO superlattice with varying epitaxial strain. Having found the magnetic phase transitions in agreement with previous work, we investigate the epitaxial strain effects on spin-phonon couplings, and find that the character of the lowest polar mode can be changed in tensile strain, leading to a substantial increase of the spin-phonon coupling. This work shows the possibility of enhancing spin-phonon coupling in magnetic perovskite oxides by combining superlattice layering with epitaxial strain tuning, providing an approach to tailoring functional materials. This work has been published on the Physical Review B[15].

During the study of superlattices, we realize the clear need for an efficient method to determine the ground state and low-energy alternative structures of superlattices. Methods of structural determination for superlattices that are commonly used are computationally formidable phonon-based distortion freeze in and relaxations or conjectures from the ground state structures for bulk constituents. In Chapter 4, a method based on a simple strategy – to generate starting structures based on low-energy structures of the constituent compounds, which are then optimized via structural relaxation calculations – is proposed. This "stacking method" is demonstrated on the 2:2 $PbTiO_3/SrTiO_3$ superlattice, which has been the subject of recent experimental and theoretical interest. Our work shows the success and efficiency of the stacking method in determination of

the ground state and alternative low energy states of the PTO/STO superlattice. This method can be implemented as an automatic process and easily generalized for different combinations of superlattices, paving the way for future superlattice studies. This work has been published on Physical Review B[16].

With the development of the stacking method in Chapter 4, I will use it to determine the ground state structures of $SrCrO_3/SrTiO_3$, a dielectric/metallic superlattice for different epitaxial strain and the interplay of magnetic states in Chapter 5. In this Chapter, I perform and analyze first-principles calculations on a 1:1 superlattice of two perovskite oxides: $SrCrO_3$, a d^2 system with competing phases, and the d^0 incipient ferroelectric $SrTiO_3$. We show that the superlattice layering has a dramatic effect on the Cr d-bands near the Fermi level. We also show that with increasing tensile epitaxial strain, a first order transition occurs between a nonpolar metallic state and a polar insulating state. It is the coupling of the polar distortion in the $SrCrO_3$ layer to the superlattice d-bands that lifts the degeneracy of d_{yz} and d_{xz} orbitals and leads to the insulating state. These results demonstrate a new mechanism for metal-insulator transitions driven by polar distortions, beyond the particular example of $SrCrO_3/SrTiO_3$. This is of particular interest in the design of novel functional materials for electric-field control of the conductivity and of the band gap, and should attract the attention of both theorists and experimentalists working on materials design and discovery. This work has been published on Physical Review Letter[17].

Thin films are another type of heterostructure. Unlike the superlattice, there is no out-of-plane periodicity. The thickness of a thin film can range from sub-nanometer (monolayer) to micrometer. In this thesis when I refer to thin films, I will merely consider the thickness from nanometers to tens of nanometers. This means that my research of thin films does not focus on surface effects. Since there are at least tens of atomic layers, the "bulk" properties actually dominate. Nonetheless, the epitaxial strain plays an important role for thin films. Thus I use the "strained bulk" to investigate the properties of thin film in the thesis. Our experimental colleagues found that the thin films of $SrVO_3$ are of decent transparency. With the conducting $SrVO_3$ film, by comparing the transparency and meanwhile the conductivity, they found that the thin

film of $SrVO_3$ had a superior performance than the widely used indium tin oxides for the transparent conductor. In Chapter 6 I will introduce our theoretical study on the interband transitions of $SrVO_3$, showing that it is the key for the small absorption within the visible light range. This work has been submitted.

At surfaces of a crystal, the electronic properties can be quite different from the bulk due to the broken symmetry at the surface, which usually leads to surface relaxations and reconstructions. Besides the superlattice first principles studies, my research also includes the formal study of the surface effect. We realize that at the surface where the in-plane inversion symmetry is broken, an in-plane polarization localized at the surface should be expected even if the bulk is nonpolar due to the centrosymmetric lattice. The Berry phase theory has been well-established for the bulk polarization. However, the surface polarization effect has not yet been studied, and the terminology is often confused with the dipole density that is localized and perpendicular to the surface. It is remarkable that such a fundamental concept as surface polarization has been overlooked until now. Probably the reason is that it only results in line charges at facet edges, which are harder to observe than the surface charges resulting from the parent phenomenon of bulk polarization. Nevertheless, it seems very likely that experimental probes now have the sensitivity to detect such line charges. These effects can occur in a broad range of insulating materials systems, and can also be associated with domain walls, twin and grain boundaries, and interfaces. Thus, we believe that a proper understanding of surface polarization and its consequences will become essential when trying to understand the electrostatics of nanostructures at near-atomic length scales. In Chapter 7 I will define and discuss the surface polarization and edge charge effect in the language of Berry phase theory and show our results of tight-binding model studies. This work has been published on Physical review B Rapid Communication[18].

Chapter 2

Introduction to Methods

In this chapter I first introduce the basic theoretical background of Density Functional Theory (DFT) and its extension, Hubbard U method, used throughout the thesis. Then the phonons, structural relaxation, and polarization calculations based on DFT are reviewed.

2.1 Density functional theory

2.1.1 Energy functional and Kohn-Sham equation

For an N electrons system, the many-body Hamiltonian H can be described as,

$$H(\mathbf{R},\mathbf{r}) = T_N(\mathbf{R}) + T_e(\mathbf{r}) + V_{NN}(\mathbf{R}) + V_{ee}(\mathbf{r}) + V_{eN}(\mathbf{r},\mathbf{R}), \tag{2.1}$$

In which $T_N(\mathbf{R})$, $T_e(\mathbf{r})$ represent the kinetic energies for nuclei and electron, respectively, while $V_{NN}(\mathbf{R})$, $V_{ee}(\mathbf{r})$ and $V_{eN}(\mathbf{R},\mathbf{r})$ denote the Coulomb potential energies for nuclei-nuclei, electron-electron, and nuclei-electron interactions, respectively. $\mathbf{R}$ and $\mathbf{r}$ are the position coordinates for nuclei and electrons. Considering the Born-Oppenheimer approximation and the large nuclei masses, the kinetic energy of nuclei, T_N, can be treated as a perturbation. The rest terms can be written as

$$T_e(\mathbf{r}) = -\frac{\hbar^2}{2m}\sum_i \frac{\partial^2}{\partial \mathbf{r}_i^2}, \tag{2.2}$$

$$V_{NN}(\mathbf{R}) = -\frac{e^2}{2m}\sum_{I\neq J} \frac{Z_I Z_J}{|\mathbf{R}_I - \mathbf{R}_J|}, \tag{2.3}$$

$$V_{ee}(\mathbf{r}) = -\frac{e^2}{2m}\sum_{i\neq j} \frac{1}{|\mathbf{r}_i - \mathbf{r}_j|}, \tag{2.4}$$

$$V_{eN}(\mathbf{r},\mathbf{R}) = -e^2 \sum_{iI} \frac{Z_I}{|\mathbf{r}_i - \mathbf{R}_I|}. \tag{2.5}$$

where Z is the charge of nuclei, i, I label electrons and nuclei, and m is the mass of the electron.

To directly solve the many-body problem in a crystal, the number of Schrödinger equations need to be solved are of the formidable order of 10^{23}.

Hohenberg and Kohn [19] showed that the total energy of the ground state of an interacting electronic system is a unique functional of the electron density electronic density. Although no practical solution was provided in this paper, the theorem of Hohenberg and Kohn inspires the approaches of density functionals that circumvent the large number of Schrödinger equations.

Following the previous paper, Kohn and Sham [20] provided a method to proceed further. In this idea, the original many-body electron problem is replaced by a fictitious one-electron problem. In this framework, the density of the system is given by the one-electron wavefunction $\psi_i(\mathbf{r})$,

$$n(\mathbf{r}) = \sum_i |\psi(\mathbf{r})|^2. \tag{2.6}$$

Hence the total energy functional can be given by

$$E_{KS}[\psi_i] = -\frac{1}{2m}\sum_i \langle\psi_i|\,\nabla^2\,|\psi_i\rangle + \frac{1}{2}\int \frac{n(\mathbf{r})n(\mathbf{r}')}{|\mathbf{r}-\mathbf{r}'|}d\mathbf{r}d\mathbf{r}' + \int V_{ext}(\mathbf{r})n(\mathbf{r})d\mathbf{r} + E_{NN} + E_{xc}[n(\mathbf{r})]. \tag{2.7}$$

It is the so-called Kohn-Sham energy functional, and the minimum value is equal to the ground state energy of the many-body system. The first term in E_{KS} is the one-electron kinetic energy, the second term is the classical Coulomb energy expressed in the electron density, namely the Hartree term, the third term is the potential energy of electrons in the external field created by the ions, the fourth term is the Coulomb energy between ions, and the last term is the exchange and correlation energy. All the differences between the real many-body total energy and the one-electron total energy is included in the E_{xc} term.

To determine the wave functions that minimize the Kohn-Sham energy functional, we use the variational method on ψ_i with the orthonormal constraint $\langle\psi_i|\psi_j\rangle = \delta_{ij}$ and

that gives the Kohn-Shame equation:

$$\left[-\frac{\hbar^2}{2m}\nabla^2 + V_H(\mathbf{r}) + V_{ext}(\mathbf{r}) + V_{xc}(\mathbf{r})\right]\psi_i(\mathbf{r}) = \epsilon_i\psi_i(\mathbf{r}), \tag{2.8}$$

where ψ_i is the wave function of electronic state, ϵ_i is the Kohn-sham eigenvalue, V_H is the Hartree potential with the expression:

$$V_H(\mathbf{r}) = e^2\int\frac{n(\mathbf{r}')}{|\mathbf{r}-\mathbf{r}'|}d\mathbf{r}'. \tag{2.9}$$

The V_{ext} term in Eq. (2.8) is the external potential, and the V_{xc} is the exchange-correlation potential given by

$$V_{xc}(\mathbf{r}) = \frac{\delta E_{xc}[n(\mathbf{r})]}{\delta n(\mathbf{r})}. \tag{2.10}$$

Once the explicit expression of E_{xc} or V_{xc} is known, the Kohn-Sham equation can be calculated self-consistently. Then the exact total energy would be given as

$$E_0 = \sum_i \epsilon_i - \frac{e^2}{2}\int\frac{n(\mathbf{r})n(\mathbf{r}')}{|\mathbf{r}-\mathbf{r}'|}d\mathbf{r}d\mathbf{r}' + E_{xc}[n(\mathbf{r})] - \int V_{xc}(\mathbf{r})n(\mathbf{r})d\mathbf{r}. \tag{2.11}$$

2.1.2 Approximations of exchange-correlation funtionals

Given the basis of the DFT in the previous subsection, the exact expression of the term of E_{xc} is not available. Approximations of it are required to really solve the problem. The local density approximation (LDA) [20] is the simplest and one of the most successful approximations. The LDA assumes that the exchange-correlation energy at position $\mathbf{r}$ is equal to the exchange-correlation energy per electron $\varepsilon_{xc}(n)$ in a homogeneous electron gas with the density $n(\mathbf{r})$ that is equal to the real system:

$$E_{xc}^{LDA}[n(\mathbf{r})] = \int\varepsilon_{xc}(n(\mathbf{r}))n(\mathbf{r})d\mathbf{r}, \tag{2.12}$$

and

$$\frac{\delta E_{xc}^{LDA}[n(\mathbf{r})]}{\delta n(\mathbf{r})} = \frac{\partial[n(\mathbf{r})\varepsilon_{xc}(\mathbf{r})]}{\partial n(\mathbf{r})}. \tag{2.13}$$

The exchange-correlation energy functional is purely local in the LDA. Several parametrization works [21, 22] use interpolation formulas to link results for the exchange-correlation energy of electron gases. The LDA generally ignores the inhomogeneities in

the electron density, but it turns out to have predicted very successful results. It has been shown that this can be partially due to the correct sum rule for the exchange-correlation hole that is included in the LDA [23, 24].

There are many attempts to improve the exchange-correlation functional. For example, generalized gradient approximation (GGA) [25] includes the gradient expansion terms, and meta-GGA takes a dependence on the kinetic energy density on the Laplacian of the wavefunctions into account. Other approximations exist that consider more terms and effects. They may have better performances than the LDA in particular cases, but overall the accuracy is not dramatically improved.

2.1.3 Practical implementations.

Plane waves are commonly used as a basis set for the electronic wave functions, after the Fourier transforms, the Kohn-Sham equations can be written as

$$\sum_{\mathbf{G}'} \left[\frac{\hbar^2}{2m} |\mathbf{k}+\mathbf{G}|^2 \delta_{\mathbf{G}\mathbf{G}'} + V_H(\mathbf{G}-\mathbf{G}') + V_{ext}(\mathbf{G}-\mathbf{G}') + V_{xc}(\mathbf{G}-\mathbf{G}') \right] c_{i,\mathbf{k}+\mathbf{G}'} = \epsilon_i c_{i,\mathbf{k}+\mathbf{G}}. \tag{2.14}$$

The sum over $\mathbf{G}'$ is finite in practice, and it is determined by the "cutoff" energy

$$|\mathbf{k}+\mathbf{G}| < G_{cut}, \tag{2.15}$$

where $\frac{\hbar^2}{2m} G_{cut}^2 = E_{cut}$. This means that the number of plane waves can be easily controlled by the cutoff energy. It is one of the reasons that the plane-wave based DFT softwares are in more widely used. In this thesis all the first-principles calculations are performed using the *Vienna Ab initio Simulation Package* (VASP-5.2)[26, 27].

Another important step to carry out DFT is the k-point sampling. For each $\mathbf{k}$ point the Kohn-Sham equations are solved, and the Kohn-Sham eigen-energy ϵ_i should be integrated over the Brillouin zone. The infinite number of k points in Brillouin zone represent the infinite number of electrons in the solid according to the Bloch's theorem. However, to carry out the DFT calculation we cannot and do not necessary to calculate the the infinite number of k points, because the wavefunctions tend to be smooth in the k space. Instead, we usually use a equally spacing k mesh to sample the Brillouin zone, and the integration over the Brillouin zone becomes a summation over the finite

k points. The denser the k mesh, the more accurate the calculation. Usually the cutoff energy and the k point mesh are determined by checking the convergence of the total energy beforehand.

When using the plane wave basis set to expand the electronic wave functions, a large number of plane waves are needed to expand the core orbitals to express the fast oscillations. The all-electron calculation is usually believed to be relatively accurate but slow due to the huge number of plane waves used.

The pseudopotential approximation largely reduces the number of plane waves. By assuming the electronic properties are mainly determined by the valence electrons, the pseudopotential for the valence electrons are constructed. The corresponding pseudo wave functions are identical to the real wave functions outside the core region and smooth inside without radial nodes. The pseudo wave functions are built to be smooth at the core region boundary and of the same scattering properties with the all-electron wave functions.

The earliest pseudopodential type is norm conserving[28]. It requires the equality of the squared amplitudes of the real and pseudo wave functions inside the core region. It is convenient in some calculations associated with summing the electron density in the core region, but it is relatively expensive when calculate the localized orbitals such as the rare earth and 3d elements for which large sets of plane waves are needed. Vanderbilt developed the ultrasoft pseudopotential[29], in which the norm conserving requirement is relaxed to further lower the number of plane waves. The price is a local charge term for the valence charge consistency.

Another important development is the projector augmented-waves (PAW) pseudopotentials [30, 31]. The PAW method combines the ideas from the pseudopotential and the linearized augmented-plane-wave (LAPW). It gives small cutoff energies for most of the elements and also the accuracy of the all electron calculation. All the first-principle calculations in this thesis are based on the PAW potentials.

2.1.4 Beyond DFT

DFT + Hubbard U. The DFT, or more specifically LDA and GGA often fail in transition

metal oxides due to an inadequate description of the strong Coulomb repulsion between d or f electrons localized on metal ions. The DFT with Hubbard U (DFT+U) method [32, 33, 34] assumes that the strongly correlated d or f electrons that can be described in a tight-binding basis are subject tot on-site quasiatomic interactions. The Hubbard parameter U is defined as

$$U = E(d^{n+1}) + E(d^{n-1}) - 2E(d^n), \tag{2.16}$$

in which $E(d^n)$ means the energy that n d orbitals are occupied. So, the Hubbard U indicates the Coulomb energy cost to place two electrons at the same site.

DFT+U method is quite successful in dealing with magnetic and strongly correlated systems. Additionally, the DFT+U does not increase the computational cost significantly comparing to the original DFT, leading to its wide-range use. In this thesis, the DFT+U is the main method I use for the magnetic systems.

2.2 Phonon calculation

A phonon is a vibrational mode in crystals. With the harmonic approximation, it is a property of the second derivative of the total energy.

$$E(u) = E_0 + \sum_{\mathbf{R},i} \frac{\partial E}{\partial u(\mathbf{R})_i} u(\mathbf{R})_i + \frac{1}{2} \sum_{\mathbf{R},\mathbf{R}',j,k} \frac{\partial^2 E}{\partial u(\mathbf{R})_j \partial u(\mathbf{R}')_k} u(\mathbf{R})_j u(\mathbf{R}')_k + o(u^3), \tag{2.17}$$

where $u(\mathbf{R})_i$ denotes the displacements of the ion with equilibrium position $\mathbf{R}$ in i. In matrix notation, the equations of motion are given by

$$M\ddot{\mathbf{u}}(\mathbf{R}) = -\sum_{\mathbf{R}'} \mathbf{C}(\mathbf{R} - \mathbf{R}')\mathbf{u}(\mathbf{R}'), \tag{2.18}$$

where $\mathbf{C}(\mathbf{R} - \mathbf{R}')$ is the force constant matrix, the second derivatives of E with respect to atomic displacements $\mathbf{u}$. With the plane waves solutions $\mathbf{u}(\mathbf{R}, t) = \mathbf{e}e^{i(\mathbf{q}\cdot\mathbf{R} - \omega t)}$, we have

$$M\omega(\mathbf{q})^2\mathbf{e} = \mathbf{C}(\mathbf{q})\mathbf{e}, \tag{2.19}$$

in which the $\tilde{\mathbf{C}}(\mathbf{q})$ is the Fourier transformation of $\mathbf{C}(\mathbf{R})$ into the reciprocal space. It is now an eigenvalue problem to obtain the phonon frequency ω^2.

In first-principles calculations, there are two main methods to compute phonon frequencies. Frozen phonon method is the most straightforward one. In this method, the atoms are rigidly displaced from the equilibrium positions, and forces between other atoms are computed by the Hellmann-Feynman formula. Hence the force constant matrix can be constructed. It can be easily implemented, but for zone boundary $\mathbf{q}$ points, supercell is required since the forces between the atoms in the unit cell and the neighboring unit cell need to be considered.

A more advanced method is based on the density-functional perturbation theory[35, 36]. The first and second derivatives of the ground-state energy read

$$\frac{\partial E}{\partial \lambda_i} = \int \frac{\partial V_\lambda(\mathbf{r})}{\partial \lambda_i} n(\mathbf{r}) d\mathbf{r}, \tag{2.20}$$

$$\frac{\partial^2 E}{\partial \lambda_i \partial \lambda_j} = \int \frac{\partial^2 V_\lambda(\mathbf{r})}{\partial \lambda_i \partial \lambda_j} n(\mathbf{r}) d\mathbf{r} + \int \frac{\partial V_\lambda(\mathbf{r})}{\partial \lambda_i} \frac{\partial n_\lambda(\mathbf{r})}{\partial \lambda_j} d\mathbf{r}. \tag{2.21}$$

Apply this onto the force constant matrix, we have the electronic part

$${}^{el}\tilde{C}_{ij}^{\alpha\beta}(\mathbf{q}) = \frac{1}{N_c}\left[\int \left(\frac{\partial n(\mathbf{r})}{\partial u_i^\alpha(\mathbf{q})}\right)^* \frac{\partial V_{ion}(\mathbf{r})}{\partial u_j^\beta(\mathbf{q})} d\mathbf{r} + \int n(\mathbf{r}) \frac{\partial^2 V_{ion}(\mathbf{r})}{\partial u_i^{\alpha *}(\mathbf{q}) \partial u_j^\beta(\mathbf{q})} d\mathbf{r}\right]. \tag{2.22}$$

Note that there still is an ionic part ${}^{ion}\tilde{C}_{ij}^{\alpha\beta}(\mathbf{q})$ which can be computed analytically that needs to sum up for the total force constant matrix in the reciprocal space[36].

The most important advantage of DFPT in the phonon calculation is circumventing the expensive supercell calculation that comes from to the $O(N^3)$ power law of computational complexity with N the number of atoms in the cell. Now, within DFPT the responses to perturbations of different wavelengths are decoupled, leading to the fairly easy and independent calculation for phonons with arbitrary wave vector $\mathbf{q}$.

To calculate the derivative of the electron charge density in DFPT, we only have to consider the occupied states,

$$(H_0 - \epsilon_v^{\mathbf{k}} + \alpha P_v)\left|\Delta\psi_v^{\mathbf{k}}\right\rangle = -P_c \Delta V_0 \left|\psi_v^{\mathbf{k}}\right\rangle, \tag{2.23}$$

in which only occupied states are considered, and P_v and P_c are project operators to occupied and unoccupied states.

For a specific wave vector $\mathbf{k}+\mathbf{q}$, we project both sides of Eq. 2.23 over the states of $\mathbf{k}+\mathbf{q}$. The projector $P^{\mathbf{k}+\mathbf{q}}$ commutes with H_0, and we denote its action on P_c and P_v with $P^{\mathbf{k}}+\mathbf{q}_c$ and $P^{\mathbf{k}}+\mathbf{q}_v$, respectively. Then Eq. 2.23 becomes

$$(H_0-\epsilon_v^{\mathbf{k}}+\alpha P_v^{\mathbf{k}+\mathbf{q}})\left|\Delta\psi_v^{\mathbf{k}+\mathbf{q}}\right\rangle=-P_c^{\mathbf{k}+\mathbf{q}}\Delta V_0\left|\psi_v^{\mathbf{k}}\right\rangle, \tag{2.24}$$

We can also decompose the perturbing ΔV into Fourier components,

$$\Delta V_0(\mathbf{r})=\sum_{\mathbf{q}}\Delta v_0^{\mathbf{q}}(\mathbf{r})e^{i\mathbf{q}\cdot\mathbf{r}}, \tag{2.25}$$

in which $\Delta v_0^{\mathbf{q}}(\mathbf{r})$ is lattice periodic. Using the periodic parts of the Bloch wave functions $u_v^{\mathbf{k}}$, Eq. 2.24 reads

$$\left(H_0-\epsilon_v^{\mathbf{k}}+\alpha\sum_{v'}\left|u_{v'}^{\mathbf{k}+\mathbf{q}}\right\rangle\left\langle u_{v'}^{\mathbf{k}+\mathbf{q}}\right|\right)\left|\Delta u_v^{\mathbf{k}+\mathbf{q}}\right\rangle=-\left[1-\sum_{v'}\left|u_{v'}^{\mathbf{k}+\mathbf{q}}\right\rangle\left\langle u_{v'}^{\mathbf{k}+\mathbf{q}}\right|\right]\Delta v_0^{\mathbf{q}}\left|u_v^{\mathbf{k}}\right\rangle, \tag{2.26}$$

where v' runs over the valence bands, and $\delta u_v^{\mathbf{k}+\mathbf{q}}$ is the first order correction of the $\mathbf{k}+\mathbf{q}$ component of $u_v^{\mathbf{k}}$. The derivative of electronic density is given by

$$\Delta n_v^{\mathbf{q}}(\mathbf{r})=4\sum_{\mathbf{k}v}\langle u_v^{\mathbf{k}}(\mathbf{r})|\Delta u_v^{\mathbf{k}+\mathbf{q}}(\mathbf{r})\rangle. \tag{2.27}$$

The derivative of electronic density then gives the new self-consistent potential,

$$\Delta v_0^{\mathbf{q}}(\mathbf{r})=\Delta v^{\mathbf{q}}(\mathbf{r})+e^2\int\frac{\Delta n^{\mathbf{q}}(\mathbf{r}')}{|\mathbf{r}-\mathbf{r}'|}e^{-i\mathbf{q}\cdot(\mathbf{r}-\mathbf{r}')}d\mathbf{r}'+\left.\frac{dv_{xc}(n)}{dn}\right|_{n=n(\mathbf{r})}\Delta n^{\mathbf{q}}(\mathbf{r}). \tag{2.28}$$

The Eq. 2.26,2.27,2.28 form a self-consistent loop which is equivalent to the self-consistent calculation of electron charge density $n(\mathbf{r})$. Thus the phonon calculation with arbitrary wave vector can be calculated by DFPT with the same complexity of ground state calculation.

2.3 Structural relaxation

The structural relaxation in this thesis refers to the search of local energy minimization process, in other words, given an starting structure, the local minimum structure with the same symmetry of the starting structure should be found by the structural

relaxation. The relaxation of the ionic positions can be performed according to the Hellmann-Feynman (HF) forces from DFT calculations,

$$F_{i,\alpha} = -\sum_{j} \langle \psi_j | \frac{\partial H}{\partial u_{i,\alpha}} | \psi_j \rangle . \tag{2.29}$$

Here F is the force, and i α and j go over the indices of atoms, components of the force and the band indices, respectively. Having the HF forces, the iterative optimization algorithms such as molecular dynamics and the conjugate gradients methods can be carried out to find the structure with the least forces, leading to a local minimum of the total energy.

The starting structure is thus critical for the structural relaxation. For bulk materials, phonon calculations, especially the unstable phonon modes at high symmetry k points usually provide hints for possible distortions we need to consider. The unstable phonons denote the phonon modes with imaginary frequencies, which means the current structure is a metastable state, and the atomic distortion follow the phonon mode would lower the total energy and lead to a local minimum.

Thus a reasonable approach to determine the distortions in the starting structure is to freeze in the unstable phonon modes. After structural relaxation, the phonon calculation should be performed again to determine the phonon modes that can further lower the total energy from the current local minimum or saddle point. Another commonly used way to determine the ground state structure is to freeze in all the combinations of unstable phonon modes, and select the lowest energy structure after relaxations.

For the structural relaxations of more complex systems such as the superlattice, considerations of pre-processes are necessary to simplify the overall calculation. This will be discussed explicitly as the stacking method in the Chapter 3.

2.4 Modern theory of polarization

The macroscopic polarization is the most essential concept in the description of dielectric properties such as ferroelectricity, piezoelectricity, pyroelectricity, flexoelectricity and so on. The standard model of the macroscopic polarization is based on the Clausius-Mossotti (CM) model, in which the dipole moment in a unit cell is calculated

by the mass centers displacements of the positive and negative charges. However, the absolute polarization in a unit cell is actually useless and ill-defined, and the polarization *differences* should be used to define the polarization. This idea, with formal quantities such as Berry phases and Wannier functions, is developed as the "modern theory of polarization [37]. The modern theory of polarization explains the microscopic picture of polarization, and it also make it accessible in the first-principle calculations.

Universally, the polarization can be given by the integrated current

$$\Delta \boldsymbol{P} = \int_0^{\Delta t} dt \boldsymbol{j}(t) = \boldsymbol{P}(\Delta t) - \boldsymbol{P}(0). \tag{2.30}$$

This quantity is independent of the way of unit cell definition and it has nothing to do with the periodic static charge distribution inside the unit cell.

Hence to calculate the polarization, usually an unpolar high symmetric phase is selected as the reference state with $\Delta \boldsymbol{P} = 0$, and the polarization difference of interested becomes equal to the $\Delta \boldsymbol{P} = \boldsymbol{P}$.

The total polarization consists of the ionic part and the electronic part,

$$\boldsymbol{P} = \boldsymbol{P}_{ion} + \boldsymbol{P}_e. \tag{2.31}$$

The ionic part is contributed from the positive point charges,

$$\boldsymbol{P}_{ion} = \frac{e}{\Omega} \sum_i Z_i^{ion} \boldsymbol{r}_i \tag{2.32}$$

where Ω is the volume of the unit cell, and eZ_i are the positive point charges with positions $\boldsymbol{r}_i$.

The electronic polarization cannot be described directly using the mass centers, but it can be written as a Berry phase of the occupied bands[38]:

$$\boldsymbol{P}_e = \frac{e}{(2\pi)^3} \mathrm{Im} \sum_n \int d\boldsymbol{k} \left\langle u_{n\boldsymbol{k}} \right| \nabla_{\boldsymbol{k}} \left| u_{n\boldsymbol{k}} \right\rangle, \tag{2.33}$$

where n sums over the occupied states and $|u_{n\boldsymbol{k}}>$ are the lattice periodic part of the Bloch wave functions that

$$\left|\psi_{n\boldsymbol{k}}\right\rangle = e^{i\boldsymbol{k}\cdot\boldsymbol{r}} \left|u_{n\boldsymbol{k}}\right\rangle. \tag{2.34}$$

In practice the first-principle calculation is carried out in discrete k-space, which means the integration over $\boldsymbol{k}$ is replaced by a sum over a k-point mesh spanning the Brillouin

zone. In the one-dimensional case, $P_n = (e/2\pi)\phi_n$, where the Berry phase ϕ_n are given as

$$\phi_n = \mathrm{Im} \int dk \, \langle u_{nk} | \, \partial_k \, | u_{nk} \rangle \, . \tag{2.35}$$

But in the discrete k-space it can be written as

$$\phi_n = \mathrm{Im} \ln \prod_{j=0}^{M-1} \left\langle u_{n,k_j} | u_{n,k_{j+1}} \right\rangle , \tag{2.36}$$

where $k_j = 2\pi j/Ma$ gives the jth k-point in the one-dimensional k path. Also, the polarization is only well-defined modulo a quantum of polarization ea/Ω, with e the electronic charge, a the lattice constant along the polarization direction of interest, and Ω the volume of unit cell. A typical value of polarization is below 100 $\mu C/cm^{-2}$. To figure out the quantum factor, a series of polarization calculations are usually performed based on the structures from a non-polar reference state to the polar one with small changes, and a smooth curve of polarization should be obtained that the non-polar structure is origin. The end point of the curve reflects the polarization for the structure of interest.

Chapter 3

Epitaxial strain effects on magnetic ordering and spin-phonon couplings in the $(SrMnO_3)_1/(LaMnO_3)_1$ superlattice from first principles

In this chapter, we have studied the influence of epitaxial strain on magnetic orderings and the couplings between the spin and polar phonons in the 1:1 $SrMnO_3/LaMnO_3$ superlattice from first principles. Magnetic phase transitions of the superlattice induced by epitaxial strain are observed, consistent with previous reports. We find that oxygen octahedral rotations lower the ground state energy but do not destroy the magnetic phase transitions induced by strain. We compute zone center phonon frequencies and eigenvectors as functions of epitaxial strain and magnetic ordering. A substantial increase of the coupling strength between the spin and the lowest-frequency polar mode is observed for tensile strains. This increase can be attributed to a change of character of the lowest mode resulting from different relative couplings of the various polar modes to epitaxial strain. Finally, spin-phonon coupling strengths are computed in a Heisenberg formalism. This analysis directly reveals the changes in exchange couplings due to specific atomic displacements or phonon modes, as well as the nonequivalence of the out-of-plane exchange couplings across LaO layers and across SrO layers, the latter being the result of the artificial structuring in the superlattice.

3.1 Introduction

Spin-phonon coupling is a measure of the dependence of the frequency of a given phonon mode on the magnetic order of the system. It can be determined from experiments measuring the changes of phonon frequencies with magnetic field[39] or as the temperature is varied through a magnetic phase transition[40]. It can be determined more directly

from first-principles calculations of the phonons with the system constrained to various magnetic orderings [41]. While in most materials, this effect is found to be very small, there are a number of exceptions, such as $EuTiO_3$[39, 13]. In fact, as a result of the combination of spin-phonon coupling with epitaxial strain, the antiferromagnetic paraelectric bulk phase of $EuTiO_3$ is transformed to a multiferroic (ferromagnetic and ferroelectric) phase[13, 8]. The search for large spin-phonon coupling and epitaxially induced multiferroicity has been extended to other perovskite compounds[42, 43, 44, 45, 46, 47]. Most notably, $SrMnO_3$ has been found to have large changes in the lowest frequency polar phonon mode with changes in magnetic ordering. [42, 47].

Recent improvements in epitaxial growth methods make it possible to study the physics of high-quality thin films and superlattices, as well as to impose percent level strains by using the mismatch between the substrate and the epitaxial layer[48]. Artificial structuring is well known to have substantial effects on structure, phonon frequencies and eigenvectors and magnetic ordering[49]. Recent work predicting enhancement in spin-phonon coupling in a $CaMnO_3/BaTiO_3$ superlattice[50] shows that interfacial effects and epitaxial strain in a superlattice can also be used to tune the spin-phonon coupling.

The $SrMnO_3/LaMnO_3$ (SMO/LMO) superlattice has attracted a great deal of theoretical and experimental interest[51, 52, 53, 54, 55, 56, 57, 58, 59, 60, 12]. In particular, it has been found that epitaxial strain induces a sequence of magnetic phases[52, 58]. In this chapter, we carry out a detailed first-principles study of the spin-phonon coupling in this system. First, we investigate the epitaxial strain effect on the phase transitions among magnetic orderings in the superlattice system. We find that oxygen octahedral rotations, which were not included in previous studies, lower the ground state energy but do not destroy the magnetic phase transitions induced by strain. We compute zone center phonon frequencies and eigenvectors as functions of epitaxial strain and magnetic ordering. We then focus on the spin-phonon couplings by studying the low-energy magnetic states for a range of epitaxial strains, and report a substantial spin-phonon coupling for large strains. The spin-phonon coupling strengths are computed to describe the spin-phonon coupling effect quantitatively. Our results show the possibility

of tuning spin-phonon coupling using epitaxial strains, paving the way for additional applications of strain engineering in functional oxides.

3.2 Methods

Our calculations were performed using the generalized gradient approximation GGA+U method[61] with the Perdew-Becke-Erzenhof parametrization[62] implemented in the *Vienna Ab initio Simulation Package* (VASP-5.2[26, 27]). We used the Liechtenstein implementation[33] with on-site Coulomb interaction $U = 2.7$ eV and on-site exchange energy $J = 1.0$ eV to describe the localized $3d$ electron states of Mn atoms[43]. The projector augmented wave (PAW) potentials[30, 31] used contain 10 valence electrons for Sr ($4s^2 4p^6 5s^2$), 11 for La ($5s^2 5p^6 6s^2 5d^1$), 13 for Mn ($3p^6 3d^5 4s^2$), and 6 for O ($2s^2 2p^4$).

For structure optimization we used a 500 eV energy cutoff, $\sqrt{2}a_0 \times \sqrt{2}a_0 \times 2a_0$ supercell and $4 \times 4 \times 4$ Monkhorst-Pack(MP) k-meshes with a threshold force of 10^{-3} eV/$\mathring{A}$ on all atoms. To obtain phonon frequencies and eigenvectors we used the frozen phonon method with ionic displacement of 0.02 Åand 600 eV energy cutoff; k-point meshes and supercells depend on the magnetic ordering considered and are specified further below. The effects of epitaxial strain were included within the strained bulk approach, in which the two lattice vectors ($a = a_0(\hat{x} - \hat{y})$ and $b = a_0(\hat{x} + \hat{y})$) that define the (001) substrate-matching plane were held fixed and all other structural parameters relaxed.

Fig. 3.1(a) shows the undistorted 10-atom unit cell of the SMO/LMO superlattice, which has the tetragonal $P4/mmm$ symmetry. We break the symmetry by displacing the atoms as in the $Pnma$ ground state structure of $LaMnO_3$, or $a^-a^-c^+$ in Glazer notation[63], generated by $M_3^+[001]$ and $R_4^+[110]$ antiferrodistortive rotations of the ideal perovskite structure. As can be seen in Fig. 3.1(b), rotation of one octahedron forces opposite rotations of its neighbors in the same plane. In the $M_3^+[001]$ mode the octahedron rotations are identical in neighboring layers, while in R_4^+, shown in Fig. 3.1(c), the rotations alternate layer by layer. The two types of A-site cations lower the symmetry of this distortion from $Pnma$ to $Pmc2_1$, with a $\sqrt{2}a_0 \times \sqrt{2}a_0 \times 2a_0$ supercell.

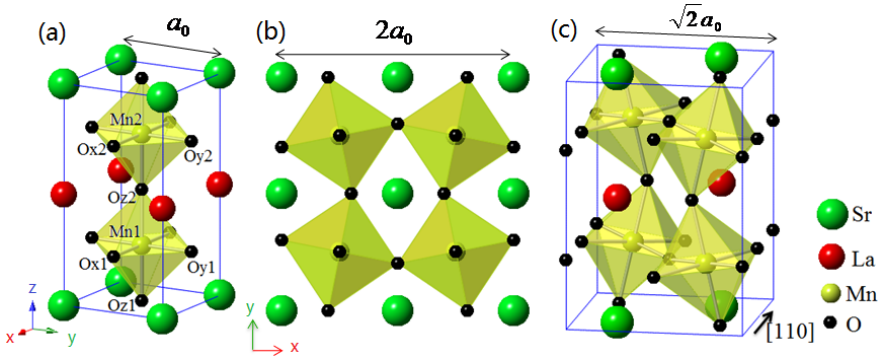

Figure 3.1: (a). View of the 10 atom SMO/LMO unit cell, where Sr, La, Mn, and O atoms are in green, red, yellow and black, respectively. (b). Top view of the rotational distortion $M_3^+[001]$. (c). Side view of the rotation distortion $R_4^+[110]$.

While $Pnma$ is nonpolar, $Pmc2_1$ is a polar space group allowing nonzero in-plane polarization, as the antipolar displacements of the different A-site cations along [110] in general will not cancel each other; insulating superlattice systems with this structure can be characterized as improper ferroelectrics [64, 65, 66].

We consider the following collinear magnetic orderings in this study: FM, C-AFM with ferromagnetically aligned chains of spins along $\hat{z}$, A-AFM with spins in the xy planes ferromagnetically aligned, A-AFM$_y$ with spins in the xz planes ferromagnetically aligned, and the "4-layer" state shown in Fig. 3.2. The phonons for all magnetic orderings were computed for the same $P4/mmm$ reference structure, obtained by relaxing with FM magnetic ordering. The supercells and k-point meshes were chosen as follows: $a_0 \times a_0 \times 2a_0$ supercell and $6\times6\times3$ MP k-mesh for FM state, $\sqrt{2}a_0 \times \sqrt{2}a_0 \times 2a_0$ and $4\times4\times4$ for C-AFM state,$a_0 \times a_0 \times 2a_0$ and $10\times10\times5$ for A-AFM state, $a_0 \times 2a_0 \times 2a_0$ and $6 \times 4 \times 4$ for the A-AFM$_y$ state and $a_0 \times a_0 \times 4a_0$ and $8 \times 8 \times 2$ for the $4-layer$ state. These k-meshes are chosen to achieve convergence of phonon frequencies within 3 cm^{-1} [42].

To quantify the spin-phonon coupling we approximate the total energy as $E = E_0 + E_{ph}^{PM} + E_{spin}$ [42, 41], in which E_0 represents the energy of the undistorted paramagnetic reference structure and $E_{ph}^{PM} = \frac{1}{2}\int dq \sum_{ij\alpha\beta} C_{i\alpha,j\beta}^{PM}(q) u_{i\alpha}(q) u_{j\beta}(q)$, where $C_{i\alpha,j\beta}^{PM}$ are the force constant matrices of a paramagnetic (PM) state with i, j representing the atomic

indices and α, β the displacements along cartesian directions. From here on, we consider only phonons, force constant matrices and atomic displacements with $q = 0$ with respect to the $a_0 \times a_0 \times 2a_0$ cell, and so we drop the explicit dependence on q. The last term in the total energy, $E_{spin} = -\sum_{<ij>} J_{ij} S_i \cdot S_j$, is the energy contributed by nearest neighbor (NN) magnetic exchange interactions. The total force constant matrix for a specific spin configuration is thus given by

$$C_{i\alpha,j\beta} = C^{PM}_{i\alpha,j\beta} - \sum_{<ij>} \frac{\partial^2 J_{ij}}{\partial u_{i\alpha} \partial u_{j\beta}} \langle S_i \cdot S_j \rangle , \tag{3.1}$$

The spin-phonon coupling effect is represented by the nonzero second derivatives of J_{ij} with respect to atomic displacements; these are symmetric matrices denoted by J''_{ij}. Note that the first derivatives of J_{ij} are in general nonzero, corresponding to the spin-lattice couplings in the system[58].

In this study, we investigate the spin-phonon coupling for the lowest-frequency polar mode. For SMO/LMO this is an E_u mode, a two-fold degenerate polar mode with atomic displacements in xy plane. Two Mn atoms are contained in a unit cell, and thus six exchange couplings are considered (see figure 3.2(a)). They are denoted as J''_{1x}, J''_{1y}, J''_{1z}, J''_{2x}, J''_{2y}, J''_{2z}, with the subscripts 1, 2 indexing the Mn atoms in the unit cell, and x, y, z denoting the direction of the exchange coupling. In the SMO/LMO superlattice, the E_u modes are symmetric across mirror planes within the SrO and LaO layers and thus we only need to know the sums $J''_{1x} + J''_{2x}$ and $J''_{1y} + J''_{2y}$; on the other hand, J''_{1z} is distinct from J''_{2z}. To solve for these four J'' matrices and the C^{PM} matrix, five magnetic configurations are needed: FM, A-AFM, C-AFM, A-AFM$_y$, and $4 - layer$, shown in Fig. 3.2(b). For example, in the FM state, $C^F = C^{PM} - S^2 \left[(J''_{1x} + J''_{2x}) + (J''_{1y} + J''_{2y}) + J''_{1z} + J''_{2z} \right]$. Extending this to other four magnetic configurations we obtain

$$\begin{pmatrix} C^F \\ C^A \\ C^C \\ C^A_y \\ C^{4L} \end{pmatrix} = \begin{pmatrix} 1 & -S^2 & -S^2 & -S^2 & -S^2 \\ 1 & -S^2 & -S^2 & S^2 & S^2 \\ 1 & S^2 & S^2 & -S^2 & -S^2 \\ 1 & -S^2 & S^2 & -S^2 & -S^2 \\ 1 & -S^2 & -S^2 & S^2 & -S^2 \end{pmatrix} \begin{pmatrix} C^{PM} \\ J''_{1x} + J''_{2x} \\ J''_{1y} + J''_{2y} \\ J''_{1z} \\ J''_{2z} \end{pmatrix} , \tag{3.2}$$

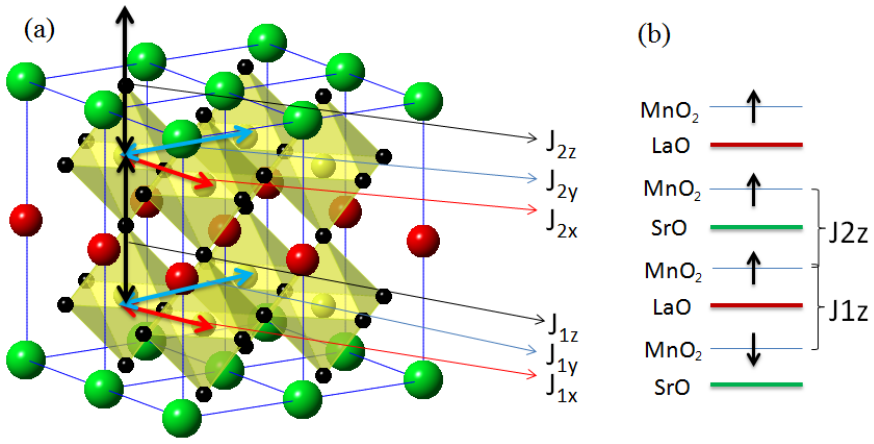

Figure 3.2: (a)The labeling of the spin exchange parameters. (b) The magnetic ordering to calculate $C^{4-layer}$, with J_{1z} and J_{2z} across LaO and SrO layers, respectively. The black arrows in (b) denote spin orientations.

where $S = 1.75$. C^F, C^A, C^C, C^A_y, C^{4L} denote the force constant matrices of FM, A-AFM, C-AFM, A-AFM$_y$ and the 4-layer ordering.

For computing force constant matrices for use in Eq.3.2, we use the supercells for the phonon computations as described above. We displace atoms with $q = 0$ patterns for the $a_0 \times a_0 \times 2a_0$ unit cell, yielding 30×30 "partial" force constant matrices. For example, in order to build C-AFM magnetic ordering we need a $\sqrt{2}a_0 \times \sqrt{2}a_0 \times 2a_0$ supercell containing two Sr atoms. When we calculate derivatives of J matrices with respect to Sr atomic displacements, we move the two Sr atoms in the supercell with the same displacement as in a zone-center distortion in the $a_0 \times a_0 \times 2a_0$ unit cell.

3.3 Results

3.3.1 $Pmc2_1$ structure

In Table 5.1, we report the computed structural parameters for the $Pmc2_1$ structure with magnetic orderings FM, A-AFM and C-AFM. The lowest-energy magnetic ordering is FM. The effective lattice constant $a_0 = (a \cdot b \cdot c)^{1/3}$ in FM, A-AFM, and C-AFM states is 3.894, 3.890 and 3.888 Å, respectively, indicating similar volumes. However, the

Table 3.1: Strain free structural details of SMO/LMO in FM, A-AFM, and C-AFM states. The values of LMO were taken from Ref. [44]
.

	FM	A-AFM	C-AFM
Relative energy(meV/f.u.)	0.0	49.9	140.3
$a_0 = (a \cdot b \cdot c)^{1/3}$ ($\mathring{A}$)	3.894	3.890	3.888
$a_{xy} = \sqrt{a \cdot b}$ ($\mathring{A}$)	3.886	3.930	3.856
$\theta_M(^\circ)$	2.8	0.1	5.1
$\theta_R(^\circ)$	8.2	8.3	7.3
Q_2(a.u.)	0.002	0.000	0.001
$\frac{b}{a} - 1$ (%)	0.5	0.9	0.2
LMO JT Q_2(a.u.)	0.072	0.831	
LMO $\frac{b}{a} - 1$ (%)	0.9	5.2	

FM state prefers a structure close to cubic, as shown by the geometric average of its in-plane lattice constants a_{xy}=3.886Å. A-AFM favors in-plane tensile state (a_{xy}=3.930Å) while C-AFM favors compressive strain (a_{xy}=3.856Å). The different unit-cell shapes for the three spin configurations directly result in strong spin-lattice coupling in the system, as we will see further below.

The incorporation of SMO layers into the superlattice substantially changes the structural parameters relative to those of pure LMO. With respect to the large in-plane orthorhombicity($\frac{b}{a} - 1$) in the ground state structure of $LaMnO_3$, the difference between the two in-plane lattice constants is reduced in SMO/LMO. It is well known that the orthorhombicity in $LaMnO_3$ is due to the strong Jahn-Teller(JT) distortion, quantified here by Q_2. We note that the Q_2 is much smaller in the superlattice than in $LaMnO_3$[44], possibly because the crystal fields of the two types of A-site cations split the degenerate $d_{x^2-y^2}$ and $d_{3z^2-r^2}$ orbitals of Mn atoms and thus suppress the JT distortion. The results for JT distortions are in good agreement with values found in the previous study of SMO/LMO[58].

3.3.2 Spin-lattice coupling and epitaxial-strain phase sequence

Application of epitaxial strain can change the relative energies of phases with different relaxed unit cell shapes and even stabilize non-bulk structures. In the previous subsection we found that the relaxed unit cell shapes for the three magnetic orderings are quite different, implying the existence of significant spin-lattice coupling. Here, we see how this large spin-lattice coupling leads to magnetic phase transitions for accessible epitaxial strains.

We calculate the total energies for FM, A-AFM, and C-AFM ordering in the $Pmc2_1$ structure for a range of epitaxial strains. The phase sequence is plotted in Fig. 3.3. As the strain varies from compressive to tensile, the ground state changes from C-AFM to FM, and then from FM to A-AFM. The epitaxial-strain-induced magnetic phase sequence is the same as that found in previous work[52, 58], where it was explained using the theory of orbital ordering under strain; however, that analysis was carried out assuming the high-symmetry $P4/mmm$ structure. To study the effect of octahedral rotations on the phase boundaries, we carry out the same total energy calculations with epitaxial strain in the space group $P4/mmm$, and plot the phase sequence in Fig. 3.3. The phase boundaries shift relatively little, although the FM phase is slightly wider with octahedral rotations than in the $P4/mmm$ structure.

3.3.3 Spin-phonon coupling

Materials with large spin-lattice couplings can be expected also to have large spin phonon couplings, as in $EuTiO_3$[13] and $SrMnO_3$,[43] both cases reflecting the sensitivity of the magnetic exchange couplings to the crystal structure. In this subsection, we investigate the spin-phonon coupling in the $P4/mmm$ high-symmetry reference structure of the LMO/SMO superlattice as a function of epitaxial strain, focusing on the lowest-frequency polar mode since its sensitivity to changes in epitaxial strain is of the most interest.

First we carry out Γ point phonon calculations for FM, C-AFM and A-AFM orderings in the $P4/mmm$ structure at 0% epitaxial strain. With the 10-atom unit cell, there

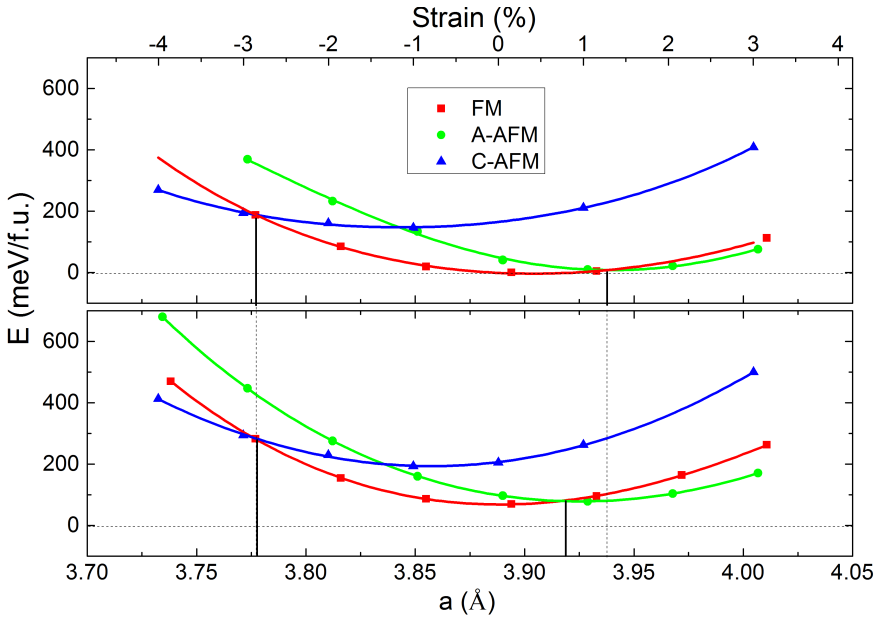

Figure 3.3: Total energy as a function of in-plane lattice constant for three magnetic orderings. The unstrained lattice constant is 3.89$\mathring{A}$. Atomic positions and cell volume are optimized at each strain. Top, $Pmc2_1$ structure. Bottom, $P4/mmm$ structure. The zero of energy in both figures is the minimum energy for the $Pmc2_1$ structure. The vertical lines show the transition strain values where the ground state magnetic ordering changes.

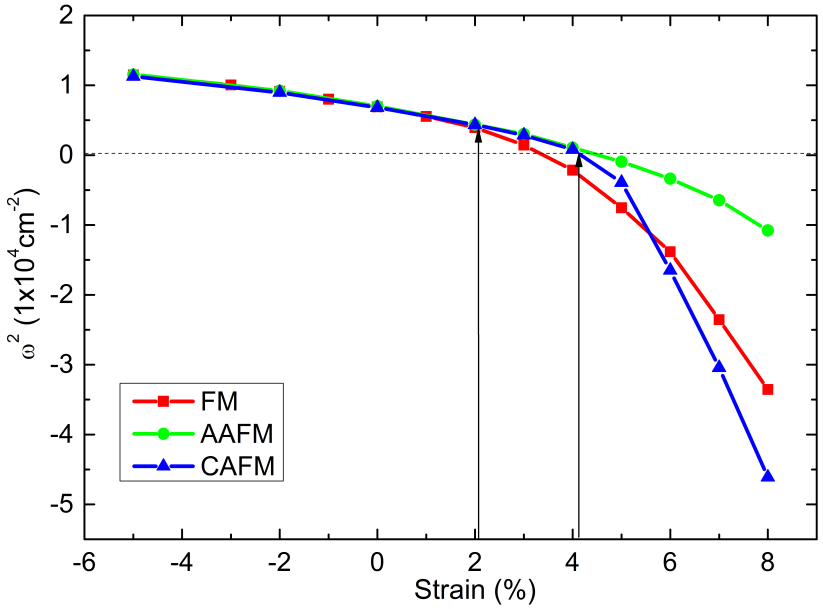

Figure 3.4: Frequencies squared of from E_{u1} in SMO/LMO superlattice as functions of in-plane strains. The vertical arrows show the strain values where the frequencies in FM, C-AFM and A-AFM deviate.

are 30 phonon modes at the Γ point, of which 18 are polar modes. In the SMO/LMO system, the lowest frequency mode is a E_u mode and denoted as E_{u1}. The E_{u1} modes for all three spin configurations are found to have frequencies of about 83 cm^{-1}, within 1 cm^{-1} of each other, and thus the spin-phonon coupling effect at 0% epitaxial strain is negligible.

The lack of spin-phonon coupling for the lowest frequency polar mode seems surprising in light of the large coupling in SMO mentioned in the Introduction. Calculations of the polar phonon frequencies of cubic LMO ($a = 3.890$Å) for FM and A-AFM magnetic orderings, show weak spin-phonon coupling for the lowest mode, 60 cm^{-1} for FM vs 63 cm^{-1} for A-AFM, but larger effects for the higher frequency modes: 192 vs 179 cm^{-1} and 315 vs 308 cm^{-1}.

To see if the greatly reduced spin-phonon coupling for the lowest frequency polar mode in the superlattice is due to the changes in the structure, we performed calculations of the phonon frequencies for the "pure SMO" structure, in which the La in the superlattice structure are replaced by Sr, and the "pure LMO" structure in which the

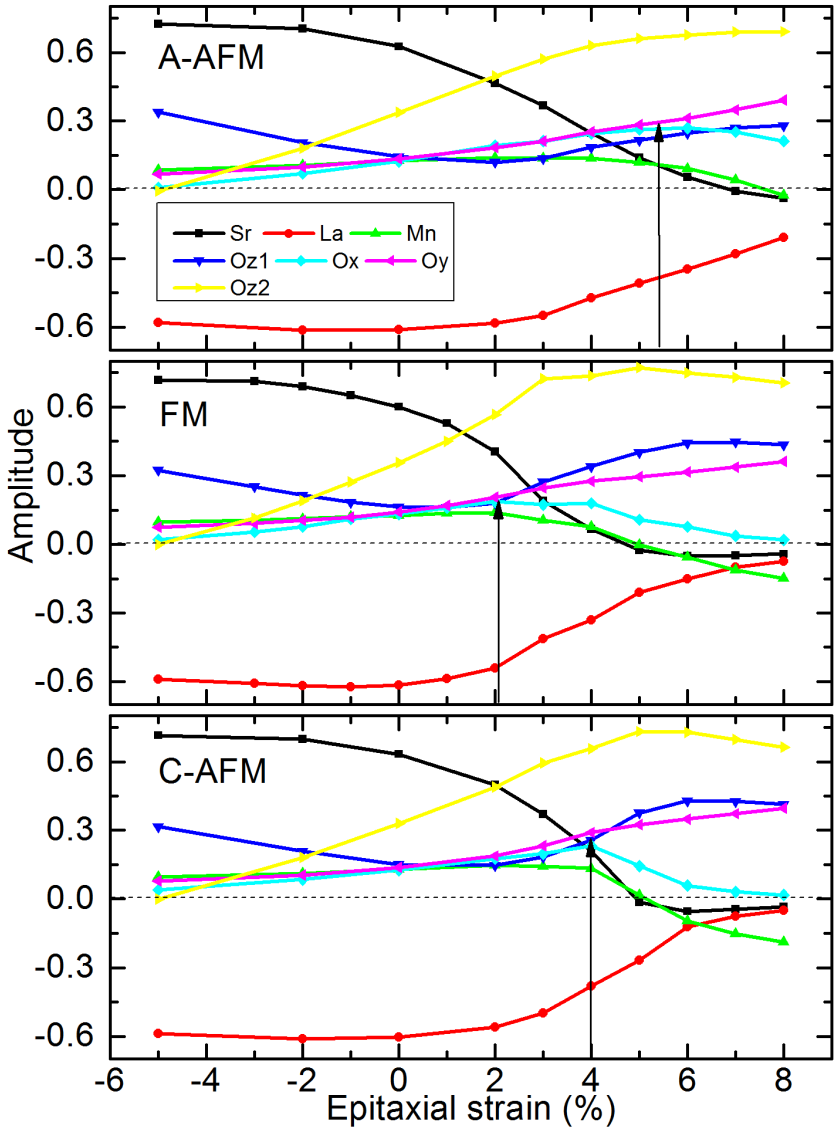

Figure 3.5: Amplitude squared of atomic displacements in the normalized x eigenvector of the lowest frequency E_u phonon mode in SMO/LMO superlattice as a function of in-plane strain. The reference structure for all three spin configurations is the same (the optimized structure for FM ordering). Top, A-AFM. Middle, FM. Bottom, C-AFM. The formula cell contains 10 atoms, but because of the mirror plane in LaO and SrO layers, the displacements of two Mn atoms are identical, as well as O_x and O_y atoms in two layers. The vertical arrows point out the transition points in E_{u1} at which the amplitudes of O_x and O_y deviate.

Sr in the superlattice structure are replaced by La. In "pure SMO", the E_{u1} mode is $221i$ cm^{-1} in FM, $174i$ cm^{-1} in A-AFM and $189i$ cm^{-1} in C-AFM. In "pure LMO", the E_{u1} mode is 10 cm^{-1} in FM, 9 cm^{-1} in A-AFM and 12 cm^{-1} in C-AFM. From this we conclude that the suppression of the spin-phonon coupling for the superlattice relative to SMO arises from the change in the electronic structure, the most obvious feature of this is the change in Mn valence (+3.5 in the superlattice and +4 in SMO).

However, application of tensile epitaxial strain in the superlattice can lead to a substantial spin-phonon coupling for the lowest E_u mode, as shown in Fig. 3.4. At 2% tensile strain, the FM phonon frequency deviates from the other two, and above 4% all three are split. The phonons in all three spin configurations become unstable with increasing tensile strain; because of the spin-phonon coupling the critical strain values in FM, C-AFM and A-AFM are different (3.3%, 4.2% and 4.5%, respectively).

To understand the nature of the "turning on" of the spin-phonon coupling, in Fig. 3.5 we show the independent components of the eigenvector of the lowest frequency phonon mode for the three magnetic orderings as a function of epitaxial strain. For compressive strains, the Sr and La atoms have the largest displacements, with the displacement of the La atoms opposite to that of Sr and the other atoms, corresponding to an antipolar A-site displacement pattern. In addition, the amplitudes of displacements of O_x and O_y atoms are almost identical. In contrast, in tensile strain, the amplitudes of displacements of A-site cations are small, with the two A-site cations moving in the same direction, while O displacements dominate, with different amplitudes of displacements of O_x and O_y atoms. The sharp change in the character of the eigenvector of the E_{u1} mode indicates the crossover of a higher frequency mode with increasing strain, with the transition in the lowest E_u mode occuring at the strain at which the amplitudes of O_x and O_y become different. These transition strains match precisely to the strain values in Fig. 3.4 at which the phonon frequencies begin to become different.

To investigate the crossover in the lowest E_u mode, in Fig. 3.6 we plot the frequencies of five of the seven E_u modes with respect to strain for three different magnetic orderings (the acoustic mode and an isolated mode at much higher frequency are excluded). The five E_u modes all soften with tensile strain, but not equally. The mode

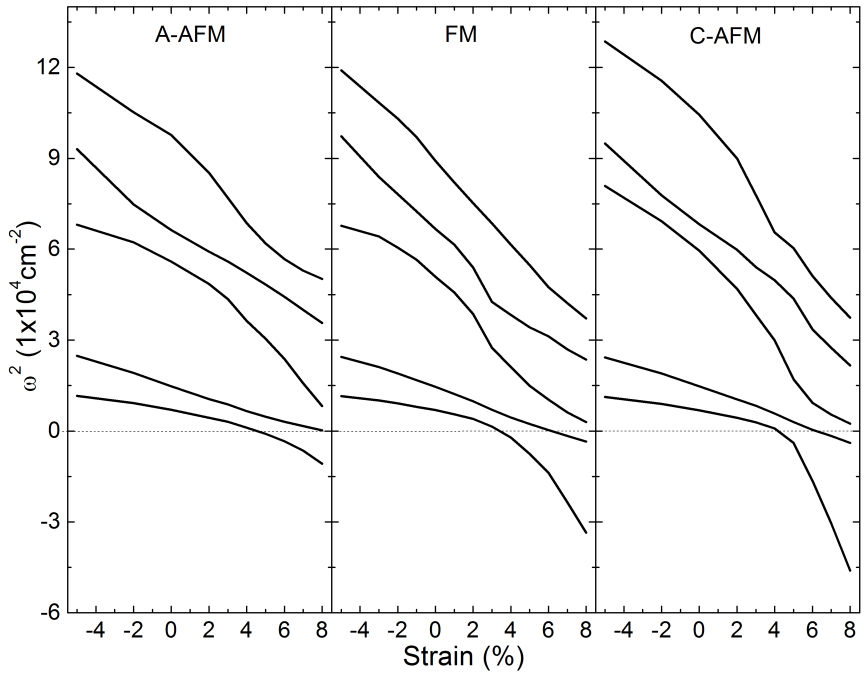

Figure 3.6: Squared frequencies for polar modes E_{u1} to E_{u5} in the SMO/LMO superlattice as functions of epitaxial strain.

with highest frequency for compressive strain appears to cross the other modes, mixing with them over the intermediate strain range, and to become the lowest frequency mode for large tensile strain. This is supported by the fact that the character of the highest frequency mode for compressive strain is similar to that for the lowest frequency mode for tensile strain. Moreover, this mode is seen to have a large spin-phonon coupling both for compressive and tensile strain.

To shed light on why this E_{u1} mode has a large spin-phonon coupling, we note it is dominated by O_z displacements, which directly change the Mn-O-Mn bond angle. By the Goodenough-Kanamori rules[67], this is the most effective way to change the exchange coupling J. Fig. 3.7 shows the displacement patterns for different strains. The displacement patterns for large tensile strains mainly bend the Mn-O_z-Mn bonds, making the FM ordering more favorable due to superexchange involving Mn t_{2g} and O p_z orbitals, as the bond angle is changed from 180°. Consequently, this mode gets softened in the FM and C-AFM phases, which have FM ordering out-of-plane, so that

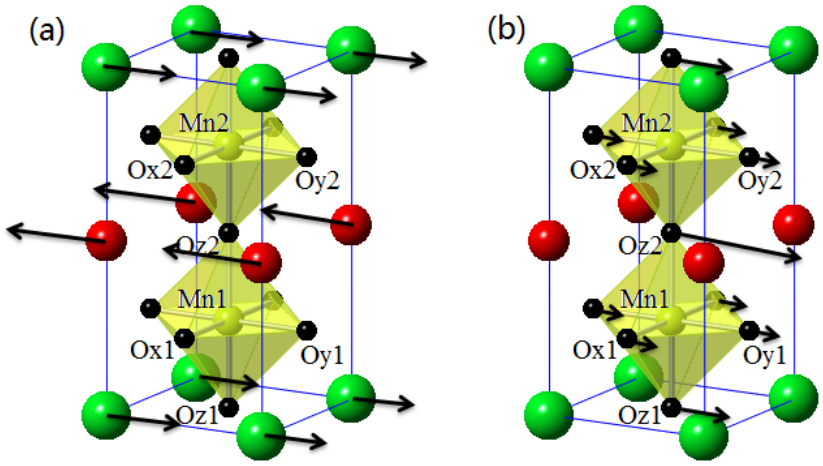

Figure 3.7: Atomic displacements of the lowest E_u mode for different strains. (a) Small strains and compressive strains. (b) Large tensile strains.

additional energy is gained.

These phonon calculations are for the high-symmetry $P4/mmm$ structure. In the ground state $Pmc2_1$ structure, a polar distortion is induced by the combination of oxygen octahedron distortions, as discussed briefly above. For compressive strains, this polar distortion has the same character (alternating in-plane La and Sr displacements) as the lowest frequency polar mode. For tensile strains, the instability of the oxygen-dominated polar mode will change the character of the polar distortion, though it will not break any additional symmetries.

The possibility of tuning the strengths of spin-phonon couplings by utilizing epitaxial strains to bring down modes with distinct character could be a general property of perovskite materials which would not be limited in the SMO/LMO system. This idea has been confirmed by calculations for the 1:1 $SrVO_3/LaVO_3$ superlattice[68].

3.3.4 Spin-phonon coupling coefficients

To describe the spin-phonon coupling quantitatively, we computed the J'' matrices, which specify the dependence of the exchange couplings on atomic displacements as described in the methods section above. The values of the force constants are one order of magnitude larger than the corresponding elements of the J'' matrices, and we thus

Table 3.2: Spin-phonon coupling strengths at 0% strain. Units, cm^{-2}.

State	ω^2_{PM}	$\lambda_{1x}+\lambda_{2x}$	$\lambda_{1y}+\lambda_{2y}$	λ_{1z}	λ_{2z}
E_{u1}	6897.0	41.9	23.1	3.0	59.7
E_{u2}	14806.9	172.3	71.8	19.3	89.6
E_{u3}	58298.5	649.2	844.9	453.5	431.3
E_{u4}	67285.8	146.4	139.6	-91.5	53.8
E_{u5}	100517.8	1634.4	1011.5	589.9	656.1

Table 3.3: Spin-phonon coupling strengths at 4% tensile strain. Units, cm^{-2}.

State	ω^2_{PM}	$\lambda_{1x}+\lambda_{2x}$	$\lambda_{1y}+\lambda_{2y}$	λ_{1z}	λ_{2z}
E_{u1}	1065.2	-231.3	965.6	999.8	35.3
E_{u2}	6280.6	-48.0	466.4	735.2	118.4
E_{u3}	35002.6	1026.5	889.6	23092.5	-20152.1
E_{u4}	51111.8	275.5	1466.6	4559.1	-2371.4
E_{u5}	66423.5	562.9	725.8	8441.6	-6983.6

treat J'' as a perturbation. Using the eigenvectors of C^{PM}, the first-order corrections to the squared frequencies are

$$\omega^2 = \omega^2_{PM} - \sum_{\alpha} \lambda_\alpha \langle S_{\alpha i} \cdot S_{\alpha j} \rangle , \tag{3.3}$$

where α represents the three Cartesian directions, and $\lambda_\alpha = \left\langle u_{PM} | J''_\alpha | u_{PM} \right\rangle$ is the spin-phonon coupling strength obtained from the computed 30×30 J'' matrices. We summarize the mode-specific coupling terms at 0% and 4% tensile strains in Table 3.2 and Table 3.3. The phonon frequencies of E_u modes in each magnetic ordering can be recovered by using the given λ values in Eq. 3.3. For the example of the E_{u3} mode at 4% tensile strain (Table 3.3) we find,

$\omega^2_F = \omega^2_{PM} - S^2 \cdot (\lambda_{1x}+\lambda_{2x}+\lambda_{1y}+\lambda_{2y}+\lambda_{1z}+\lambda_{2z}) = 20129.6$ cm^{-2},

$\omega^2_A = \omega^2_{PM} - S^2 \cdot (\lambda_{1x}+\lambda_{2x}+\lambda_{1y}+\lambda_{2y}-\lambda_{1z}-\lambda_{2z}) = 38139.5$ cm^{-2},

$\omega^2_C = \omega^2_{PM} - S^2 \cdot (-\lambda_{1x}-\lambda_{2x}-\lambda_{1y}-\lambda_{2y}+\lambda_{1z}+\lambda_{2z}) = 31865.7$ cm^{-2}. These squared frequencies with large spin-phonon couplings are those shown in Fig. 3.6.

From Tables 3.2 and 3.3, it can be seen that there are large differences between the spin-phonon coupling strengths at 0% and 4% epitaxial strain. This suggests that in addition to the dramatic effects resulting from crossover in the E_u mode, it should also

possible to tune the spin-coupling strengths using epitaxial strain.

3.4 summary

In summary, we have studied the influence of epitaxial strain on magnetic orderings and the couplings between the spins and polar phonons in the 1:1 SMO/LMO superlattice from first principles. The ground state magnetic order of the SMO/LMO superlattice from compressive to tensile strain is C-AFM, FM and A-AFM. We have shown that the spin-phonon coupling in the lowest polar phonon mode is weak at compressive strains and small strains, but it turns on when the tensile strain is greater than 2%, which can be attributed to a change of character of the lowest mode produced by different relative coupling of the various modes to epitaxial strain. We speculate that this could be a more general property of perovskite superlattices. Finally, we have calculated spin-phonon coupling parameters in a Heisenberg formalism and shown directly that the strength of spin-phonon couplings are functions of epitaxial strain. The tuning of spin-phonon coupling using epitaxial strain provides a useful approach for future tailoring of functional materials.

Chapter 4

Determination of ground-state and low-energy structures of perovskite superlattices from first principles

In the studies of Chapter 3, we have realize the issue to determine the ground state structure of the superlattice. In that case, the rotations do affect the total energies and slightly shift the magnetic phase boundary locations within epitaxial strain, without changing the main results. However, this is not always true. In the development of first-principles high-throughput searches for materials with desirable functional properties, there is a clear need for an efficient method to determine the ground state and low-energy alternative structures of superlattices. In this chapter, a method based on a simple strategy – to generate starting structures based on low-energy structures of the constituent compounds, which are then optimized via structural relaxation calculations – is proposed. This "stacking method" is demonstrated on the 2:2 $PbTiO_3/SrTiO_3$ superlattice, which has been the subject of recent experimental and theoretical interest. Considerations relevant to wider use of the method are discussed.

4.1 Introduction

Discovery of new functional materials with enhanced performance, novel functionalities and reduced cost and toxicity is a central goal of materials science. Recently, there has been tremendous progress in the synthesis of superlattices, which are artificially structured materials built up from unit-cell-scale layers of different constituent compounds[69, 70, 71]. In many cases, superlattices have distinctive functional properties, which can be attributed to the strain in the layers and the high density of interfaces[72, 73, 14]. The design of functional superlattice materials requires exploration of an enormous parameter space of constituent materials and layer sequences.

With the development of computational techniques and resources, specifically high-throughput first-principles approaches, this process can be greatly accelerated[74].

For the first-principles calculation of physical properties of a given system, determination of the ground-state structure (GSS) is the essential first step. Methods to predict the GSS from a given stoichiometry have recently been much discussed[75]. These include genetic algorithms[76, 77, 78], random search methods[79], data mining of experimentally-determined structural information[80, 81] and coupled cluster expansion method[82, 83]. While highly effective at identifying novel structures, such methods are very computationally demanding. Fortunately, for superlattices, the space of structures to be considered is already constrained by physical considerations, making these powerful but costly methods unnecessary. For (001) perovskite superlattices, the structures are expected to be closely related to the high-symmetry $P4/mmm$ structure generated from layered cation ordering in the ideal perovskite structure. As for pure perovskites, this high symmetry structure is expected to be unstable with respect to lower-symmetry structures with distortions such as polar distortions, oxygen octahedron rotations, and Jahn-Teller distortions. These instabilities can be identified by first-principles calculations of the phonon dispersion of the $P4/mmm$ structure, and different instabilities or combinations of instabilities can in general be expected to lead to a variety of low-energy metastable structures in addition to the ground state[84].

For perovskite superlattices, most first-principles studies have utilized one of three basic strategies for ground-state structure determination. One approach focuses on instabilities identified by first-principles phonon-dispersion calculations. Starting with the high-symmetry reference structure, the phonon dispersion is computed, unstable modes at high-symmetry points are identified, and a set of low-symmetry structures is obtained by freezing in selected modes and relaxing the structure. For each low-symmetry structure thus obtained, the phonon dispersion is calculated; the process terminates when the structure is at a local minimum of the energy. Given the computational demands of phonon-dispersion calculations, this method is expensive even in the simple case of a pure perovskite; for superlattices, with larger unit cells and more modes at each wavevector, it becomes prohibitive.

In the second method, closely related to the first, the phonon dispersion is computed only for the high-symmetry reference structure. The unstable phonon modes at high symmetry k-points are identified, and structures generated by freezing in the unstable modes, singly and in combination, are relaxed and compared, the one with lowest total energy being the GSS. A final phonon-dispersion calculation is performed to verify that the candidate GSS is stable. This method has been widely used in first-principles studies of the epitaxial-strain-induced phases of pure perovskites [85, 9] and ultrashort period (1:1) superlattices of perovskites[14, 86, 87, 15].

A quite different strategy is to generate starting structures by making small random displacements of the atoms away from the high-symmetry $P4/mmm$ structure, relax each starting structure and compare the distinct structures thus generated. This has the advantage of sampling the relevant structure space without any particular bias, but it is relatively demanding, as a general random initial configuration will take a large number of iterations to converge to the nearest minimum. Further, in principle this method could miss local minima or even the ground state due to statistical fluctuations, with no guarantees even if the number of starting structures is systematically increased. Therefore, this method is best used as a complementary "double check," to make sure that no exotic low-energy structures have been missed by other methods.

Given the ground state structure of the superlattice, it would be implausible if the structure of an individual layer were to derive from a high-energy bulk structure. Indeed, the assumption that the structures of each constituent layer should derive from the ground state of the corresponding pure compound at the relevant epitaxial strain has been used as the basis for structure determination in a number of previous studies [88, 89, 90]. If a starting structure is obtained by distorting each layer to its ground state structure, and then relaxed, the expectation is that the original distortions would remain, and additional distortions of certain types (specifically out-of-plane polarization and oxygen octahedron rotations about an in-plane axis) in one layer would induce the same distortion in an adjacent layer through considerations of electrostatic boundary conditions and steric constraints associated with the rigidity of oxygen octahedra. However, it should be noted that the structure of an individual layer could be derived

not from the ground state, but from a distinct low-energy alternative state of the corresponding pure compound at the relevant epitaxial strain. In that case, the "bulk" energy cost would be more than balanced by a reduction in energy associated with matching conditions or interface energetics. Thus, the assumption above should be modified to be that structures of the constituent layers will derive from a low-energy state of the pure compound at the relevant epitaxial strain, and that the ground state and low-energy states of the superlattice can be obtained by relaxing starting structures obtained from stacking combinations of the low-energy pure-compound states.

In this chapter, we propose a simple and efficient stacking method, suitable for high-throughput studies, to determine the GSS and low-energy structures in perovskite superlattices based on this modified assumption. In section 4.2, we describe the method in detail. In section 4.3, we demonstrate the method by application to the structure determination of the $(PbTiO_3)_2(SrTiO_3)_2$ superlattice as a function of epitaxial strain, as previous work suggests that this system is particularly rich in low-energy structures[14, 87]. We first describe the construction of a database of the low energy structures of the constituent pure compounds $PbTiO_3$ (PTO) and $SrTiO_3$ (STO). We then describe the results of structure determination of $(PbTiO_3)_2(SrTiO_3)_2$ (2:2 PTO/STO) via the stacking method, illuminating various aspects of implementation of the method. At 0% strain, we find that 2:2 PTO/STO does not have a unique GSS, as previously proposed[87], but that the energy surface at the lowest energy is rather flat. This has important implications for experimental studies of the structure and properties of this system.

4.2 Methods

Our stucture determination method, which we refer to the "stacking method," is based on the assumption that for the GSS of the superlattice, structures of the constituent layers will derive from a low-energy state of the pure compound at the relevant epitaxial strain. Based on this assumption, we construct starting structures by putting each constituent layer into a low-energy pure-compound structure, generating all such symmetry-inequivalent combinations. Relaxations from these starting structures using

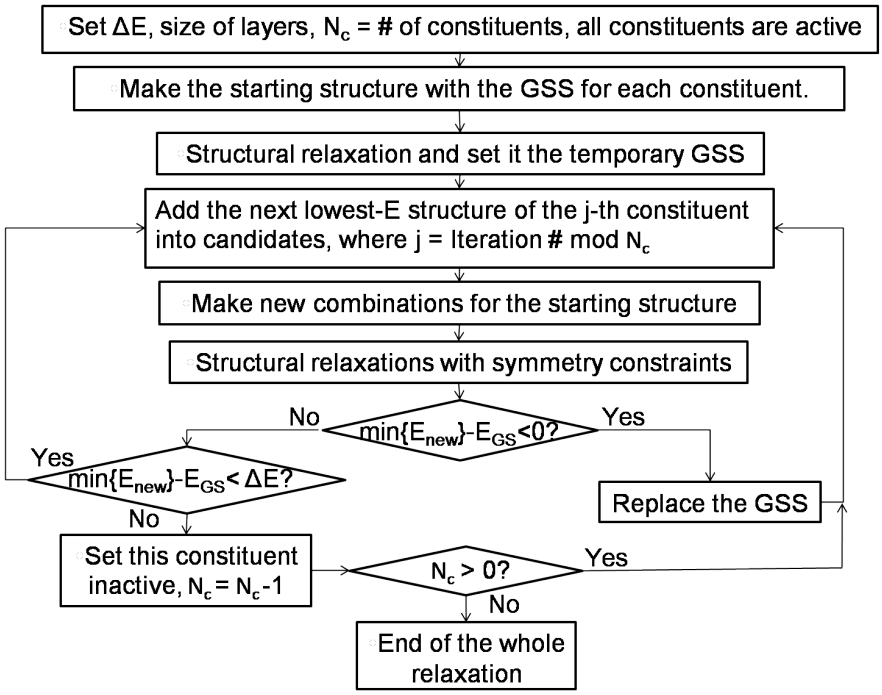

Figure 4.1: Flowchart for the stacking method for identification of the ground-state structure of a superlattice.

Hellmann-Feynman forces and stresses are performed to minimize the overall energy of the superlattice structure. This energy of the superlattice includes the energy associated with electrostatic interactions of the layers, steric constraints associated with rigidity of the oxygen octahedra, and contributions from the interface regions.

Our method is iterative, starting with combinations of the ground states of the constituents and adding low-energy constituent structures into the combinations until no more low-energy structures for the superlattice are found. For this, we choose an energy window: when the iterative step yields no new superlattice structures with energies within the window, the process terminates. Thus, in addition to the GSS, our method will identify the lowest-energy alternative structures as well, which can be of interest for functional properties.

Once the constituents for the superlattice are chosen, the first step is to generate the database of low-energy states of the pure constituent compounds at the relevant epitaxial strain. This can be done using a conventional method such as the second

method mentioned in Section 4.1. In a study including various combinations of several different constituents, it is convenient to generate the database for all constituents as a pre-processing step.

The steps in the stacking method for structure determination of a superlattice with specified layer thickness then follow the flow chart shown in Fig. 4.1:

(1) We set the energy window ΔE. We define N_c to be the number of active constituents. If a constituent has been given "inactive" status, we will not include any additional higher-energy structures for the relevant constituent. At the beginning, all constituents are active.

(2) We use the lowest energy structure for each constituent to construct the starting structure for the superlattice, with the atomic positions of the interfacial layers being the linear combination of the two adjacent constituents.

(3) We relax the structure and set it as the candidate GSS.

(4) Considering each constituent in turn, we take the next lowest-energy structure of the given constituent and construct "new" starting structures by combining it with the low-energy structures for the other constituents already included.

(5) We do structural relaxations on the new starting structures.

(6) If the minimum of the energy of the "new" superlattices, $\min\{E_{new}\}$, is lower than the current ground state energy E_{GS}, then we replace the GSS with the "new" superlattice of the lowest energy, and then return to step (4).

(7) If $0 < \min\{E_{new}\} - E_{GS} < \Delta E$, we check to see if any of the "new" structures in the energy window are distinct structures not already identified. We add these to the list of low-energy structures and return to step (4). If the number of distinct structures in the energy window is smaller than 3, then go to step (4). Else, if no new low-energy structures are found within the energy window or $\min\{E_{new}\} - E_{GS} > \Delta E$, then we are done with adding low-energy structures for this constituent. We declare this constituent to be inactive and decrease the number of active constituents N_c by one. If there are still active constituents, we go to step (4).

(8) If only the ground-state structure is desired, the process now terminates, with

the identification of the ground state structure as the lowest energy structure found. If the identification of low-energy alternative structures is also desired, there is one additional step (not included in the ground-state search flowchart in Fig. 4.1). For each low-energy superlattice structure S already identified, the full distortion patterns in each constituent layer are analyzed. All symmetry-inequivalent combinations of the distorted layer structures (those with reversal of the out-of-plane polarizations or in-plane rotations can be excluded as being much higher in energy) are generated. Those that are not symmetry-equivalent to S are included as additional starting structures and relaxed. This step will be explained in more detail in the discussion of the application to $(PbTiO_3)_2(SrTiO_3)_2$ superlattice.

Structural relaxations in this approach preserve space group symmetries, so that the space group of the relaxed structure will be the same or a supergroup of the space group of the starting structure. In the latter case, the iterative relaxation process will in general yield a structure that has tiny displacements of the atoms that break the symmetry of the supergroup. For example, if we start with a low-symmetry configuration with polar $P4mm$ which relaxes to a nonpolar $P4/mmm$ structure, the relaxed structure would in general have tiny displacements away from the $P4/mmm$ structure resulting in a space group of $P4/mmm$. For this reason, most space-group-identification software tools find the highest-symmetry space group consistent with displacements of the atoms by a specified distance, referred to as the tolerance. If the displacements in the case of the relaxed structure in the example above are less than the tolerance, the space group will be identified as $P4/mmm$. In the first-principles calculation, a very low tolerance ($10^{-5}\mathring{A}$) is chosen to avoid artificially increasing the symmetry during the calculation. Using the python package "pyspglib" [91], we analyze the relaxed structure by increasing the tolerance from $10^{-5}\mathring{A}$ until we find the critical tolerance (CT) at which the space group changes from the space group of the starting structure to one of its supergroups. A small CT suggests that the structure has relaxed into a structure with a higher symmetry space group. The upper limit on CT which establishes relaxation to the supergroup is $CT_{UL} = 2\delta E/\delta F$, where δF is the force threshold in the relaxation and δE is the energy resolution. We will discuss explicitly how the the upper limit on

CT is chosen for the example of 2:2 in the next section.

Our calculations for PTO/STO were performed using the local density approximation[22, 92] implemented in the *Vienna Ab initio Simulation Package* (VASP-5.2.12)[26, 27]. The projector augmented wave (PAW) potentials[30, 31] used contain 10 valence electrons for Sr ($4s^2 4p^6 5s^2$), 14 for Pb ($5d^{10} 6s^2 6p^2$), 10 for Ti ($3p^6 3d^2 4s^2$). We used a 500 eV energy cutoff, $\sqrt{2} \times \sqrt{2} \times 4$ supercell and $4 \times 4 \times 1$ Monkhorst-Pack(MP) k-meshes[93] for total energy calculations in structural relaxation, and the force threshold is $\delta F = 5 \times 10^{-3}$ eV/$\mathring{A}$. The energy resolution is 1 meV/5atom, so that $\delta E = 0.2$ meV/atom and the CT_{UL} is thus 0.08Å.

4.3 Results

4.3.1 Low energy structures of pure compounds: $PbTiO_3$ and $SrTiO_3$

In the stacking method, the first step in structure determination of a superlattice is construction of the database of the low energy structures of the constituent pure compounds at the relevant epitaxial strain(s). For our demonstration case $(PbTiO_3)_2(SrTiO_3)_2$, the constituents are PTO and STO. First-principles computations of the phonon dispersions for the cubic-perovskite high-symmetry reference structures show that in both compounds, Γ_{15} and R_{25} modes are unstable[94, 95]. To identify the low-energy structures for each compound at each epitaxial strain, we freeze in the unstable Γ and R modes, singly and in combinations, and relax the structures (we note that not all structures thus obtained will be distinct). The space group of each relaxed structure is identified by using the CT approach with a threshold of 0.08Å. Here we label the structures not by the space group, but by the distortions that generate them, indicated in Cartesian components. u and w denote nonzero in-plane and out-of-plane polar mode components, respectively, while a and c denote non-zero R-point octahedron rotations around in-plane and out-of-plane axes, respectively.

Figs. 4.2 and 4.3 show the relaxed total energies and CTs for bulk PTO for various combinations of polar distortions and R point octahedron rotations at three values of epitaxial strain (-2%, 0% and +2%, defined with respect to 3.849Å, the computed

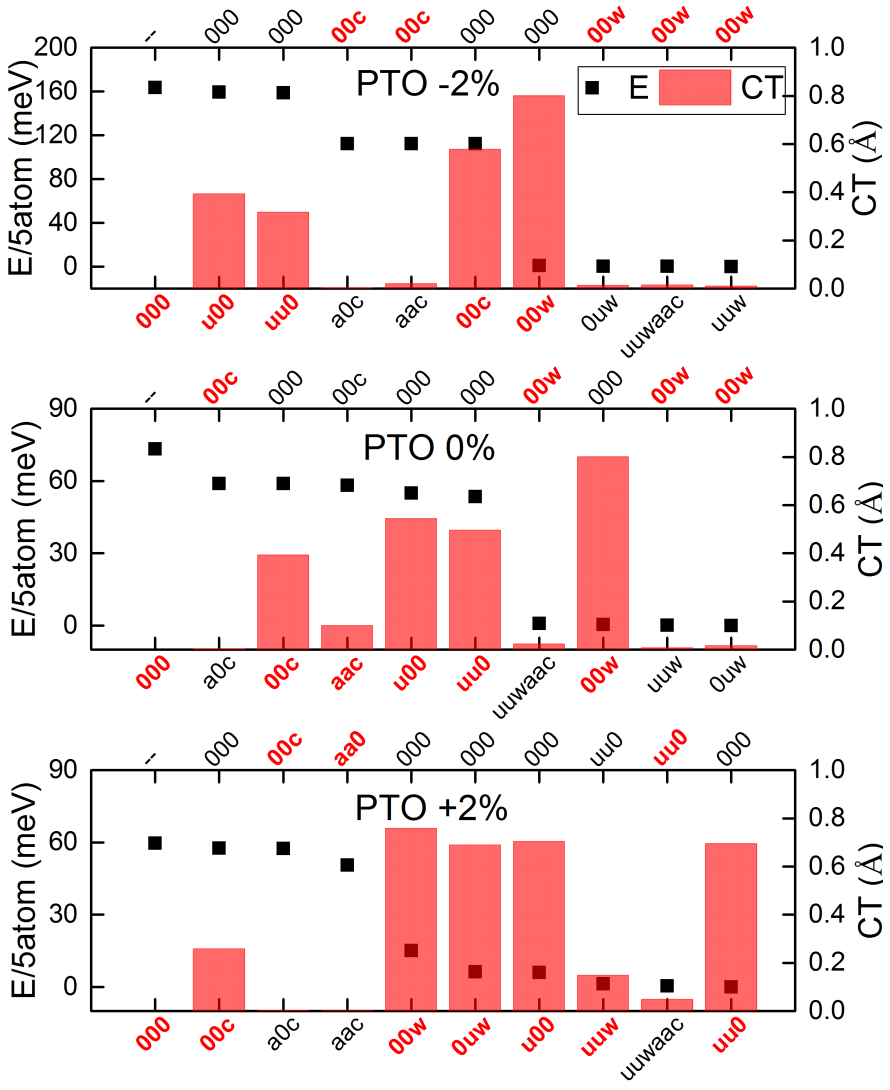

Figure 4.2: Total energies (black squares) and space-group-symmetry analysis for relaxed structures of epitaxially-strained PTO. Top, -2% strain. Middle, 0% strain. Bottom, +2% strain. Energies are in meV per 5 atoms, with the zero of energy for each strain taken as the energy of the ground state structure at that strain. The horizontal axis is labeled at the bottom by the space group of the starting structure, and at the top by the space group of the supergroup produced at values of the tolerance higher than the critical value CT, which is shown as a red bar. Stable distortions are typeset in bold red.

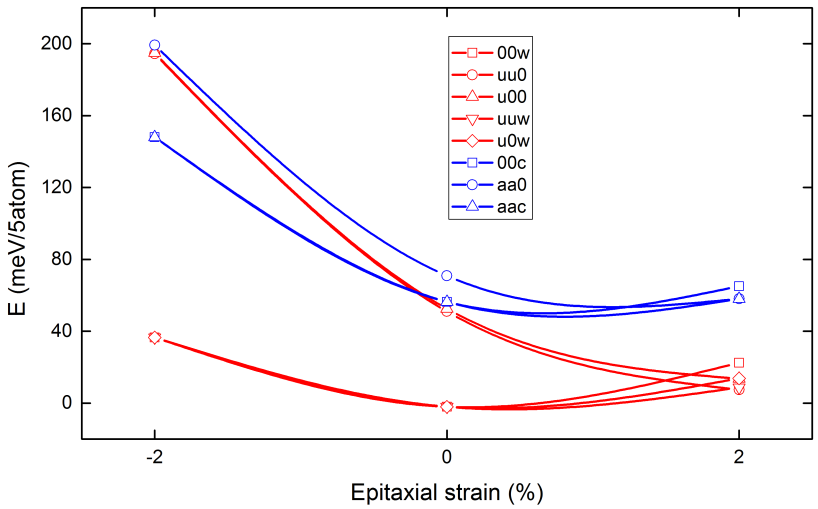

Figure 4.3: Energies of low-energy distorted structures of PTO as functions of epitaxial strain. Red lines represent structures with polar distortions, and blue lines represent structures with octahedron rotations.

lattice constant of cubic STO). For -2% and 0% epitaxial strain, the most favorable distortion is the out-of-plane polar distortion, denoted by $00w$, while for +2%, the states with in-plane polarization and out-of-plane polarization are essentially equal in energy, consistent with previous studies[96, 97, 98, 99, 100]. The low-energy structures at each strain, in order of increasing total energy, are listed in Table 4.1 and constitute the required database for PTO.

Figs. 4.4 and 4.5 show the analogous results for STO. For -2% epitaxial strain, the out-of-plane oxygen-octahedron rotation $00c$ is most favorable. For +2% epitaxial strain, in-plane polar distortions combined with in-plane octahedron rotations produce the lowest energy structures, with different combinations of these two distortions resulting in slightly different energies, in agreement with previous studies[101, 102, 103, 98]. The 0% epitaxial strain case is the most complicated: five distinct structures with different rotation patterns have almost identical energy. This suggests a rather flat energy surface. As for PTO above, the database of low-energy structures for STO is given in Table 4.1.

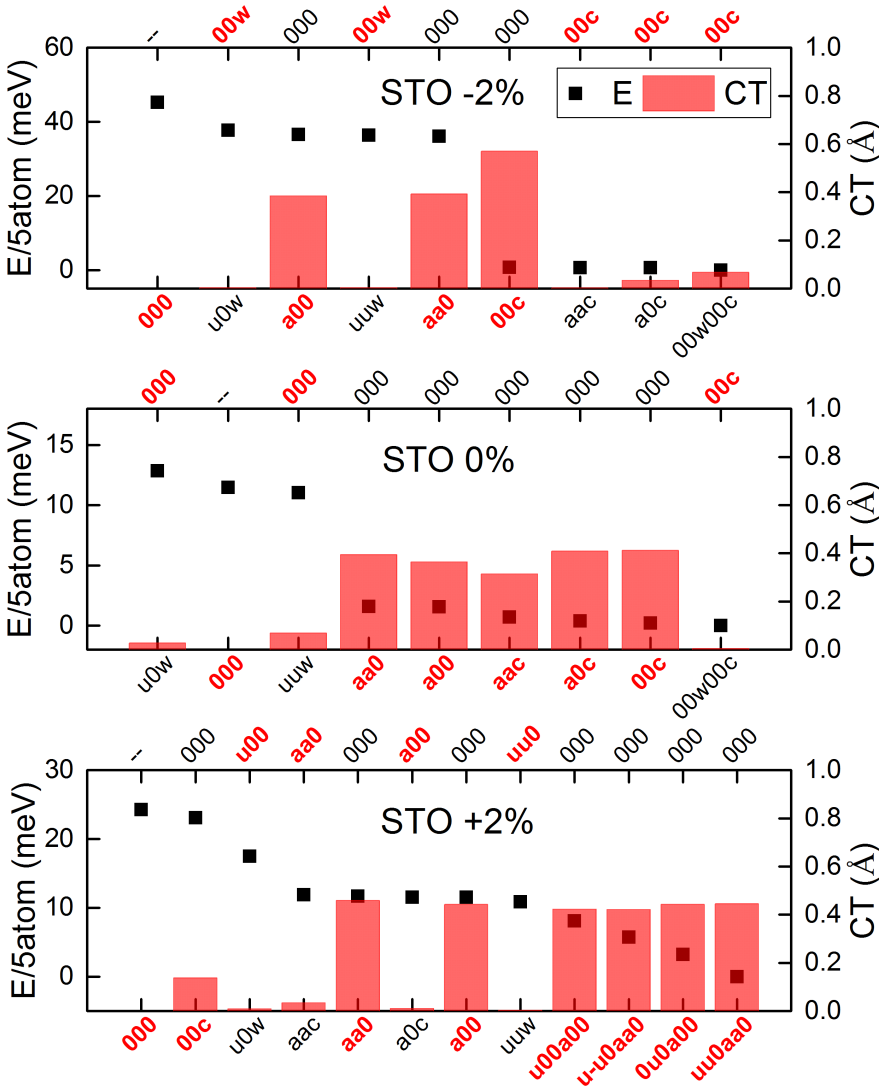

Figure 4.4: Total energies and space-group-symmetry analysis for relaxed structures of epitaxially-strained STO. Conventions as in Figure 4.2.

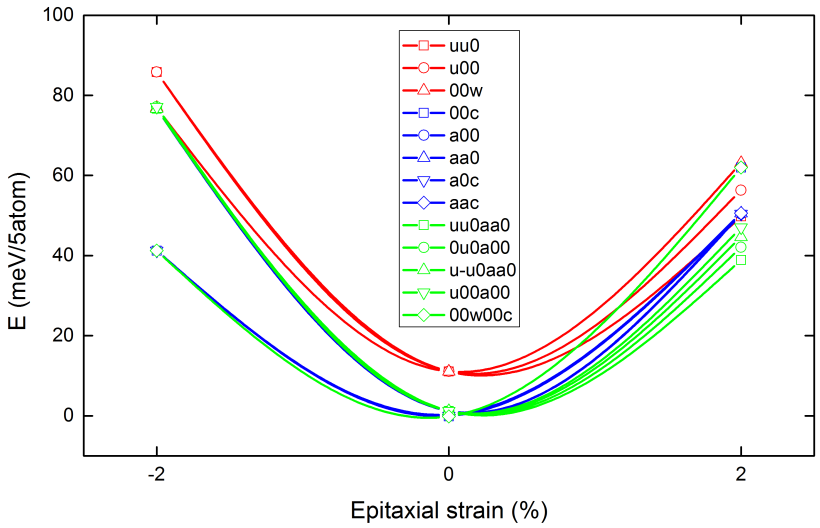

Figure 4.5: Energies of low-energy distorted structures of STO as functions of epitaxial strain. Red lines represent structures with polar distortions, blue lines represent structures with octahedron rotations, and green lines represent structures with combined distortions of polar modes and rotations.

Table 4.1: The low energy distorted structures of PTO and STO for -2%, 0% and +2% strain.

Perovskite	**Stable distortions**
PTO -2%	$00w$, $00c$, $uu0$, $u00$
PTO 0%	$00w$, $uu0$, $u00$, aac, $00c$
PTO +2%	$uu0$, uuw, $u00$, $u0w$, $00w$, $aa0$, $00c$
STO -2%	$00c$, $aa0$, $00w$, $a00$
STO 0%	$00c$, $a0c$, aac, $a00$, $aa0$
STO +2%	$uu0aa0$, $0u0a00$, u-$u0aa0$, $u00a00$, $uu0$, $a00$, $aa0$, $u00$, $00c$

Table 4.2: Space groups of $(PTO)_2/(STO)_2$ starting structures for -2% strain. The space group information is obtained using ISOTROPY[104, 105]. The labels #1 and #2 differentiate between two inequivalent starting structures with the same space group.

PTO/STO	$00c$	$aa0$	$00w$
$00w$	$P4bm\#1$	$Pma2$	$P4mm$
$00c$	$P4/mbm$	$P2_1/c$	$P4bm\#2$

Table 4.3: Space groups of $(PTO)_2/(STO)_2$ starting structures for +2% strain. Conventions as in Table 4.2. The triplets in parentheses indicate different settings for a given space group.

PTO/STO	$uu0aa0$	$0u0a00$	$u\text{-}u0aa0$	$u00a00$
$uu0$	$Pnc2$	$Pc\#1$ $(00\frac{1}{4})$	$Pc\#2$ $(00\frac{1}{4})$	$Pc\#3$ $(00\frac{1}{4})$
$u\text{-}u0$	$Pc\#4$ $(00\frac{1}{4})$	$Pc\#5$ $(00\frac{1}{4})$	$Pmn2_1$	$Pc\#6$ $(00\frac{1}{4})$
uuw	$Pc\#7$ $(\frac{1}{4}00)$	$P1\#1$	$P1\#2$	$P1\#3$
$u\text{-}uw$	$P1\#4$	$P1\#5$	Pm	$P1\#6$
$u00$	$Pc\#8$ $(00\frac{1}{4})$	$Pc\#9$ $(00\frac{1}{4})$	$Pc\#10$ $(00\frac{1}{4})$	$Abm2\#1$
$0u0$	$Pc\#11$ $(00\frac{1}{4})$	$Pc\#12$ $(00\frac{1}{4})$	$Pc\#13$ $(00\frac{1}{4})$	$Abm2\#2$ $(00\frac{1}{4})$
$u0w$	$P1\#7$	$P1\#8$	$P1\#9$	$Cm\#1$ (000)
$0uw$	$P1\#10$	$Cm\#2$ $(\frac{1}{2}00)$	$P1\#11$	$P1\#12$

4.3.2 Structure determination for $(PTO)_2/(STO)_2$

In this section, we describe the starting structures and the ground-state and low-energy structures of $(PTO)_2/(STO)_2$ found through our structural determination procedure with an energy window of 30 meV/5 atoms for -2% epitaxial strain and 15 meV/5 atoms for 0% and +2% epitaxial strain. As discussed in the previous section, in both compounds, at -2% there is a single structure much lower in energy than the others, and it is expected that the GSS of the superlattice will be a stacking of these two structures. At 0% and +2% strain, the near-degeneracy of several low-energy states in one or both compounds is expected to lead to a less clear-cut situation requiring a

Table 4.4: Space groups of $(PTO)_2/(STO)_2$ starting structures for 0% strain. Conventions as in Table 4.2 and 4.3. The dash indicates that the structure is equivalent to the one above it.

PTO/STO	$00c$	$a0c$	aac	$a00$	$aa0$
$00w$	$P4bm$	$Cm\#1$ ($\frac{1}{2}00$)	$Pc\#1$ ($\frac{1}{4}00$)	$Cmm2$	$Pma2$
$uu0$	$Pmc2_1$	$P1\#1$	$Pc\#3$ ($\frac{1}{4}00$)	$Pc\#2$ ($00\frac{1}{4}$)	$Pnc2$
u-$u0$	-	-	$P2_1$	-	$Pmn2_1$
$u00$	$Amm2\#1$ ($\frac{1}{2}0\frac{1}{4}$)	$Cm\#2$ ($\frac{1}{2}00$)	$P1\#2$	$Abm2\#1$ (00-$\frac{1}{4}$)	$Pc\#4$ ($00\frac{1}{4}$)
$0u0$	-	$C2$	-	$Abm2\#2$ (-$\frac{1}{4}$-$\frac{1}{4}$-$\frac{1}{4}$)	-

systematic approach; it is here that our stacking method will yield nontrivial results.

The simplest case is for -2% strain. The iterative process terminates after only six starting structures, shown in Table 4.2. Specifically, only two PTO low-energy structures are included, as inclusion of PTO $uu0$ yielded no new superlattice structures within the energy window and "inactivated" the PTO layer in further iterations, while all four low-energy structures of STO are included. The starting structures are thus obtained by combining the two lowest energy structures of PTO at -2% strain with the three lowest energy structures of STO at -2% strain (the rows and columns, respectively, of Table 4.2).

As shown in the top panel of Fig. 4.6, the GSS is $P4bm$, obtained from the $P4bm\#1$ starting structure built from the ground state of PTO ($00w$) and STO ($00c$), with octahedron rotations and polar displacements along [001], consistent with previous results[87]. The $P4bm\#2$ starting structure also relaxes to this structure. In this $P4bm$ state, the interlayer interactions induce octahedron rotations in the PTO layer and out-of-plane polarization in the STO layer. The main distortions are therefore can be denoted as $00w00c/00\tilde{w}00\tilde{c}$ using the notation we defined, where the tilde for the STO layer is used to indicated that the amplitude of the distortion is in general different from that in the PTO layer. Rotations in TiO_2 atomic layers between PbO atomic layers and those between SrO atomic layers are in the same direction and with

surprisingly close amplitudes. Rotations in the two interfacial TiO_2 atomic layers are in opposite directions, so that one is in the same direction as the bulk atomic layers and the other opposite. Above the GSS we find two unstable saddle point structures, $P4/mbm$ ($00c/00\tilde{c}$) and $P4mm$ ($00w/00\tilde{w}$) which are supergroups of the GSS $P4bm$, and a distinct structure, $Pma2$ ($00waa0/00\tilde{w}\tilde{a}\tilde{a}0$), with small amplitudes of octahedron rotations along [110][106].

For +2% strain, there are many low-energy states of STO at this strain. Also the low-energy states of STO and PTO include in-plane distortions along [110] or [100], as shown in Table 4.1, and so there can be multiple symmetry-inequivalent ways to combine distortions due to different relative orientations of the in-plane distortions. A lot of starting states relax into the single $Pnc2$ state ($uu0aa0/\tilde{u}\tilde{u}0\tilde{a}\tilde{a}0$), with the polar distortion along [110] and octahedron rotations around [110]. However, the criterion that at least three distinct structures need to be found before the termination of the iterative process leads to the inclusion of three and four low energy bulk structures for PTO and STO, respectively, as listed in Table 4.3. The majority of starting structures (26 out of 32) relax to the GSS $Pnc2$ structure as shown in the bottom panel of Fig. 4.6 (the data for 15 of the Pc and $P1$ starting structures are not shown; they all relax to the GSS $Pnc2$ structure). Octahedron rotations are induced in PTO layers due to the interlayer interactions, with amplitudes similar to those in STO layers. However, in contrast to the large energy difference between distinct structures for -2%, here the energy scale for alternative low-energy states is smaller, due to the smaller energy differences for stable distortions in +2% strained bulk STO. We also find a unstable saddle point structure above the GSS, $Amm2$ ($uu0/\tilde{u}\tilde{u}0$), which is the supergroup of the GSS $Pnc2$, and other alternative low-energy structures $Abm2_{low}$ ($0u0a00/0\tilde{u}0\tilde{a}00$), and $Abm2_{high}$ ($u00a00/\tilde{u}00\tilde{a}00$)[106].

The most complicated case is for the intermediate value of 0% strain. Low-energy states of STO and PTO both with in-plane distortions, characteristic of tensile strain, and out-of-plane distortions, characteristic of compressive strain, are represented in the starting-state combinations determined by the iterative process (Table 4.4). We find that the $P4bm$ stacking of the two ground states for the constituent compounds is in

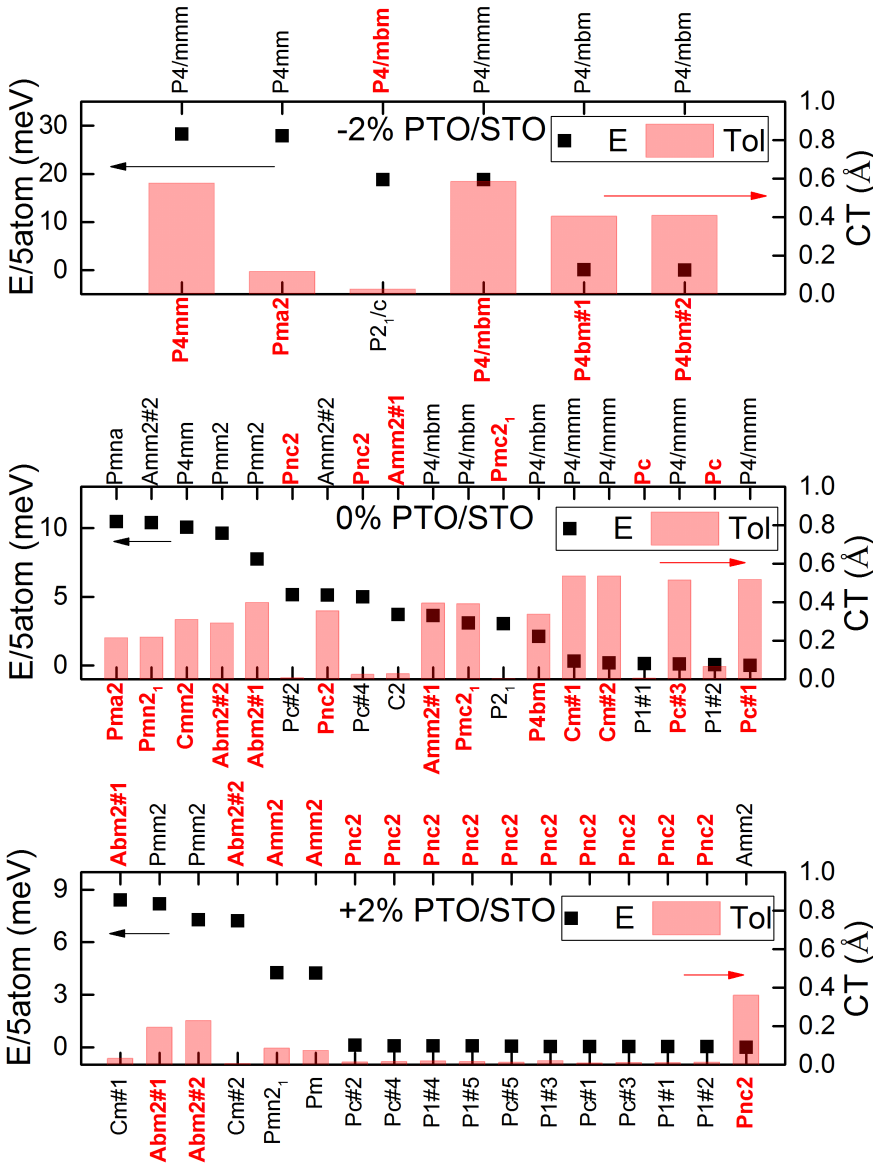

Figure 4.6: Total energies and space-group-symmetry analysis for relaxed structures of the epitaxially-strained 2:2 PTO/STO superlattice. Conventions as in Figure 4.2.

fact not the ground state structure for the superlattice. Further, the GSS is not unique: as seen in the middle panel of Fig. 4.6, relaxation identifies two distinct structures, Cm and Pc, with an energy difference less than 0.3 meV/5 atoms, less than the resolution of our calculation. Both the Pc and Cm structures have octahedron rotations and polar displacements in each constituent layer. The difference is that the direction of in-plane distortions is [110] for Pc ($uuwaac/\tilde{u}\tilde{u}\tilde{w}\tilde{a}\tilde{a}\tilde{c}$) and is [100] for Cm ($u0wa0c/\tilde{u}0\tilde{w}\tilde{a}0\tilde{c}$), suggesting a "flat" energy surface for in-plane distortions. The ground-state Pc structure has been previously identified and discussed[87]. The present results suggest that the experimental determination of the low-temperature structure would not show Pc as a well-defined ground state, but that the results would show variations in the directions of the distortions resulting from the flatness of the energy surface in the vicinity of this structure, which could also have an impact on the physical properties. In addition to the characterization of the ground state, at this stage we find a number of low-energy unstable saddle point structures. $P4bm$ ($00w00c/00\tilde{w}00\tilde{c}$), $Pmc2_1$ ($uu000c/\tilde{u}\tilde{u}000\tilde{c}$), $Amm2$ ($uu0/\tilde{u}\tilde{u}0$), $Pnc2$ ($uu0aa0/\tilde{u}\tilde{u}0\tilde{a}\tilde{a}0$), $Abm2$ ($u00a00/\tilde{u}00\tilde{a}00$), $Cmm2$ ($00wa00/00\tilde{w}\tilde{a}00$), $Pmn2_1$ (u-$u0aa0/\tilde{u}$-$\tilde{u}\tilde{a}\tilde{a}0$), $Pma2$ ($00waa0/00\tilde{w}\tilde{a}\tilde{a}0$)[106]. They are all supergroups of the GSS Pc or Cm structures.

Finally, we carried out the final step described in Sec. 4.2 to identify additional low-energy structures. First, for 0% strain, we analyzed the full distortion patterns in each constituent layer for the Pc GSS, which can be characterized as *uuwaac* (in-plane polarization along [110], out-of plane polarization along [001], octahedron rotation around [110] and octahedron rotation around [001]. Excluding the configurations with high energy due to electrostatics or steric constraints, these can be combined in four ways: $uuwaac/\tilde{u}\tilde{u}\tilde{w}\tilde{a}\tilde{a}\tilde{c}$, -$u$-$uwaac/\tilde{u}\tilde{u}\tilde{w}\tilde{a}\tilde{a}\tilde{c}$, $uuwaa$-$c/\tilde{u}\tilde{u}\tilde{w}\tilde{a}\tilde{a}\tilde{c}$ and -u-$uwaa$-$c/\tilde{u}\tilde{u}\tilde{w}\tilde{a}\tilde{a}\tilde{c}$. Two of these, $uuwaac/\tilde{u}\tilde{u}\tilde{w}\tilde{a}\tilde{a}\tilde{c}$, -$u$-$uwaac/\tilde{u}\tilde{u}\tilde{w}\tilde{a}\tilde{a}\tilde{c}$, relaxed to the Pc GSS, while the other two relax to a distinct Pc structure with energy 2 meV/5 atoms above the ground state, which we denote as Pc_{high}. The Pc_{high} structure is closely related to the ground state Pc structure, the main difference being the pattern of oxygen octahedron rotations around [001]. As shown in Fig. 4.7, for the Pc_{high} state the octahedron between SrO layers rotates in the opposite sense to the one between PbO layers, while for the Pc

GSS state, these two octahedra rotate in the same direction.

The reason that this low-energy structure was not identified in the earlier steps of structure determination is that the starting structures did not contain any oxygen octahedron rotation in the PTO layer (see Table 4.4). The rotation in the PTO layer in the relaxed structure is induced by the symmetry breaking for the superlattice by the rotations in the STO layer, picking out one of two senses for the rotation. Fig.4.8 shows an analogous coupling of distortions in a pure perovskite, showing two inequivalent local minima obtained by freezing a Γ_3^- mode into a structure obtained by freezing in a M_3^+ and a M_1^- mode; symmetry analysis shows that in the energy expansion around the high-symmetry cubic structure there is a term trilinear in M_3^+, M_1^- and Γ_3^-. By relaxation of the starting state with M_3^+ and M_1^- nonzero and Γ_3^-=0, only the lower minimum would be found.

With the same procedure applied to the Cm GSS at 0% strain and the $P4bm$ GSS at -2% strain, we find a Cm_{high} state at 0% with distortion pattern $u0wa0$-c+$u0wa0c$ and energy 2 meV/5 atoms, and a $P4bm_{high}$ state at -2%, with distortion pattern $00w00$-$c/00\tilde{w}00c$ and energy 3 meV/5 atoms. The appearance of inequivalent local minima thus appears to be relatively common in superlattices. The idea that the low-energy landscape is complex for small epitaxial strain, as observed in a previous study[87], is here strengthened by the fact that even more distinct structures at small scales of differences in total energies are found by the stacking method than previously recognized.

As a complementary approach to investigating the energy surface for the 0% case, we generated and relaxed twenty randomly-distorted starting structures[107]. The results are shown in Fig. 4.9. Seven of the starting structures relax to the Pc GSS, one relaxes to the Cm GSS, and eight are at the same energy with a CT just barely larger than our threshold of 0.08Å, indicating that they stay in $P1$ structure but are close to the Cm or Pc GSS, corresponding to intermediate directions of in-plane polarization. For the ground state, these results confirm the flatness of the energy surface suggested by our stacking method results. Four of the starting structures relax to the low-energy structure Pc_{high}. The low-energy state Cm_{high} was missed in this process.

It is also instructive to put our results into the context of a more conventional "energy curve" approach for constructing epitaxial phase sequences. This approach involves computation of the epitaxial strain dependence of the energy for relaxed structures based on selected distortions of the superlattice, plotting of the energies vs epitaxial strain, and analysis of the resulting curves to find the ground state structure and low energy structures at each strain. We performed additional calculations of the total energies of all the low-energy structures identified in our structure determination (Fig. 4.6) for all three values of epitaxial strain, and present the resulting set of energy vs epitaxial strain curves in Fig. 4.10. At -2% strain in Fig. 4.10, the stacking method identified the three lowest-energy configurations, $P4bm$, $P4/mbm$ and $P4mm$, the other two structures in this diagram being outside the 30 meV/5atoms energy range. For +2% strain, the stacking method identified the four lowest-energy structures (shown as three points in Fig. 4.10 due to the small energy differences), the other two structures being outside the energy window. In agreement with previous work[14, 87], at 0% strain, many distinct structures are close in energy, The energy curve approach is useful in understanding the evolution of symmetry-breaking distortions with strain and the resulting phase transitions, but involves energy computation for structures that are quite high in energy. In addition, the selection of distortions for the superlattice is generally not systematic. In comparison, our stacking method concentrates on the low-energy structures at each strain, and thus is more efficient for constructing the phase sequence and identifying the low-energy alternative structures at each strain.

4.4 Discussion

The example of PTO_2STO_2 demonstrates that the stacking method provides an efficient and systematic method for identifying the ground state and low-energy alternative structures for perovskite superlattices. The results at 0% strain show that it is not enough to combine ground state structures of constituents, as has been assumed in some past studies, but that the ground state of the superlattice can be derived from alternative low-energy structures of the constituents. Further, the stacking method found ground-state and low-energy structures that had been missed by other methods.

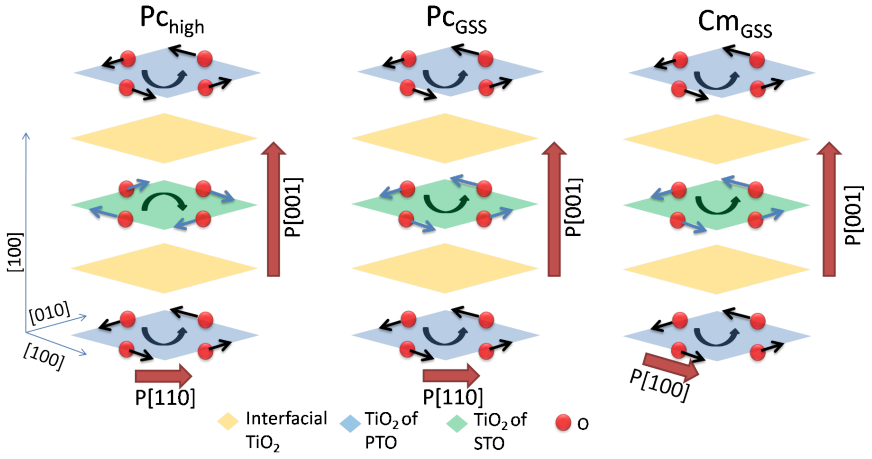

Figure 4.7: Oxygen octahedron rotation patterns and polarization directions for the Pc_{GSS}, Pc_{high} and Cm_{GSS} structures of the 2:2 PTO/STO superlattice. The rotations of the two interfacial TiO_2 planes (yellow) are in the same sense in all three structures and are not shown. The blue and green planes represent the TiO_2 layer between SrO layers and PbO layers, respectively. Note that the sense of the rotation in the central layer of Pc_{high} is opposite to that of the rotation in the central layer of Pc_{GSS} and Cm_{GSS}.

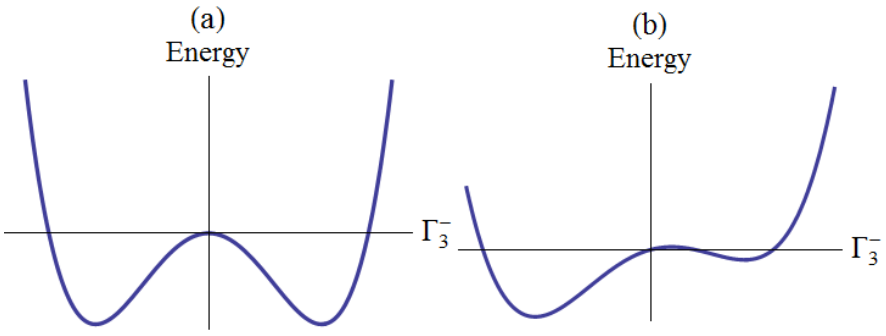

Figure 4.8: Schematic curves for the total energy as a function of the amplitude of an unstable mode in two cases: trilinear terms including the mode are (a) forbidden by symmetry, or (b) allowed by symmetry.

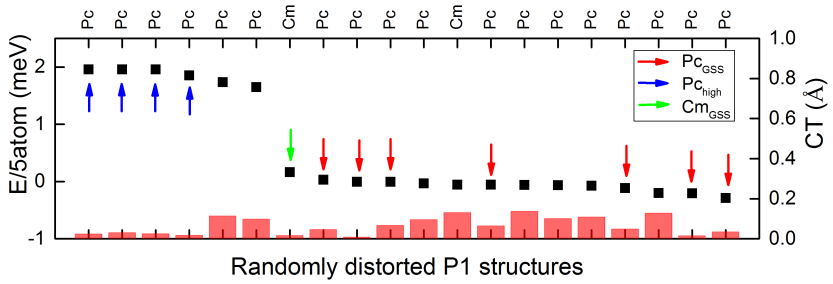

Figure 4.9: Total energies and space-group-symmetry analysis for relaxed structures of the epitaxially-strained 2:2 PTO/STO superlattice from a set of 20 randomly-distorted $P1$ starting structures. Conventions as in Figure 4.2. Red, blue and green arrows point to Pc_{GSS}, Pc_{high} and Cm_{GSS} states, respectively. The Cm_{high} state does not appear in this set.

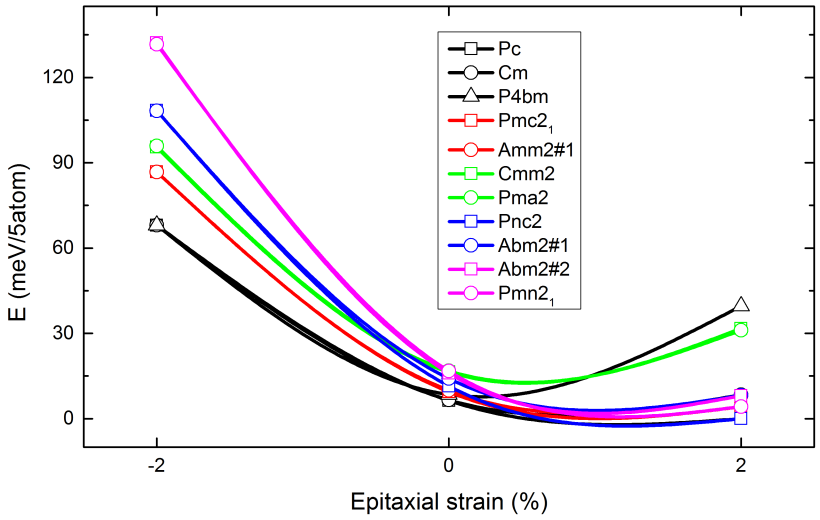

Figure 4.10: The total energies of all the low-energy superlattice structures as functions of epitaxial strain, as described in the text. The line colors are chosen to correspond to the five distinct structures observed at -2% strain.

The approach is readily generalized to multicomponent perovskite superlattices and to superlattices based on other structure types.

We note that there may be exceptional cases in which our basic assumption, that the structure of an individual layer derives from a low-energy structure of the constituent compound, is violated. It is for this reason that our method includes a complementary small-scale random search that could identify such systems by yielding low energy structures that violate this assumption. We also emphasize that this approach avoids making an exhaustive examination of all possible structures, no matter how implausible, for a chosen supercell. The supercells for the starting structures are determined by the low energy structures determined for the constituent compound, and effort is focused on the structures most likely to be low in energy given the validity of the basic assumption. The method is thus particularly suitable for high-throughput studies of superlattices with constituents drawn from a specified set of pure compounds. Once the database of low-energy structures for the specified set of compounds is constructed, the generation of starting structures is rapid and automatic, and computational effort is focused on structures that are likely to be low in energy.

4.5 Summary

In summary, we have proposed a stacking method for the determination of the GSS and low-energy structures in perovskite superlattices. This method has been demonstrated on the 2:2 PTO/STO superlattice. For the range of epitaxial strain considered, our results for the GSS are consistent with previous work. For 0% strain, this method highlights the previously unrecognized feature that the energy surface is flat at the lowest energies and hence the GSS is not unique. The method is double-checked by the random initial configuration method, and no structures with lower energy are found. We have also shown the existence at 0% strain of a second low-energy structure with the same space group as the Pc GSS, which could be difficult to identify using other methods. This method allows for the efficient determination of the GSS and low-energy structures in general superlattice systems, paving the way for high-throughput studies of superlattices.

Chapter 5

$SrCrO_3/SrTiO3$ superlattice: Coupled nonpolar-polar metal-insulator transition

Within this chapter, using first principles calculations and the stacking method introduced in Chapter 4, we determined the epitaxial-strain dependence of the ground state of the 1:1 $SrCrO_3/SrTiO_3$ superlattice. The superlattice layering leads to significant changes in the electronic states near the Fermi level, derived from Cr t_{2g} orbitals. An insulating phase is found when the tensile strain is greater than 2.2% relative to unstrained cubic $SrTiO_3$. The insulating character is shown to arise from Cr t_{2g} orbital ordering, which is produced by an in-plane polar distortion that couples to the superlattice d-bands and is stabilized by epitaxial strain. This effect can be used to engineer the band structure near the Fermi level in transition metal oxide superlattices.

5.1 Introduction

Metal-insulator transitions (MIT) occur in many transition metal oxides as a function of composition, temperature, pressure and epitaxial strain [4]. At the atomic scale, the mechanism for the metal-insulator transition depends on the physics of the insulating state. For Mott insulators, the relevant parameters are the transition metal (TM) *d*-level occupation, which can be changed through doping, and the bandwidth, which can be changed by varying the TM-oxygen-TM bond angles. For band insulators, a gap can be opened at the Fermi level by a structural distortion that lowers the crystal symmetry. A symmetry-breaking distortion that lifts the degeneracy of a partially occupied state will always lower the energy; this is called a Jahn-Teller distortion or a Peierls distortion depending on whether the degenerate states are localized atomic orbitals or extended bands. Polar distortions have also been shown to couple to states near the Fermi level,

proving useful in band-gap engineering[108, 109]. When the distortion can be controlled by an applied field or stress, the system can dynamically be driven back and forth through the MIT, a property of particular interest for applications to high-performance switching devices[110, 111],

$SrCrO_3$ (SCO) is a d^2 perovskite. It was initially reported as a paramagnetic and metallic cubic perovskite[112]. Experimental studies also showed a tetragonal C type antiferromagnetic (C-AFM) phase, with the Neel temperature below 100K and space group $P4/mmm$, coexisted with the cubic phase in the low temperature[113, 114]. This tetragonal C-AFM state is further investigated in first-principles studies[115, 116]. It is correlated to a partial orbital ordering d^1_{xy},$(d_{yz}d_{xz})^1$, where the d_{xy} is nearly occupied while d_{yz} and d_{xz} orbitals are both half occupied[114, 115]. For the single layer film of SCO epitaxially grown on $SrTiO_3$, due to the missing apical oxygen of the CrO_5 octahedra at the surface, d_{yz} and d_{xz} orbitals become lower in energy than d_{xy}, leading to a $d^1_{yz}d^1_{xz}d^0_{xy}$ orbital ordering and an insulating state[10]. However, recently Zhou *et al* claimed that SCO is an insulator while the insulator-metal transition occurs under sufficient pressure[117], due to the bond instability found around 4 GPa, suggesting the strong interaction between structure and electronic structure.

Layering a d-band perovskite oxide in a superlattice with a d^0 insulating perovskite will lead to large changes in the d-band states near the Fermi level, depending on the thickness of the d-band layer [118, 119, 120]. For SCO, $SrTiO_3$ (STO) is a natural choice as the second component. It is a d^0 insulator with a 3.25 eV band gap and an A-site cation in common with SCO. In addition, the structure of STO can be tuned by epitaxial strain, with different octahedral rotation patterns and polar distortions in compressive and tensile strain[102, 98, 16]; these distortions are expected to influence the structure in the SCO layer.

In this chapter, we present first-principles results for the ground-state phase sequence of the 1:1 $SrCrO_3/SrTiO_3$ superlattice with varying epitaxial strain, with a first-order MIT from a metallic x-type $P2_1/c$ phase to a polar insulating G-type $Pmm2$ phase observed at 2.2% tensile epitaxial strain. We show that the insulating character arises

from orbital ordering induced by a polar distortion in the SCO layer. The polar distortion is shown to be stabilized by a combination of epitaxial strain and the polar distortion in the adjacent STO layer. This offers the possibility of driving the system through the MIT by an applied field or stress that coupled to the polar mode.

5.2 Methods

Our first-principles calculations were performed using the local density approximation[22, 92] with Hubbard U (LDA+U) method implemented in the *Vienna Ab initio Simulation Package* (VASP-5.2[26, 27]). We used the Dudarev implementation[34] with effective on-site Coulomb interaction $U = 1.5$ eV to describe the localized $3d$ electron states of Cr atoms. The projector augmented wave (PAW) potentials[30, 31] contain 10 valence electrons for Sr ($4s^2 4p^6 5s^2$), 12 for Cr ($3p^6 3d^4 4s^2$)10 for Ti ($3p^6 3d^2 4s^2$) and 6 for O ($2s^2 2p^4$). $\sqrt{2} \times \sqrt{2} \times 2$ and $2 \times 2 \times 2$ cells were used to allow the structural distortions and magnetic orderings for the 1:1 superlattice. 500 eV energy cutoff, $4 \times 4 \times 4$ k mesh and 5×10^{-3} eV/Å force threshold were used for structural relaxations. A $15 \times 15 \times 11$ k-point mesh was used for density of state calculations. Our calculations give $a = 3.812$Å for the relaxed tetragonal state of C-AFM $SrCrO_3$, consistent with the previous first-principles and experimental studies[115, 114], with aspect ratio $c/a = 0.964$ slightly smaller than the experimental value of 0.99. The epitaxial strain value is defined with respect to 3.849Å, the computed lattice constant of the cubic STO. The effects of epitaxial strain were studied through "strained bulk" calculations[121].

5.3 Results and discussion

5.3.1 1:1 superlattice

At each value of epitaxial strain in the range -4% - 3%, we determined the ground state (GS) structure of the superlattice using the "stacking method" [16]. This involved combining the computed low-energy structures of epitaxially strained STO and SCO to obtain a set of starting structures, which were then relaxed to the nearest energy minimum using first-principles calculations. To obtain the low-energy structures of

SCO, we considered F, G, A, and C-type AFM ordering in the tetragonal phase with various distortions. C-AFM was found to be the ground state magnetic ordering in the full range of epitaxial strain considered. For C-AFM and FM states, $P4/mmm$ is the GS structure. For G-AFM, $P4/mmm$ is the GS from -4% to 0%, $P4/mbm$ Jahn-Teller (JT)[122, **?**] distortion is the GS beyond 0% and anti-polar distortion $Pmcm$ is also unstable beyond 2%. For A-AFM, $P4/mmm$ is the GS from -4% to 0%, $P4/mbm$ JT distorted structure is the GS beyond 0%, and polar distortion $Pmm2$ is the unstable beyond 3%. The low-energy structures of epitaxially-strained STO have been previously discussed in the literature[102, 98, 16]. We use the low-energy structures of STO listed in Table I of Ref. [16], consistent with the reports in other studies. When the epitaxial strain is within -1% - 1%, the low-energy structures of STO are generated by the M and R point octahedral rotations. For compressive epitaxial strain greater than -1%, the out-of-plane polar mode becomes unstable, while the in-plane rotations are suppressed. For tensile epitaxial strain greater than 1%, the main distortions are in-plane polar modes along [110] and [100] and out-of-plane rotations are suppressed.

To include magnetic ordering in the stacking method for the 1:1 superlattice, we consider three magnetic phases for the single layer of SCO that can fit in the 2×2 lattice, as shown in Fig. 5.1(a). The three phases are FM, G-AFM for the checkerboard ordering in the CrO plane, and x-type AFM for the AF ordering along [100] and FM along [010] in the CrO plane. For each magnetic state of SCO and each value of epitaxial strain, we generate the starting structures by following the procedures of the stacking method. We also carry out relaxations for a small number of random starting structures[16]. Thes show that from -3% to -1% epitaxial strain, the JT distortion is found in the SCO layer, while it is not metastable in the bulk state.

In Fig.5.1(b) we plot the total energies of the GS of the superlattice obtained by the "stacking method" for the three magnetic states versus epitaxial strain. From -3% to 2.2%, the x-AFM is the GS magnetic state, as expected from the resemblance of magnetic ordering to the bulk C-type AFM state. Beyond 2.2%, the GS magnetic state changes to G-AFM.

It is instructive to examine the epitaxial strain dependence of the structure for each

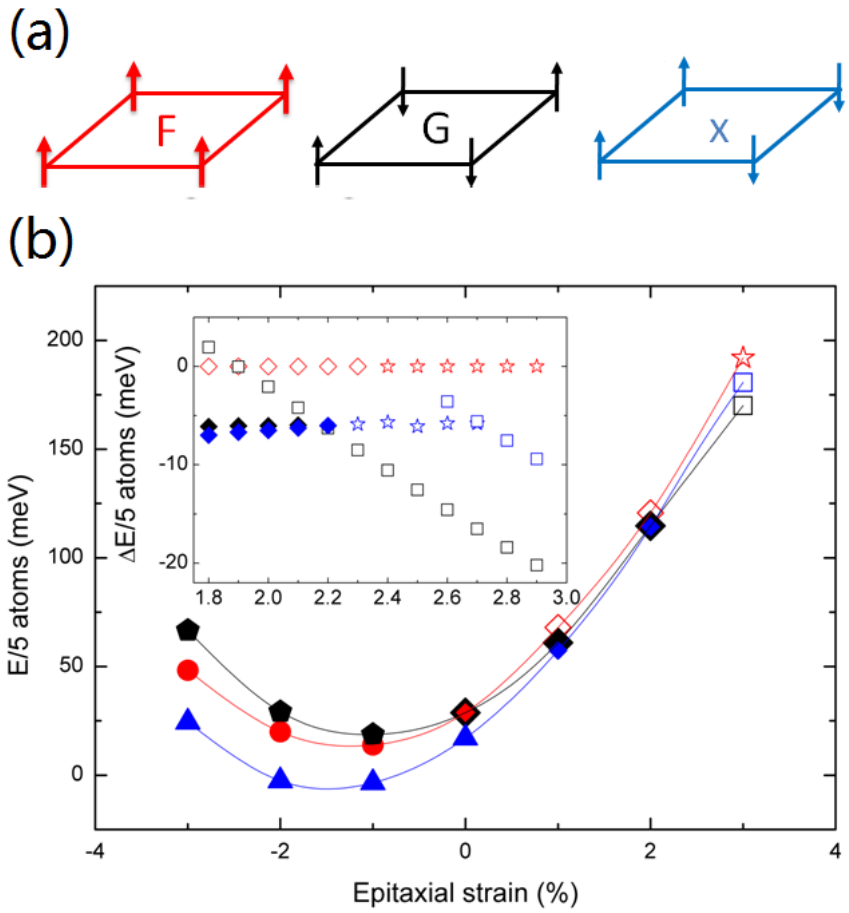

Figure 5.1: (a) Magnetic orderings in the SCO layer. Red: ferromagnetic (F), black: G-AFM (G), and blue: x-type AFM (x) states. (b) GS structures and energies for F (red), G (black), and x (blue) magnetic states as functions of epitaxial strain. The solid curves guide the eye. Insulating and metallic states are denoted by open and solid symbols. Shapes of data points indicate the space groups: pentagons ($Pbam$), triangles ($P2/m$), circles ($P4/mbm$), diamonds ($P2_1/c$), five-pointed stars (Pc) and squares ($Pmm2$). The inset shows the energies of low energy structures relevant to the F state in the epitaxial strain range 1.8% to 2.9%.

magnetic ordering. For FM state, from -3% to 0%, $P4/mbm$ structure with the $a^0a^0c^-$ oxygen octahedral rotation pattern is the lowest energy structure in this phase. From 0% to 2.3%, the lowest energy structure is $P2_1/c$, with an $a^-a^-c^-$ rotation pattern and JT Q_2 mode. The amplitude of the Q_2 mode is about 1% of the lattice constant and does not change much with the strain. As the tensile epitaxial strain increases, the $a^0a^0c^-$ rotation decreases while the $a^-a^-c^0$ increases. Beyond 1%, the lowest energy structure of FM state is insulating. Beyond 2.3%, the lowest energy structure is Pc, with the $a^-a^-c^0$ rotation and small and decreasing amount of $a^0a^0c^-$ rotation, JT Q_2 mode in the SCO layer, and polar distortions along [110].

For the G-AFM state, from -3% to -1%, $Pbam$ is the lowest energy structure, with the $a^0a^0c^-$ rotation mainly in the STO and JT Q_2 distortion in the SCO layer. The JT distortion amplitude is small but enough to lift the d_{yz} d_{xz} degeneracy. However, the system is still metallic due to the band overlap. From 0% to 2.2%, $P2_1/c$ with the $a^-a^-c^-$ oxygen octahedral rotation pattern and JT Q_2 mode is the lowest energy structure. Beyond 2.2%, the polar structure $Pmm2$, with only polar distortion along [100] becomes the lowest energy structure, leading to the insulating overall GS, with magnetic moment 1.8 μ_B.

For the x-AFM state, from -3% to 0%, the lowest energy structure is nonpolar $P2/m$, with $a^0a^0c^-$ rotation mainly in the STO layer, and small JT Q_2, Q_3 modes in the SCO layer. From 0% to 2.2%, the lowest energy structure is $P2_1/c$. Beyond 2.2%, the lowest energy structure is insulating. In particular, from 2.2% to 2.7%, the lowest energy structure is Pc with the $a^-a^-c^0$ rotation and a small and decreasing amount of $a^0a^0c^-$ rotation, JT Q_2 mode in the SCO layer and polar distortion along [110]. The in-plane rotation is now the main distortion pattern, and the amplitudes for both STO and SCO layers are similar, due to the connection of oxygen octahedra. Beyond 2.8%, the lowest energy structure changes to $Pmm2$.

The phase boundary at 2.2% epitaxial strain is of particular interest. The inset of Fig. 5.1 shows the energies for F, G, and x structures for $1.8\% - 2.9\%$ epitaxial strain. The energy of the G-type polar $Pmm2$ structure decreases relative to that of the x-type nonpolar $P2_1/c$ structure with increasing epitaxial strain, with a first-order transition

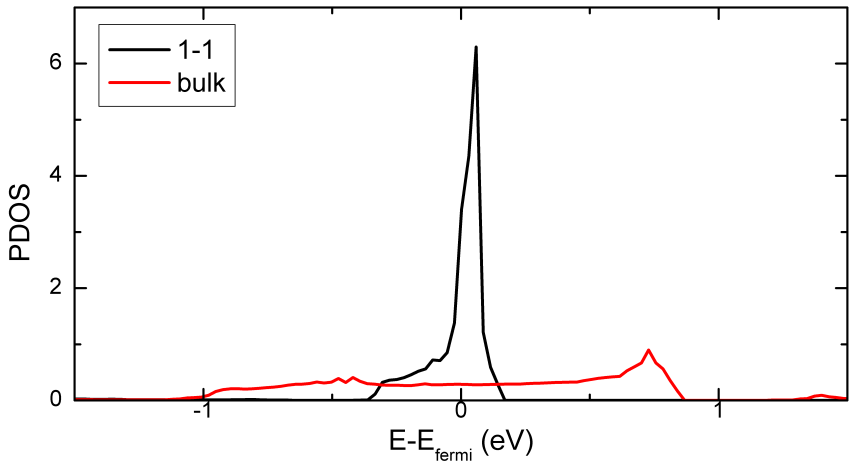

Figure 5.2: The PDOS of the Cr d_{yz} orbital for G-type 1:1 SCO/STO superlattice and C-type bulk SCO.

at 2.2% epitaxial strain. We note the metal-insulator transition associated with the change from the nonpolar to the polar structure.

To figure out the mechanism of the insulating phase in the 1:1 superlattice beyond 2.2% epitaxial strain, we first consider the effect of the superlattice layering on the bands near the Fermi level. It eliminates the dispersions of Cr t_{2g} bands along k_z, and significantly narrows the band widths of d_{yz} and d_{xz}. Fig. 5.7 shows the PDOS of d_{yz} of one Cr atom in the G-type 1:1 superlattice and C-AFM bulk SCO for 3% tensile epitaxial strain in the $P4/mmm$ symmetry. The 1:1 superlattice is metallic for the $P4/mmm$ structure, with the d_{yz} band much narrower than in the bulk case. The thickness of the STO layer has little effect. Our calculations show that the Cr-layer structure and bands are very similar for 1:1 and 1:3 superlattices.

Next, we consider the coupling effect of the polar distortion to the superlattice insulating $Pmm2$ state. The $Pmm2$ structure is generated from the high symmetry reference structure by the doubly-degenerate in-plane E_u polar distortion, with eigenvector (0.00, 0.00, −0.15, 0.08, 0.53, 0.53, 0.37, 0.40, 0.06, 0.33) specifying the displacement pattern of the atoms (Sr, Sr, Cr, Ti, O_{z1}, O_{z2}, O_{x1}, O_{x2}, O_{y1}, O_{y2}). From 2.2% to 3%, the band gap increases from 0.27 to 0.47 eV, and the polarization increases from 36 to 41 $\mu C/cm^{-2}$.

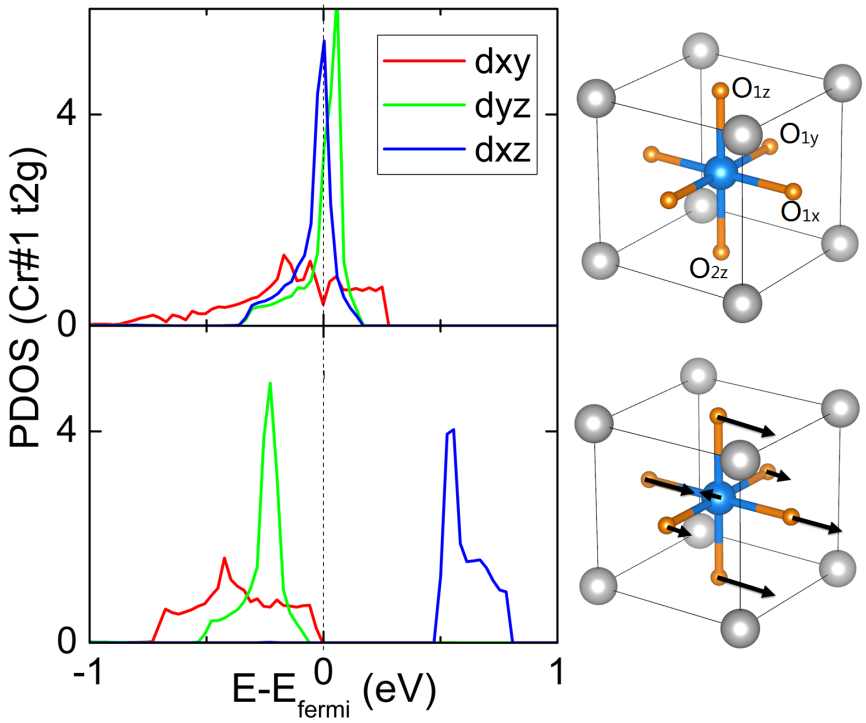

Figure 5.3: PDOS of the spin up Cr t_{2g} in the 1:1 superlattice for +3% strain, with G-AFM magnetic ordering. The left panels represent the PDOS without (top) and with (bottom) the polar distortion. The vertical dashed line marks the energy of the highest occupied state. The distortions in the SCO layer are shown on the right part, where gray, blue and orange spheres represent Sr, Cr and O ions, respectively.

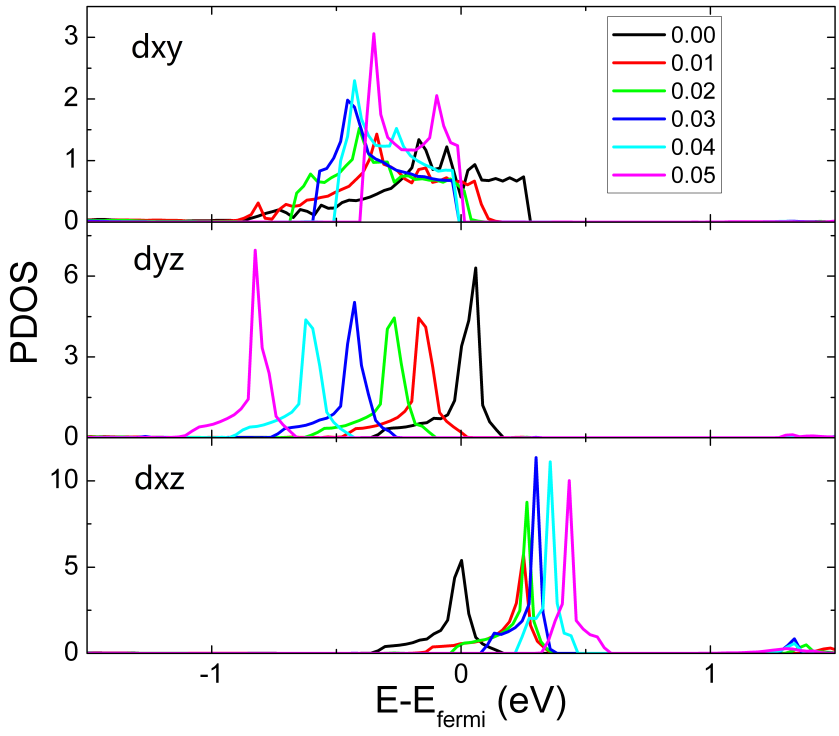

Figure 5.4: The evolution of PDOS of Cr d_{xy}, d_{yz} and d_{xz} as a function of polar displacement of Cr ion in [100]. The amplitude of the displacement for each curve is given in the legend in units of the in-plane lattice constant.

The effects of the in-plane polar distortion on the electronic structure of the superlattice are evident from the projected density of states (PDOS) of the t_{2g} bands of the spin up Cr atom, shown in Fig. 5.3. The layered structure of the superlattice splits d_{xy} from d_{xz} and d_{yz} and increasing tensile epitaxial strain lowers the energy of the d_{xy} orbital relative to d_{yz} and d_{xz}. At 3% epitaxial strain, in the undistorted structure, all three d orbitals are partially occupied. The in-plane polar distortion lifts the degeneracy of d_{yz} and d_{xz}, so that in the polar $Pmm2$ state the d_{xy} and d_{yz} orbitals are fully occupied while d_{xz} is unoccupied, corresponding to $d^1_{xy}d^1_{yz}d^0_{xz}$ orbital ordering.

In fact, the OO can be produced by polar displacements just of the Cr atoms. To show this, we consider a $Pmm2$ 1:1 SCO/STO superlattice, in which only the Cr atoms are uniformly displaced along [100], while all other atoms stay at the high symmetry positions. In Fig. 5.4 we show the PDOS of the distorted superlattice as a function

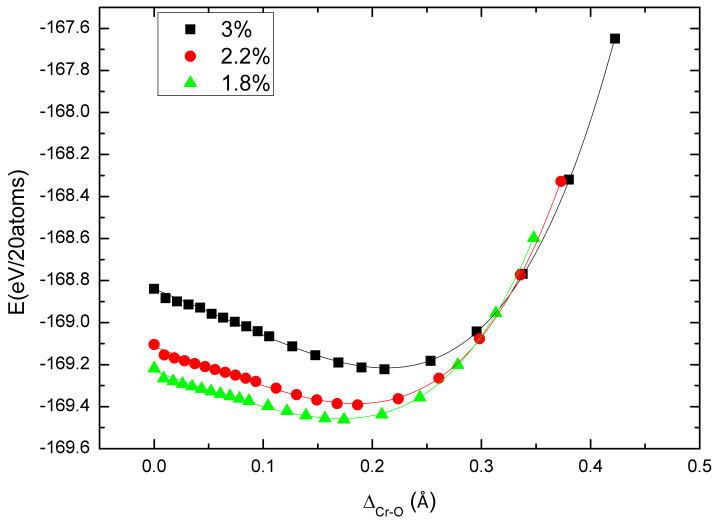

Figure 5.5: Decomposed polar mode energies for three epitaxial strain cases.

of Cr displacement. There is a dramatic downward shift of the d_{yz} with increasing displacement, accompanied by a smaller upward shift of d_{xy} and a decrease in the d_{xy} bandwidth.

Finally, we discuss why the in-plane polar distortion becomes the GS for tensile strain. Our calculations show that for any distortion that lifts the d_{yz} and d_{xz} degeneracy, there is a energy gain. This explains the emergence of JT distortions in $P2_1/c$ or *Pbam* structures for the 1:1 superlattice. However, in general, for large tensile epitaxial strain, the in-plane polar state is likely to be more favorable than the JT distortion due to the well-known polarization-strain coupling. In Fig. 5.5 we compare the energies of the decomposed polar mode for 1.8% 2.2% and 3% epitaxial strain cases. As the tensile strain increases, the energy gain from the inplane polar mode also increase. Also, the polar mode is very soft. If we fit the decomposed mode with polynomials, the second order coefficient becomes from positive for 1.8% to negative for 3% epitaxial strain. It shows that in the large tensile strain this polar mode is unstable.

However, JT distortion does not show instability in tensile epitaxial strain. In Fig. 5.6 we plot the energy of decomposed JT distortion for the 2.2% epitaxial strain

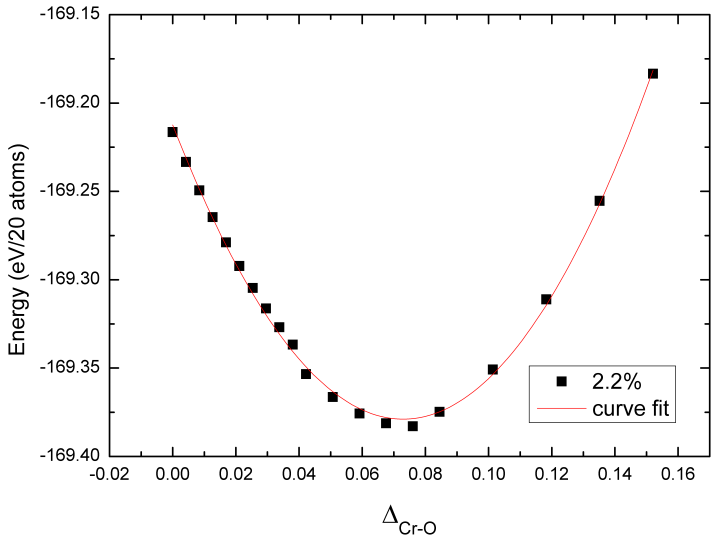

Figure 5.6: Decomposed polar mode energies for three epitaxial strain cases.

case. The curve shows a positive second order coefficient, suggesting only a linear energy gain.

The other reason for the polar ground state structure is the polar distortion in the STO layer. To show this, we fixed the STO layer in a nonpolar structure for 3% strain, froze in the in-plane polar mode and JT distortion in the CrO_2 layer in turn, and relaxed. Distortions survive in both cases and the relaxed structure with JT distortion has lower energy, suggesting that the in-plane polar mode in the STO coupled differently to the in-plane polar mode and the JT mode in the SCO layer.

This insulating state also raises the possibility of controlling band gap by applied electric field. Given the SCO/STO superlattice in the insulating state, an in-plane electric field will change the atomic positions, and hence change the band gap, because the band gap is sensitive to the displacement of the Cr atom relative to the O atoms around it.

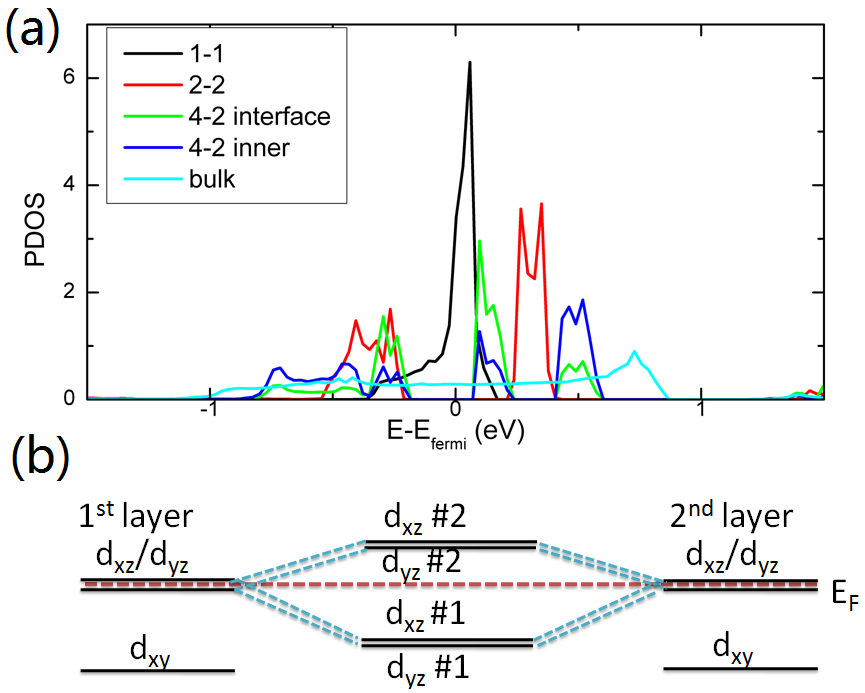

Figure 5.7: (a) PDOS of d_{yz} orbitals for bulk SCO and different periods of SCO/STO superlattices. (b) A sketch for the bonding/antibonding states for d_{yz} or d_{xz} between different Cr layers.

5.3.2 Thicker superlattices

The thickness also play an important role to the electronic state of the superlattice. When the number of layers of $SrCrO_3$ is larger than 1, bonding/antibonding states of Cr d_{yz} or d_{xz} between different Cr layers are possible for the C-AFM state. In Fig. 5.7 we plot the PDOS of the Cr d_{yz} orbital. It shows that compare to the bulk state, in the superlattice, the d_{yz} bands are very narrow, similar to the 1:1 superlattice care. However, in the 2:2 case for example, the bonding and antibonding states arise, leading to two occupied d_{xy}, one occupied d^B_{yz} and one occupied d^B_{xz}. So the superlattice is insulating even without the polar mode or JT distortion. On the other hand, the inplane polar mode and JT distortion that can lift the d_{yz} and d_{xz} degeneracy do not gain linear order of energy in this case, and therefore we cannot have them in the superlattice after structural relaxations.

Fig. 5.7(a) also shows the 4:2 SCO/STO superlattice case. For these superlattices with thick SCO layers, the hybridizations among Cr layers are even more complicated. For the 4:2 case we can see that 4 levels are formed, with half of them occupied. As the number of SCO layers increases, the hybridized energy level increases, and the band gap between them will be reduced. Keeping increasing the SCO layer in the superlattice, and eventually the DOS will coincide with the bulk case.

The thickness of STO layer is however not so critical to the electronic structure near the Fermi energy. We have calculated the 1:3 and 2:4 superlattices, and their band structures and DOS near the Fermi energy are similar to the 1:1 and 2:2 superlattices, respectively.

5.4 Summary

In summary, we have studied both the lattice and electronic structures of the ground state for the 1:1 SCO/STO superlattice. Distortions in SCO layers are established by the superlattice layering with STO. For tensile epitaxial strain, due to the in-plane polar distortion associated with nonzero Cr displacements, the $d^1_{xy}d^1_{yz}d^0_{xz}$ orbital ordering can

be formed and the band gap is therefore induced. The polar distortion induced metal-insulator transition can be used to engineer the SCO band structures near the Fermi level. Our study sheds light on a new way to control electronic band structures and approach the metal-insulator transition point.

Chapter 6

Transparent conducting $SrVO_3$ thin film

Transparent conductor is electrically conductive and optically transparent. It is a crucial component of many electronic devices, including touch screens, high definition televisions (HDTVs) and photovoltaics. Thus there is a huge market of transparent conductors over twenty billion dollars. Currently the best and mostly used transparent conductors are indium tin oxides (ITOs). However, to keep enhancing the performance, and to avoid the expensive indium, a large number of studies have been carried out to look for substitutes of ITOs. The conventional paradigm to combine high electrical conductivity and high optical transparency in the visible spectrum is to begin with a wide band gap semiconductor with low electron effective mass and to increase its conductivity by degenerate doping. Our experimental collaborators (Roman Engel-Herbert's group at Penn State) recently found that the metallic correlated transition metal oxide, $SrVO_3$, is highly transparent for visible and near-infrared light under 100 nm thickness. This may introduce a new material design concept for transparent conductors by beginning with a highly conducting, correlated metal. The strong electron-electron interaction causes an enhancement of the electron effective mass, which makes plasma frequency shift to lower energy. In addition, when interband transitions within the visible light range are suppressed by the small transition matrix or Fermi factor, the light absorption in the visible range will be suppressed, directly benefiting optical transparency without compromising electrical conductivity. In this chapter, we calculate the band structure, interband transitions and dielectric functions of $SrVO_3$ from first principles, and the results of dielectric functions are in good agreement with experimental data. Our results indicate the robustness of this design concept, opening up new avenues for designing transparent conductors in other correlated metals.

6.1 Introduction

Transparent conductors are extremely rare. A good transparent conductor should have good electric conductivity and meanwhile good transparency for visible light. These two properties contradict to some extent. The conductivity $\sigma = en\mu = e^2\tau n/m^*$ is related to the density n and mobility μ of carriers, where the mobility can be determined by the carrier scattering τ and effective mass m^*. Hence to enhance the conductivity large n/m^* and τ are desired. For conductors, when the frequency of light is less than the plasma frequency $\hbar\omega_p = \hbar e\sqrt{\frac{n}{m^*\epsilon}}$, the light will interact with the carriers, lead to intraband transitions and will not be transmitted through. Thus the plasma frequency has to be suppressed below the visible light range (1.55 eV) and a small n/m^* value is desired. The current design strategy the transparent conductors is to balance the trade-offs between n, m^* and τ by doping wide band gap (> 3.25 eV) semiconductors, most of which are transparent conductive oxides (TCOs), ZnO- or indium tin oxide (ITO-) based materials[123, 124]. High dopant concentrations necessarily lead to the additional scattering contributions and lower the scattering time τ, and thus lead to an intrinsic limit to optimize the performance.

$SrVO_3$ (SVO) is a paramagnetic metal at room temperature. It has recently been found by our colleagues to be transparent for thin film states (< 100 nm), and with even better performance than conventional thin film TCOs. SVO is a new type of transparent conductors. It has a low plasma frequency, 1.58 eV, possibly due to the strong correlation effect [125]. Meanwhile, SVO avoids the doping issue. It is a metal with conductivity $\sigma = 3.3 \times 10^4$ S/cm for the 45 nm thin film, better than ITOs. Most importantly, the amplitudes of interband transitions within the visible light energy range have been suppressed for the high transparency of thin film SVO.

In this chapter, I carry out a detailed first-principles study on strained SVO to investigate the reason of suppressed interband transitions. I calculate the dielectric functions and simulate the transmittance of light for thin film SVO, and the results are in good agreement with experimental data. I analyze the electronic band structure and the interband transitions. The results show that within the visible light range, there

exist interband transitions with small transition matrix that have tiny contribution to the light absorption, and those with large transition matrix but are blocked by the Fermi factor.

6.2 Method and formalism

Our first-principles calculations of $SrVO_3$ were performed using the generalized gradient approximation (GGA) with the Perdew-Becke-Erzenhof parameterization [62] as implemented in the *Vienna Ab initio Simulation Package* (VASP-5.2.12) [26, 27]. The projector augmented wave (PAW) potentials [30, 31] used contained 10 valence electrons for Sr ($4s^2 4p^6 5s^2$), 13 for V ($2s^2 2p^6 3d^3 4s^2$) and 6 for O ($2s^2 2p^4$). We used 500 eV as the energy cutoff. An $8 \times 8 \times 8$ Monkhorst-Pack k-point mesh was used for the structural relaxation, and a $31 \times 31 \times 31$ Γ centered k-mesh was used for the interband transition calculation. Extensive testing with the GGA+U method with nonzero U and ferromagnetic, G-type antiferromagnetic and nonmagnetic configurations showed that the relevant features of the band structures and interband transitions are not sensitive to U or the magnetic ordering. For U=0, the ground state was found to be non-magnetic. Since $SrVO_3$ is paramagnetic at room temperature, we performed the analysis for the nonmagnetic state with U=0. The c lattice parameter of the tetragonal five-atom unit cell was relaxed with in-plane lattice constant fixed to the experimental value 3.868Å, preserving P4/mmm symmetry, yielding a value for c/a ratio of 0.979.

The plasma frequency was calculated from the band structure using

$$\omega^2_{p,\alpha\beta} = \frac{4\pi e^2}{V\hbar^2} \sum_{n,\mathbf{k}} 2g_{\mathbf{k}} \frac{\partial f(E_{n\mathbf{k}})}{\partial E} (\mathbf{e}_\alpha \frac{\partial E_{n\mathbf{k}}}{\partial \mathbf{k}})(\mathbf{e}_\beta \frac{\partial E_{n\mathbf{k}}}{\partial \mathbf{k}}) \tag{6.1}$$

where α, β denote the direction, V denotes the volume of the unit cell, f is the occupancy function, E is the band energy, $\mathbf{e}$ is the unit vector, and $g_{\mathbf{k}}$ is the weight of $\mathbf{k}$ point. For $SrVO_3$, the plasma frequency is determined by the t_{2g} bands that cross the Fermi level. Since the t_{2g} band structure is relatively simple, the uncertainty in the plasma frequency is determined by the uncertainty in the t_{2g} bandwidth. We have computed band structures for different U and k-meshes, and the t_{2g} bandwidth is found to vary by less than 2%. The uncertainty in can thus be estimated to be about 4% of the

computed value.

The intraband contribution to the dielectric function was obtained empirically from the Drude model,

$$\epsilon^{(1)}_{\text{intra}}(\omega) = 1 - \frac{\omega_p^2}{\omega^2 + \gamma^2}, \tag{6.2}$$

$$\epsilon^{(2)}_{\text{intra}}(\omega) = \frac{\gamma\omega_p^2}{\omega^3 + \omega\gamma^2}, \tag{6.3}$$

$$\gamma = \frac{ne^2\rho}{m_e}. \tag{6.4}$$

Using measured values $\rho = 2 \times 10^{-7}\Omega \cdot \text{cm}$, $n = 2 \times 10^{22}\text{cm}^{-3}$, we estimate $\gamma = 0.1$ eV and $m_e = 4.5m_0$.

The interband contributions to the dielectric functions ϵ_{inter} were calculated using the *VASP* implementation, in the approximation that the local field effects are neglected [126]. The imaginary part is determined by

$$\epsilon^{(2)}_{\text{inter},\alpha\beta}(\omega) = \frac{4\pi^2e^2}{V} \lim_{q\to 0} \frac{1}{q^2} \sum_{c,v,\mathbf{k}} 2w_{\mathbf{k}}\delta(E_{c\mathbf{k}} - E_{v\mathbf{k}} - \omega) \times \langle u_{c\mathbf{k}+\mathbf{e}_\alpha\mathbf{q}}|u_{v\mathbf{k}}\rangle\langle u_{v\mathbf{k}}|u_{c\mathbf{k}+\mathbf{e}_\alpha\mathbf{q}}\rangle \tag{6.5}$$

where V is the volume of the unit cell, the index c and v refer to conduction and valence bands, respectively, and $u_{\mathbf{k}}$ is the cell periodic part of the wavefunction at k-point $\mathbf{k}$. and $\mathbf{e}_\alpha$, $\mathbf{e}_\beta$ denote unit vector in Cartesian directions. $\lim_{q\to 0}\langle u_{c\mathbf{k}+\mathbf{e}_\alpha\mathbf{q}}|u_{v\mathbf{k}}\rangle$ gives the α component of the dipole matrix element between two bands.

The real part of the dielectric function is obtained using the Kramers-Kronig transformation,

$$\epsilon^{(1)}_{\text{inter},\alpha\beta}(\omega) = 1 + \frac{2}{\pi}\text{P}\int_0^\infty \frac{\epsilon^{(2)}_{\text{inter},\alpha\beta}(\omega')\omega'}{\omega'^2 - \omega^2 + i\eta}d\omega', \tag{6.6}$$

where the P means the principal value, and η is a tiny shift.

The refractive index can be calculated using the dielectric functions, and further the reflectivity and absorption rate can also be obtained. From the complex refractive index writes

$$(n + i\kappa)^2 = \epsilon^{(1)} + i\epsilon^{(2)}, \tag{6.7}$$

where n and κ are the real and imaginary parts of the refractive index. Thus,

$$n = \sqrt{\frac{1}{2}(\sqrt{\epsilon^{(1),2} + \epsilon^{(2),2}} + \epsilon^{(1)})}, \tag{6.8}$$

$$\kappa = \sqrt{\frac{1}{2}(\sqrt{\epsilon^{(1),2} + \epsilon^{(2),2}} - \epsilon^{(1)})}. \tag{6.9}$$

Then the reflectivity is

$$R = \frac{(1-n)^2 + \kappa^2}{(1+n)^2 + \kappa^2}. \tag{6.10}$$

Transmissivity at the surface can be calculated as $T = 1 - R$. The absorption rate is a function of reflectivity and κ

$$\lambda = \frac{4\pi\kappa}{R}, \tag{6.11}$$

and the transmittance decreases exponentially with the thickness of the film,

$$\mathcal{T} = T\exp(-\lambda z). \tag{6.12}$$

6.3 Results and Discussion

We first calculate the dielectric functions of the strained bulk $SrVO_3$, with in-plane lattice constant 3.868Å, the experimental value. In Fig. 6.1 we compare the calculations with experimental results. The experimental dielectric functions were measured by Podraza's group at Toledo University via the spectroscopic ellipsometry. In low energy range (< 1.2 eV) there is a discrepancy between the calculation and the experiment. The suppression of the intraband contribution, namely the Drude peak part, to the dielectric functions is related to the electron-electron correlation of $SrVO_3$[125, 127]. Since the GGA we used for the exchange-correlation potential in the calculation does not carefully describe the strong correlation, this may lead to the low energy range discrepancy of dielectric functions. However for higher energy range, including the visible light range, where the interband transitions are the main components for the dielectric functions, our calculation captures the main features. For $1.3 - 2.8$ eV the $\epsilon^{(2)}$ is suppressed, and the main peak is at 3.4 eV as the experimental data. In the rest of the chapter, we focus on the $1.3 - 3.6$ eV energy range and explain the transparency by analyzing the interband transitions.

With the dielectric functions, we can also calculate the transmittance of different thickness thin films using Eq. 6.12. In Fig. 6.2 we show the experimental and calculated

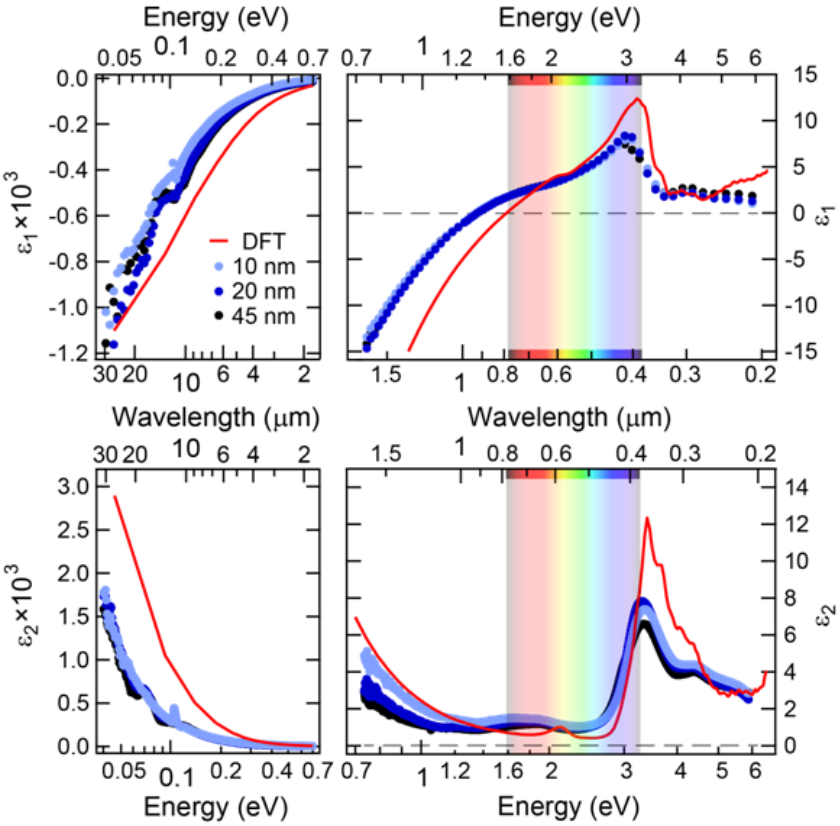

Figure 6.1: Dielectric functions with respect to wavelength. Real part (top panels) and imaginary part (bottom panels). Solid lines are DFT calculated data, and dots represent experimental data. The experimental data is measured by Podraza's group at Toledo University.

transmittance. Both sets of data show that SVO thin films have a high transparency. The transmittance for light with wavelength 400–900 nm, which almost covers the visible light range, is higher than 70% for the 45 nm-thick film. Even if Fig. 6.2 show the transparency in a direct representation, since the experimental results are calculated from the dielectric data in Fig. 6.1, Fig. 6.2 and 6.1 are actually equivalent. As we can see in Fig. 6.2, the calculated transmittance for short wavelength is in a good agreement with experiment, while for the wavelength greater than 900 nm, the calculated transmittance is more suppressed than the experimental value.

A key requirement for optical transparency is that the contributions of interband transitions must be suppressed in the optical range, either by the absence of transitions

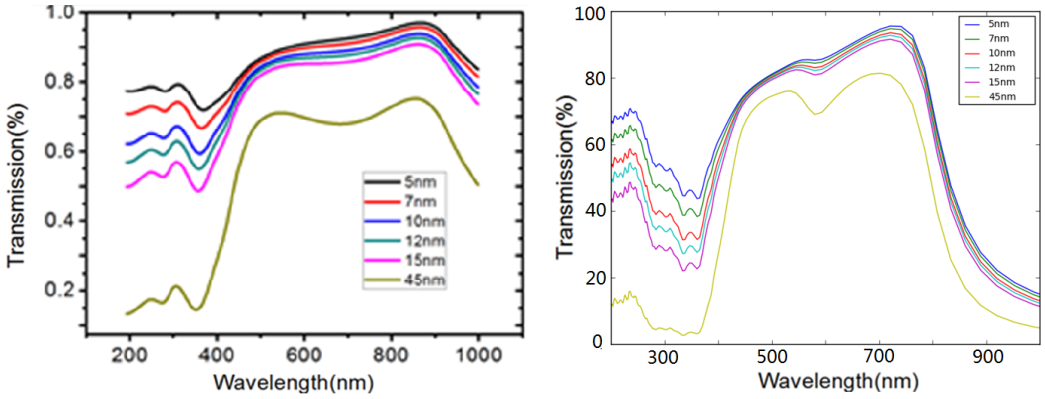

Figure 6.2: Transmittance of thin film $SrVO_3$. Left, experiment. Right, first-principles calculation.

with the relevant energies or by the suppression of their contribution by the Fermi factor, matrix elements and/or joint density of states.

Here, we analyze the interband transitions in $SrVO_3$ via first principles calculations of the band structure of $SrVO_3$ and the dipole transition matrix elements for the optical transitions between bands. The three relevant sets of bands yielding interband transitions below 3.6 eV are shown in Figure 6.3(A): the valence band, dominated by oxygen $2p$ orbitals; the lowest conduction band, predominantly V t_{2g}; which lies at the Fermi level, and the higher-lying conduction band, derived from the V e_g orbitals. Fig. 6.3(B) shows the sheets of the Fermi surface, with the bands from Γ to X clearly differentiating the outer sheet from the two inner sheets. Thus the interband transitions of interest are $t_{2g} - t_{2g}$, $t_{2g} - e_g$ and $2p - t_{2g}$ transitions. Fig. 6.4 shows the imaginary dielectric function $\epsilon^{(2)}$ decomposed into the above three sets of interband transitions.

Interband transitions from filled t_{2g} to empty t_{2g} states occur at low energy, below 1 eV. In Fig. 6.4 it is shown that the contribution of $t_{2g} - t_{2g}$ interband transitions are within the Drude peak. The transition matrix elements and energy difference along the band structure k path are shown in Fig. 6.5. The matrix elements for $t_{2g} - t_{2g}$ transitions can be extremely large, possibly due to the degenerate t_{2g} bands in those areas, for which the eigenfunctions are similar, leading to the large $\langle u_{c\mathbf{k}+\mathbf{e}_\alpha\mathbf{q}} | u_{v\mathbf{k}} \rangle$. However, they are not contribution because of the same Fermi factor.

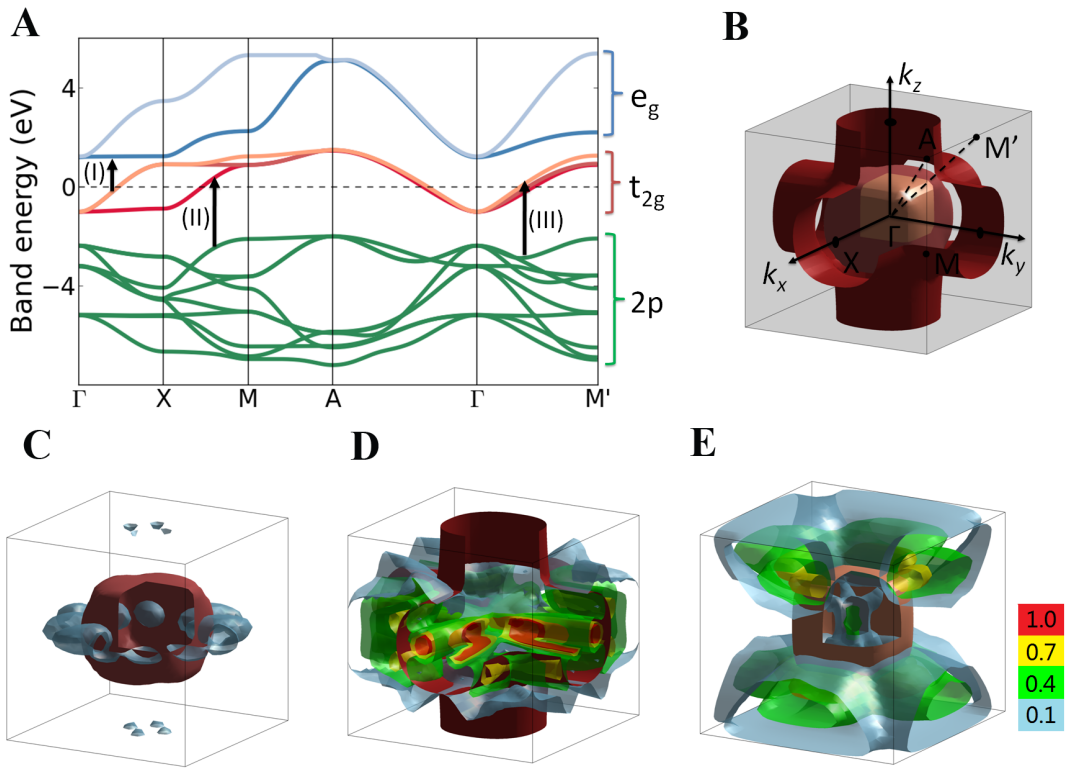

Figure 6.3: First principles calculation results of $SrVO_3$. (A) Band structure of $SrVO_3$ in the vicinity of the Fermi level E_F, comprised of nine bands originating from O $2p$ orbitals, three bands from V $3d$ t_{2g}, and two bands from V $3d$ e_g orbitals. Interband transition (I) through (III) are indicated. (B) Brillouin zone of $SrVO_3$ containing the Fermi surfaces of the three t_{2g} bands. Isosurface representation of the dipole matrix element M^2 for electronic states in the Brillouin zone for the interband transitions. (C) (I): t_{2g}^2 to e_g^1, (D) (II): $2p^1$ to t_{2g}^1, (E) (III): $2p^1$ to t_{2g}^3 with $2p^1$ the highest lying valence band, t_{2g}^1, t_{2g}^2, t_{2g}^3 the lowest middle and highest lying t_{2g} bands, and e_g^1, e_g^2 the lowest, highest lying e_g bands, respectively. The Fermi surface of the t_{2g} band involved in the transition is indicated as well.

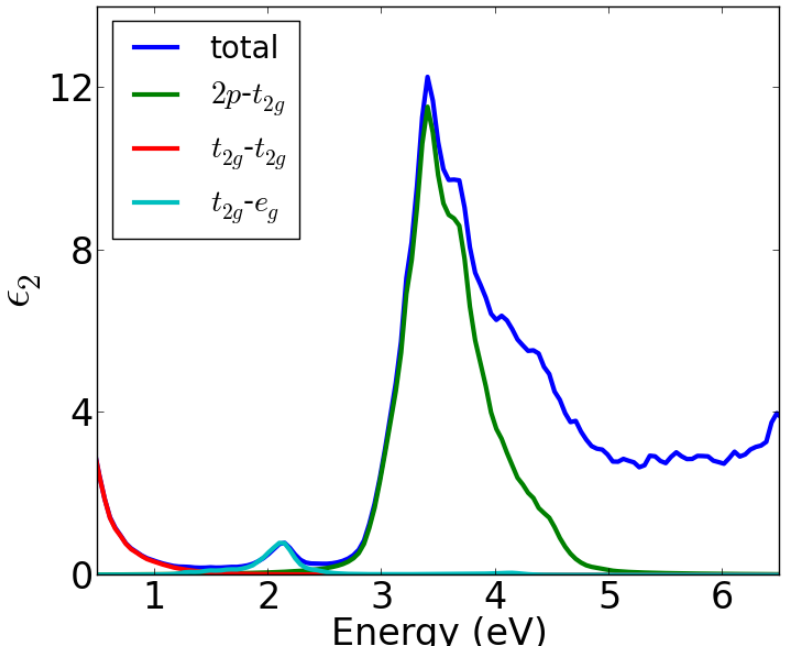

Figure 6.4: Decomposed $\epsilon^{(2)}_{\text{inter}}$ to $2p - t_{2g}$, $t_{2g} - t_{2g}$ and $t_{2g} - e_g$ contributions.

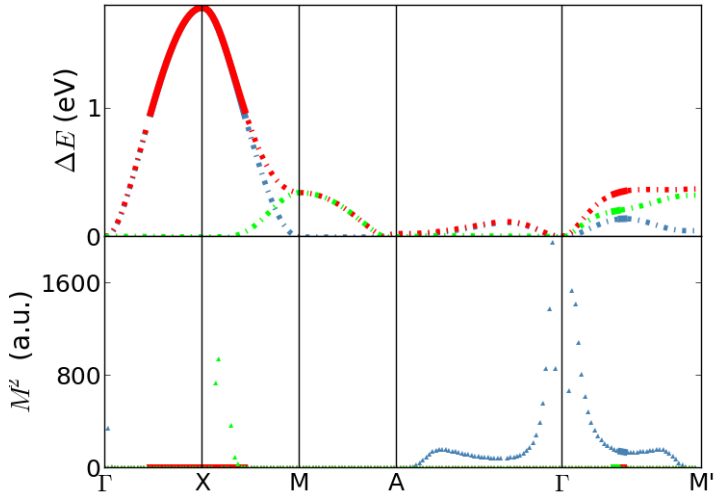

Figure 6.5: Energy difference (upper panel) and M_z^2 (bottom panel) for $t_{2g} - t_{2g}$ transitions along the k path of Fig. 6.3(A). Solid and dotted lines represent the allowed transitions and those forbidden by the Fermi factor. Blue, red and green represent transitions of $t^1_{2g} - t^2_{2g}$,$t^1_{2g} - t^3_{2g}$ and $t^2_{2g} - t^3_{2g}$.

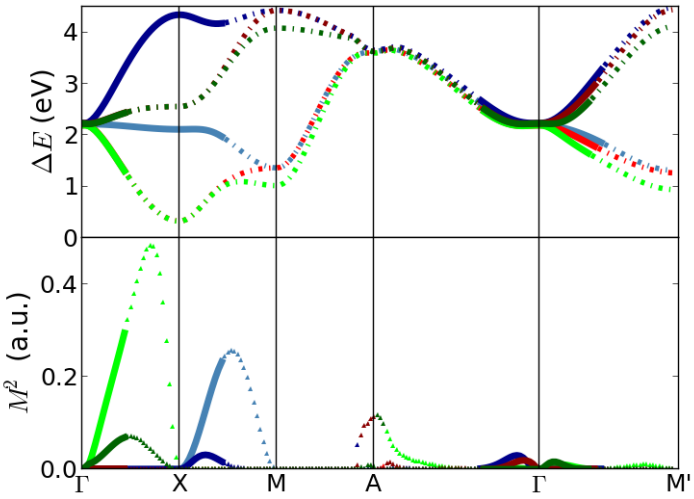

Figure 6.6: Energy difference (upper panel) and M_z^2 (bottom panel) for $t_{2g} - e_g$ transitions along the k path of Fig. 6.3(A). Solid and dotted lines represent the allowed transitions and those forbidden by the Fermi factor. Blue, red and green represent transitions start from t_{2g}^1 t_{2g}^2 and t_{2g}^3. The light and dark blue, red and green represent the transitions end in e_g^1 and e_g^2, respectively.

The interband transitions between the V t_{2g} bands and the e_g bands lie in an energy range of 1.3 to 4.3 eV, and mainly contribute to the small peak at 2.1 eV in Fig. 6.4. The transition matrix elements and energy difference along the band structure k path are shown in Fig. 6.6. To see the transition matrix within the Brillouin zone, we plot M_z^2 of middle t_{2g} to the lower e_g, $t_{2g}^2 - e_g^1$ transitions (marked I in Fig. 6.3(A)) in an isosurface representation in Figure 6.3(C). Only the wavevectors inside the Fermi surface sheet shown correspond to filled-to-empty transitions and contribute to the optical absorption; the small matrix element factor for these transitions suppresses the resulting peak in the imaginary part of the dielectric function, as shown in Fig. 6.4. It can be seen that the matrix elements are substantially larger for transitions at wavevectors just outside the Fermi sheet, so that the exact location of the Fermi level in the t_{2g} bands is critical in suppressing the contribution of the t_{2g} to e_g transitions in the visible range.

Finally, we consider the interband transitions from the filled valence band to the

empty t_{2g} band states, which contribute the main peak of $\epsilon^{(2)}$ at 3.4 eV as shown in Fig. 6.4. (The interband transitions from the filled valence band to the e_g band are higher than 3.6 eV). The transition matrix elements and energy difference along the band structure k path are shown in Fig. 6.7. We can find that large matrix elements near Γ point is not allowed due to the Fermi factor, and the main contribution comes from several sets of $2p-t_{2g}$ transitions. As an example of the computed matrix elements in the Brillouin zone, we plot the transitions M_z^2 from the highest valence band to the lower t_{2g}, $2p^1 - t_{2g}^1$ band (marked II in Fig. 6.3(A)) in Fig. 6.3(D). The filled-to-empty transitions are at wavevectors outside of the Fermi surface sheet, where the matrix elements are relatively small. The energy for filled-to-empty transitions ranges from 2.8 eV to 3.4 eV, with the largest matrix elements (yellow isosurfaces) just outside the Fermi surface sheet. This is in dramatic contrast to the much larger matrix elements inside the sheet (red isosurfaces), which correspond to filled-to-filled transitions in the energy range 1.3 - 2.8 eV and thus do not contribute to optical absorption. We also plot M_z^2 for the transitions from the highest valence band to the upper t_{2g} band, $2p^1 - t_{2g}^3$ (marked III in Fig. 6.3(A)) in Fig. 6.3(E). States located just outside the Fermi surface gave rise to the strong absorption peak at 3.4 eV. From this, we see that here too, the exact location of the Fermi level in the t_{2g} bands is critical in suppressing strong transitions in the visible range.

Transparent conducting $SrVO_3$ thin film is a great start, and we then propose ways to tune and improve the transparency. We note that for $SrVO_3$ the Fermi factor ensures a near-zero optical absorption from interband transitions in the energy range 2.1 eV and 2.8 eV. Thus, manipulating band position, Fermi surface size and shape via epitaxial strain, and manipulating band dispersion via doping on the A-site cations are reasonable strategies to enhance the transparency.

Furthermore, to search for other candidates of transparent conductors within transition metal oxides, there are several keys noteworthy. 1. As $p - d$ transitions, the $2p - t_{2g}$ transitions matrix are usually greater than the $t_{2g} - e_g$ transition matrix and contribute to the main absorption peak of interband transitions. So the energy difference of $2p - t_{2g}$ bands should be large enough to avoid absorptions in the visible light

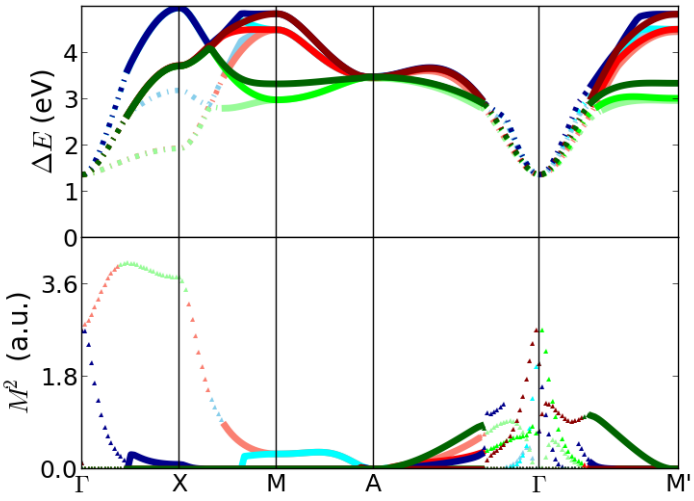

Figure 6.7: Energy difference (upper panel) and M_z^2 (bottom panel) for $2p - t_{2g}$ transitions along the k path of Fig. 6.3(A). Solid and dotted lines represent the allowed transitions and those forbidden by the Fermi factor. Blue, red and green represent transitions start from the lowst p, $2p^3$ to the highest p, $2p^1$. The light to dark blue, red and green represent the transitions end in t_{2g}^1, t_{2g}^2 and t_{2g}^3, respectively.

range. To achieve this, except choosing an appropriate material, we can use epitaxial strain to tune the energy levels of d and p bands. Also, the band engineering via polar distortion of the B-site transition metal atom relative to the oxygen octahedron studied in the previous $SrCrO_3/SrTiO_3$ example provides another possibility.

2. It is not shown that $t_{2g} - e_g$ contribution is always small, thus it would be a good idea to push the $t_{2g} - e_g$ energy difference outside or to the edge of visible light energy range. The $t_{2g} - e_g$ band gap can be tuned by the crystal field, namely by epitaxial strain. The tetragonal effect further splits the d_{xy} from d_{yz}/d_{xz} in t_{2g}, and $d_{x^2-y^2}$ from d_{3z^2-r2} in e_g, so that the band gap between the higher t_{2g} and the lower e_g can be manipulated, and thus the position of the small $\epsilon^{(2)}$ peak within the visible light range can be optimized.

3. The width of the Drude peak should be suppressed, which is usually true for transition metal oxides where the correlation effect is strong.

6.4 Summary

In summary, we have studied in depth the interband transitions of $SrVO_3$. I have found three sets of transitions, $t_{2g} - t_{2g}$, $t_{2g} - e_g$, and top $2p - t_{2g}$ that are within the visible light range. Some $t_{2g} - t_{2g}$ transitions show large transition matrix elements due to the similar eigenfunctions, but are in low energy less than 1 eV. The $t_{2g} - e_g$ transitions have overall small transition matrix. Those with largest transition matrix are blocked by the Fermi factor, leading to the small $\epsilon^{(2)}$ peak at 2.1 eV. This is the main reason for the good transparency of $SrVO_3$. $2p - t_{2g}$ transitions have large joint density of states and transition matrix, leading to the $\epsilon^{(2)}$ main peak at 3.4 eV. By tuning the Fermi level, or using epitaxial strain to change the Fermi surface or orbital energy levels, the optical properties of $SrVO_3$ may be further engineered. The understandings of interband transitions of $SrVO_3$ also provide good hints to search for other correlated transparent conductors.

Chapter 7

Surface polarization and edge charges

In previous chapters I have discussed the structure-dependent effects for superlattices and thin films, and in this chapter I will investigate polarization effect at the surface. The term "surface polarization" is introduced to describe the in-plane polarization existing at the surface of an insulating crystal when the in-plane surface inversion symmetry is broken. In this chapter, the surface polarization is formulated in terms of a Berry phase, with the hybrid Wannier representation providing a natural basis for study of this effect. Tight binding models are used to demonstrate how the surface polarization reveals itself via the accumulation of charges at the corners/edges for a two dimensional rectangular lattice and for GaAs.

7.1 Introduction

Electronic properties at surfaces can be quite distinct from the bulk state. One of the main reasons is that the surface lowers the crystalline symmetry. Furthermore, when the in-plane inversion or mirror symmetry is broken, there should exist an in-plane polarization at the surface, no matter surface reconstructions happen or not.

For over two decades, it has been understood that the electric polarization $\mathbf{P}$ of an insulating crystal is a bulk quantity whose electronic contribution is determined modulo $2e\mathbf{R}/\Omega$ (where $\mathbf{R}$ is a lattice vector and Ω is the unit cell volume) by the Bloch functions through a Berry-phase expression, or alternatively, in real space through the charge centers of the Wannier functions [128, 129]. It was also shown that the macroscopic surface charge of an insulating crystal is predicted by the standard bound-charge expression $\sigma^{\mathrm{surf}} = \mathbf{P} \cdot \hat{\mathbf{n}}$ (where $\hat{\mathbf{n}}$ is the surface normal) [130], as illustrated schematically in Fig. 7.1(a).

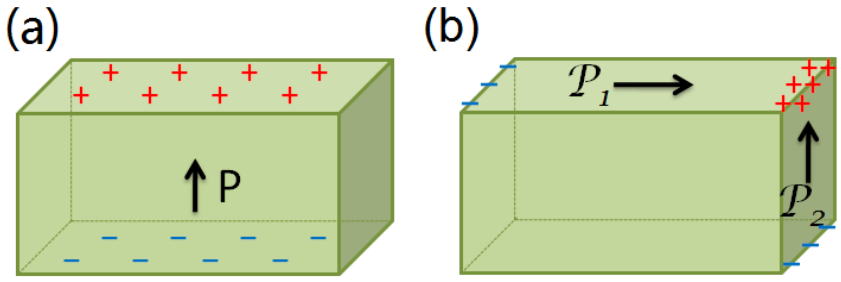

Figure 7.1: Illustration of bulk and surface polarization effects. The polarizations are denoted by black arrows, and net positive and negative bounded charged are in red and blue, respectively. (a) Bulk polarization gives rise to surface charges σ. (b) Surface polarization gives rise to edge charges λ.

Here, we introduce and analyze a related quantity, the *"surface polarization,"* defined as a 2-vector $\boldsymbol{\mathcal{P}}$ lying in the plane of an insulating surface of an insulating crystal. By analogy with the bulk 3-vector $\boldsymbol{P}$, it has the property that when two facets meet, the linear bound-charge density appearing on the shared edge is predicted to be

$$\lambda^{\text{edge}} = \boldsymbol{\mathcal{P}}_1 \cdot \hat{\mathbf{n}}_1 + \boldsymbol{\mathcal{P}}_2 \cdot \hat{\mathbf{n}}_2 \tag{7.1}$$

where $\boldsymbol{\mathcal{P}}_j$ is the surface polarization on facet j and $\hat{\mathbf{n}}_j$ is a unit vector lying in the plane of the facet and pointing toward (and normal to) the edge, as illustrated in Fig. 7.1(b).

This surface polarization $\boldsymbol{\mathcal{P}}$ is quite distinct from the dipole per unit area *normal* to the surface, which has also been called "surface polarization" by other authors [131, 132]. The latter is always present regardless of the symmetry of the surface, and manifests itself macroscopically through the surface work function. In contrast, our surface polarization $\boldsymbol{\mathcal{P}}$ lies in-plane and is nonzero only when the symmetry of the terminating surface supports a nonzero in-plane vector, as for example on the (110) surface of GaAs. It can also arise from a spontaneous symmetry-lowering surface reconstruction, as observed recently at the $Pb_{1-x}Sn_xSe$ (110) surface [133] and predicted for an ultrathin film of $SrCrO_3$ on $SrTiO_3$ substrate (001) [10]. The surface polarization will be most evident when the bulk $\boldsymbol{P}$ vanishes, as will be the case for the systems discussed below.

The purpose of this Letter is to extend the Berry-phase theory to the case of surface polarization $\boldsymbol{\mathcal{P}}$ as defined above. To do this, we introduce a formulation based on hybrid

Wannier functions (HWFs), which are Bloch-like parallel to the surface and Wannier-like in the surface-normal direction [134, 135, 136, 137]. This allows for the use of Berry-phase methods parallel to the surface while allowing a real-space identification of the surface-specific contribution in the normal direction. We illustrate the concept first for a "toy" 2D tightbinding (TB) model, demonstrating the method of calculating the surface polarization. We then consider an atomistic 3D model of an ideal (110) surface of a generic III-V zincblende semiconductor, using a TB model of GaAs to describe the electronic structure. In both cases, we confirm that the surface polarization correctly predicts corner and edge charges.

7.2 Formalism and methods

We first show how to express the surface polarization in terms of the Berry phases of HWFs for a 2D insulating sample, which we take to lie in the (x, z) plane. We take the "surface" (here really an edge) to be normal to $\hat{z}$ and introduce HWFs $|h_{lj}(k_x)\rangle$, where l indexes unit-cell layers normal to the z direction and j runs over occupied Wannier functions in a single unit cell. For the bulk, the lattice is periodic in z as well as x, and the $|h_{lj}(k_x)\rangle$ and their centers $z_{lj}^{\mathrm{bulk}}(k_x)$ can be obtained using the 1D construction procedure given in Ref. [138]. To study the surface behavior we consider a ribbon consisting of a finite number of unit cells along $\hat{z}$. We then construct and diagonalize the matrix $Z_{mn} = \langle\psi_m(k_x)|\, z\, |\psi_n(k_x)\rangle$, whose eigenvectors yield the HWFs and whose eigenvalues give the HWF centers $z_{lj}(k_x)$. In practice these are easily identified with the bulk $z_{lj}^{\mathrm{bulk}}(k_x)$ covering the range of l values that define the ribbon, with only modest shifts induced by the presence of the surface, allowing a common labeling scheme for both.

If we were interested in computing the dipole moment *normal* to the surface, we could obtain this from an analysis of the k_x-averaged z positions $\bar{z}_{lj}$ of the HWFs, where a is the lattice constant along x. However, our purpose here is different: we want to compute the polarization *parallel* to the surface. For this, we compute the Berry phase

$$\gamma_{x,lj} = \int dk_x\ \langle h_{lj}|\, i\frac{d}{dk_x}\, |h_{lj}\rangle\,. \tag{7.2}$$

of each HWF "band" (lj) as k_x runs across the 1D BZ. Doing the same for the bulk HWFs (these are independent of l) and taking the difference, we obtain a set of Berry-phase shifts $\Delta\gamma_{x,lj} \equiv \gamma_{x,lj} - \gamma_{x,j}^{\rm bulk}$ from which the electronic surface polarization can be determined via

$$\mathcal{P}_x^{\rm elec} = -\frac{ea}{\Omega\pi} \sum_{lj=\rm center}^{\rm top\ surf} \Delta\gamma_{x,lj} \tag{7.3}$$

where a factor of two has been included for spin degeneracy and Ω is the edge repeat length a in 2D. Since $\Delta\gamma_{x,lj}$ decays exponentially into the bulk, the sum will converge within a few layers of the surface, but for definiteness we sum to the center of the ribbon. If the z_{lj} values of some neighboring HWF bands overlap, the procedure needs to be generalized by grouping the HWFs into layers and using a multiband generalization to assign contributions to each layer.

The generalization to a 3D crystal with surface normal to z is straightforward. The HWFs are $|h_{lj}(k_x, k_y)\rangle$ with centers $z_{lj}(k_x, k_y)$. The surface polarization $\mathcal{P}_x^{\rm elec}$ is then obtained by computing Berry phases with respect to k_x as before, averaging over all k_y, and multiplying by the lattice constant a divided by the surface cell area Ω. The other surface polarization $\mathcal{P}_y$ is given by the same formalism but with x and y reversed.

In the models considered in this paper, the surface polarization is purely electronic, as the ions are held fixed in their bulk positions. More generally, $\mathcal{P}_x = \mathcal{P}_x^{\rm ion} + \mathcal{P}_x^{\rm elec}$ with the ionic contribution given by $\mathcal{P}_x^{\rm ion} = \Omega^{-1} \sum_{l\tau} Z_\tau \, (X_{l\tau} - X_{l\tau}^{\rm bulk})$, where Z_τ and $X_{l\tau}$ are the x position and bare charge of ion τ in cell l, and $X_\tau^{\rm bulk}$ is the corresponding bulk position of the same atom.

7.3 Two-dimensional tight-binding model

To illustrate these ideas, we start by considering a tight-binding (TB) model of the simple 2D crystal shown in Fig. 7.2(a). We assume a rectangular lattice with an aspect ratio $b/a = 0.8$. There are two atoms symmetrically located along a diagonal of the rectangular unit cell with coordinates $(\frac{1}{3}, \frac{1}{3})$ and $(\frac{2}{3}, \frac{2}{3})$, so that the bulk crystal has inversion symmetry. We consider only one s orbital per atom with onsite energy taken to be zero, and assume that each atom contributes one electron so that only the lower band

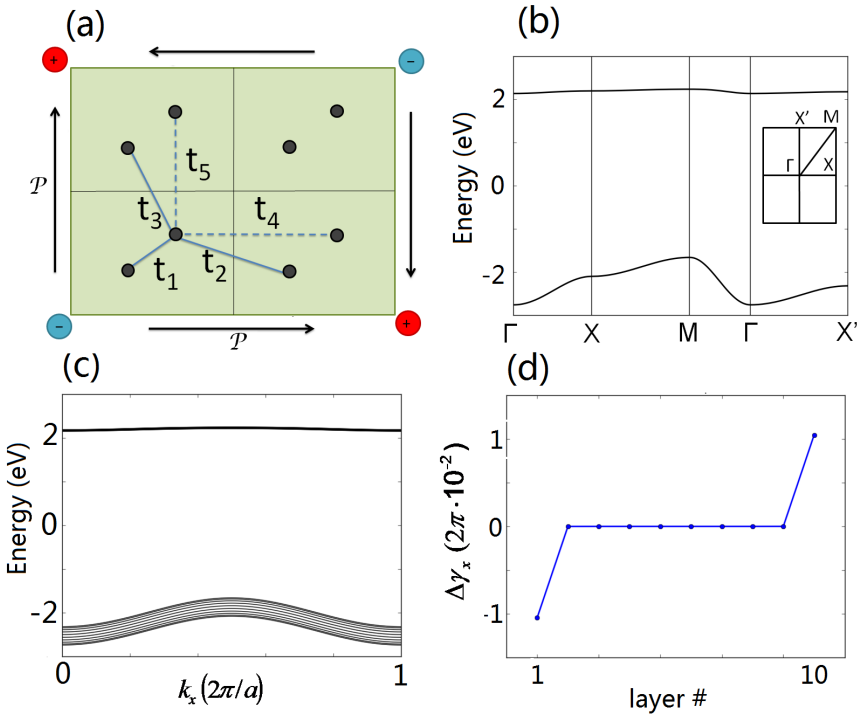

Figure 7.2: (a) Illustration of the TB model, where four unit cells are presented. The atoms are denoted by black dots. Nearest neighbor hoppings t_1, t_2 and t_3 are shown in solid blue lines. Next-nearest neighbor hoppings t_4 and t_5 are shown in dashed blue lines. $\mathcal{P}$ are shown by black arrows. The induced Q_{corner} are denoted by red (positive) and blue (negative) large dots at the corners. (b) Band structure of the TB model in the (k_x, k_z) space. The inset shows the high symmetry points in the 2D Brillouin zone, where Γ, X, M, X' refer to (0,0), $(0,\frac{1}{2})$, $(\frac{1}{2},\frac{1}{2})$ and $(\frac{1}{2},0)$, respectively. (c) Band structure along k_x for the 2D slab model that is infinite along x while 10-cell-thick in z. (d) Difference between effective x positions of each HWF and that deep in the bulk.

is (doubly) occupied. We take the nonzero hoppings to be those shown in Fig. 7.2(a) and choose their values to be $t_1 = -2.2$, $t_2 = -0.15$, and $t_3 = -0.1$, $t_4 = -0.09$ and $t_5 = -0.06$ in eV. The position operators are taken to be diagonal in the local-orbital representation so that $\langle \phi_i | z | \phi_j \rangle = z_i \delta_{ij}$.

We plot the bulk band structure of the TB Hamiltonian in Fig. 7.2(b). For the selected parameters the band gap is large compared to the band widths; in particular, the upper (unoccupied) band is quite flat. Next we compute the surface polarization of a ribbon cut from the 2D lattice, taking it to be ten unit cells thick along z and infinite along x. For the atoms in the surface layers, the hoppings to the interior atoms are the same as those described above, while the hoppings to the vacuum side are set to zero. We used an equally spaced 60-point k_x grid. At each k_x the 20×20 Hamiltonian is diagonalized, resulting in the band structure shown in Fig. 7.2(c). There are no obvious surface states, and in fact the result looks almost indistinguishable from a surface projection of the bulk band structure. The eigenfunctions $|\psi_n(k_x)\rangle$ are expressed in the tight-binding basis as $|\psi_n(k_x)\rangle = \sum_j c_{nj}(k_x) \, |\chi_j(k_x)\rangle$, where the $|\chi_j(k_x)\rangle$ are the Bloch basis function formed as a Fourier sum at wavevector k_x of atomic orbitals $|\phi_i\rangle$. From the ten occupied bands we construct the 10×10 position matrix $Z_{mn} = \langle \psi_m(k_x) | z | \psi_n(k_x) \rangle = \sum_j z_j c^*_{mj}(k_x) c_{nj}(k_x)$. Diagonalizing this matrix, we get ten eigenvalues $z_l(k_x)$ that can each be clearly associated with a particular unit cell layer, and ten eigenfunctions that are the HWFs. We label the HWF $|h_l(k_x)\rangle$, where l is the layer index running from the bottom to the top of the ribbon.

Next we calculate $\gamma_{x,l}$, the Berry phase along k_x, for each l using Eq. (7.2). Deep in the interior these Berry phases become equal to π within numerical precision, while the Berry phases near the edge are slightly shifted away from π, leading to a nonzero surface polarization as shown in Fig. 7.2(d).

The value of the surface polarization obtained from Eq. (7.3) is $\mathcal{P}_x = \pm 2.1 \times 10^{-4} \, e$ for the top and bottom surfaces respectively. Similarly we can compute the surface polarizations for the left/right surfaces using a ribbon ten cells wide in x and infinite along z. We obtain $\mathcal{P}_z = \pm 4.7 \times 10^{-4} \, e$ along the left and right edges respectively. At the corners, the surface polarizations are directed head-to-head or tail-to-tail, as shown

in Fig. 7.2(a).

We have investigated the dependence of the surface polarizations on the model parameters, finding that its magnitude scales roughly as a power of the ratio of the valence band width over the band gap. We also find that the surface polarization contributions decay into the interior with a decay length that increases as this ratio increases. The hopping parameters we chose give a decay length short enough to achieve essentially zero ($< 10^{-7}$) polarization in the center of the 10-layer ribbon.

Given the values of the surface polarizations in the 2D model, we predict that the charge accumulation at the corner of a finite sample should equal the sum of the two adjacent surface polarizations, here $|\mathcal{P}_x| + |\mathcal{P}_z| = 6.8 \times 10^{-4}\, e$. To test this, we directly calculate the corner charge in a finite 2D sample, specifically a 10×10 supercell, large enough to ensure neutrality in the central region and in the middle of the edges of the sample. The corner charge is obtained by summing up the on-site charge differences, relative to the bulk, for atoms in the quadrant containing the corner. We find $Q_{\text{corner}} = 6.8 \times 10^{-4}\, e$ for the top left and bottom right corners, and $-6.8 \times 10^{-4}\, e$ for the other two corners, in agreement with our prediction from the computed surface polarizations.

7.4 GaAs with (110) facets

We now consider a TB model of a generic III-V zincblende semiconductor, with GaAs as the prototypical example. The crystal structure is characterized by Ga-As zigzag chains running along $\langle 110 \rangle$. Although the crystal structure does not have inversion symmetry, the tetrahedral symmetry forbids a nonzero spontaneous polarization. We use tight-binding parameters from Ref. [139], in which is shown the bulk bandstructure and density of states. The unit cell contains two Ga and two As atoms, each with four sp^3 hybridized orbitals and four electrons, as shown in Fig. 7.3(a). The position matrix is assumed to be diagonal and atom-centered in the basis of tight-binding orbitals.[140]

To describe the (110) surface, we construct a slab geometry as shown in Fig. 7.3(a), and we henceforth label the Cartesian directions as shown there. That is, the surface, which is normal to $\hat{z}$, has zigzag chains running along $\hat{y}$. Since the two atoms making

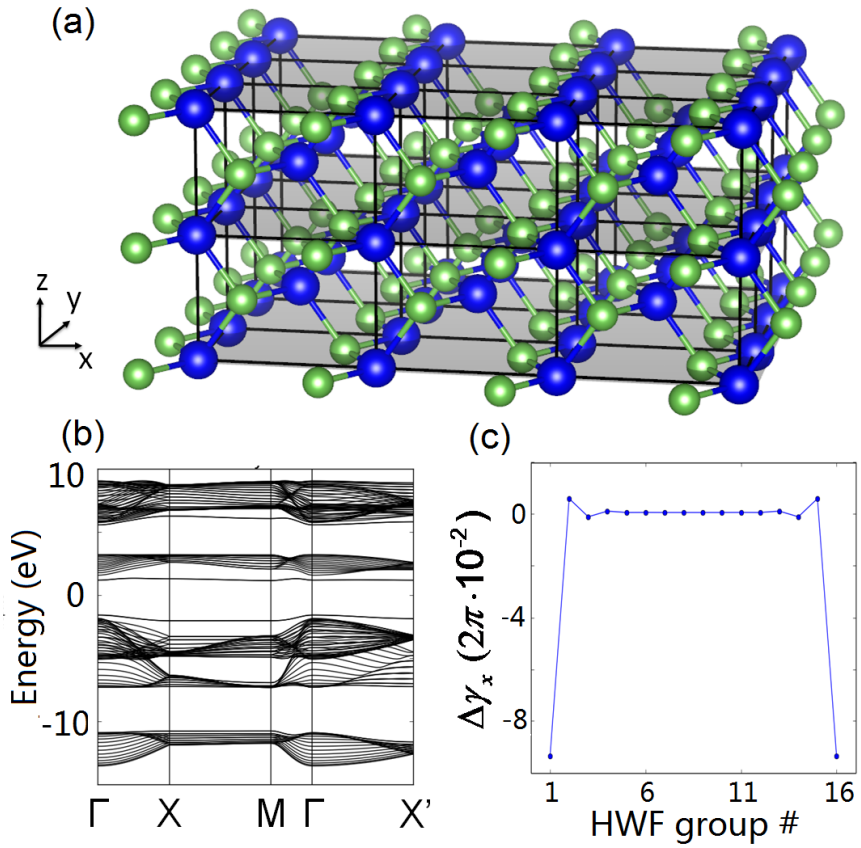

Figure 7.3: (a) Illustration of the GaAs slab studied in the TB model, where the blue and green balls represent Ga and As atoms, respectively. The grey shaded planes denote the (110) family planes. (b) Electronic band structure of the GaAs slab in the 2D Brillouin zone, with the thickness of 8 cells z. (c) Difference between the γ_x of each group of HWFs and that deep in the bulk.

up these chains are inequivalent, we expect a surface polarization in the $\hat{x}$ direction. We take the slab to be eight unit cells thick; for the atoms in the surface layer, the hoppings to the atoms inside the slab are the same as in the bulk, while the hoppings to the vacuum side are set to zero. At each (k_x,k_y) of the 100×100 k grid in the surface BZ, the 128×128 Hamiltonian is diagonalized, and we obtain the band structure for the slab, shown in Fig. 7.3(b). Surface states are evident as isolated bands.

Next, we diagonalize the 64×64 position matrices $Z(k_x, k_y)$ constructed from the eigenstates of the occupied bands. The eigenvalues, which are the z coordinates of the HWF centers, can be clearly divided into groups, each consisting of four HWFs j representing the four Ga-As bonds around an As atom, each group being associated with one of the 16 atomic layers l. In this case, it is more useful to calculate the Berry phase of each group of HWFs rather than of each single HWF [130].

As expected, the Berry phase in the $\hat{y}$ direction along the zigzag chain is found to be zero, but in the $\hat{x}$ direction it is nonzero for the HWF groups near the top and bottom surfaces of the slab. Thus, we confirm that there is a nonzero surface polarization $\mathcal{P}_x$. We plot the difference between the Berry phase γ_x of each group of HWFs and that for the bulk in Fig. 7.3(c). By summing up the contributions from each group of HWFs from the center of the bulk to one surface, the total surface polarization is found to be 0.178 e/L. Here $L = a/\sqrt{2}$ is the repeat length of the zigzag chain, i.e., the surface cell dimension along $\hat{y}$, where a is the surface lattice constant along $\hat{x}$. Subdividing the dominant surface-group contribution further, we find that the surface polarization comes mainly from the surface-most HWF, corresponding to a shift of the center of the dangling bond on the surface As atom.

The surface polarization on the {110} surfaces predicts an accumulated line charge for the common edge of two such surfaces. In order to demonstrate this effect, we consider a hexagonal wire of GaAs that is infinite along [111], with a periodicity corresponding to three of the GaAs buckled (111) layers. In this case, the six side surfaces of the wire are all {110} planes: $(1\bar{1}0)$, $(10\bar{1})$, $(01\bar{1})$, $(\bar{1}10)$, $(\bar{1}01)$, and $(0\bar{1}1)$. As shown in Fig. 7.4(a), on each side facet the surface polarization is perpendicular to

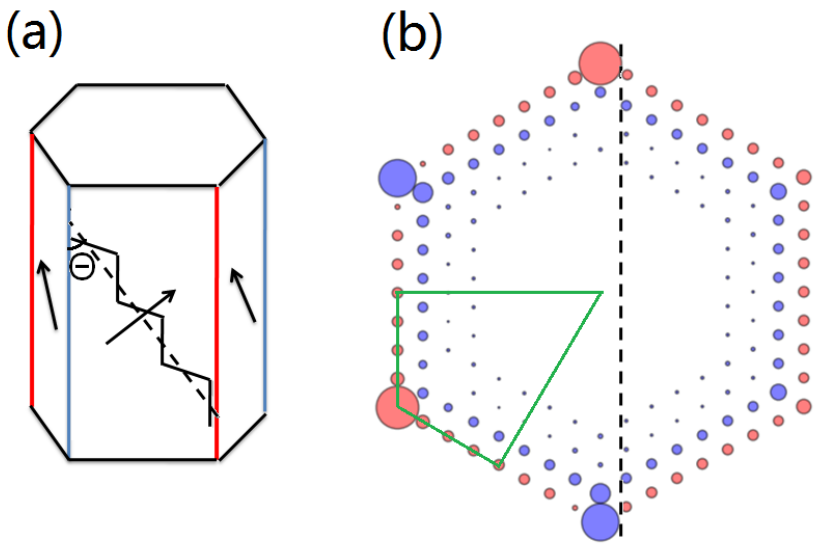

Figure 7.4: (a) Overhead view of the hexagonal GaAs nanowire. The dashed black line, which meets the edges along [111] at an angle of $\theta = 35.26°$, shows the direction along which the zigzag surface chains run. The relevant surface polarizations at the side surfaces are denoted by black arrows. The blue and red vertical edges mean net negative and positive edge charge distributions, respectively. (b) On-site charge distribution summed over the trilayer. Red and blue dots represent positive and negative net charges, respectively. The sizes of dots indicate the magnitudes of the on-site net charge. the left and right regions to the dashed vertical line show the total and symmetric part of onsite charges, respectively.

the zigzag chains, forming a pattern of $\boldsymbol{\mathcal{P}}$ vectors shown as black arrows. The surface polarizations for each neighboring pair of side facets have a common component along [111], but are head-to-head or tail-to-tail for the component normal to [111], leading to alternating positive and negative line charges for the six edges as shown. According to Eq. (7.1), we expect the line charge per three-layer vertical period to be $Q_{3L} = 2\mathcal{P}\cos\theta \cdot 3L\cos\theta = 0.71e$, where the $3L\cos\theta$ factor is the vertical period.

For comparison, we directly calculate the edge charges per trilayer period in a nanowire with a radius of 8 atoms. We sum up the site populations within the TB model with a 60-point k grid along [111]. The onsite charge is the difference from the bulk value. The computed onsite charges are shown in the left half of Fig. 7.4(b), while the right half shows the corresponding results after averaging with a 60°-rotated version of itself. The surface charges decay rapidly into the bulk, leading to a neutral bulk

state inside the nanowire. Also, a surface dipole density normal to the surface is clearly visible, especially in the orientationally averaged results. However, we are interested in the accumulation at the edges, which is obviously present in the unaveraged results in the left half of the figure. The edge charge is calculated by summing up the onsite charges in the wedge-shaped region illustrated in Fig. 7.4(b), using a weight of 1/2 for atoms located on its radial edges. The total edge charge per trilayer is found to be $\pm 0.71e$, in agreement with the value predicted using the previously calculated surface polarization.

7.5 Discussion

We emphasize that this numerical value is not intended to be realistic for GaAs. A more accurate estimate would require the use of an improved tight-binding model and treatment of surface relaxations and dielectric screening effects, or better, direct first-principles calculations. Our purpose here has been to show that the surface polarization as defined here correctly predicts edge charges. We note that an analysis based on maximally localized Wannier functions [141] is also possible. However, we believe our HWF-based approach is more natural, as the Wannier transformation is only done in the needed direction and no iterative construction is required.

We stress that the concept of surface polarization $\boldsymbol{\mathcal{P}}$ is quite general, occurring whenever the surface symmetry is low enough. In some cases this can arise from a spontaneous symmetry-lowering surface relaxation or reconstruction, allowing "surface ferroelectricity" if it is switchable. In other cases, as for GaAs (110), the ideal surface space group already has low enough symmetry to allow a nonzero $\boldsymbol{\mathcal{P}}$. This will occur quite generally for low-angle vicinal surfaces. The concept also applies to planar defects such as domain walls, stacking faults, and twin boundaries, and to heterointerfaces; if $\boldsymbol{\mathcal{P}}$ is present within this plane, it may induce a line charge where the plane intersects the surface. Such edge and line charges are potentially observable using electric force microscopy [142] , electron holography [143], or other experimental methods. Finally we note that the concept of surface polarization may become more subtle in the presence of orbital magnetization, which we have omitted from our considerations here.

7.6 Summary

In summary, we have formulated the concept of surface polarization, i.e., the dipole moment per unit area *parallel* to the surface, which can exist whenever the surface symmetry is low enough. Using TB models we have computed the surface polarizations for a 2D toy model and a generic III-V zincblende semiconductor, and shown that the predicted corner or edge charges are in good agreement with direct calculations. We point out that surface and interface polarizations can be responsible for observable effects, and perhaps even desirable functionality, in a broad range of insulating materials systems.

Chapter 8

Conclusion and Outlook

In this thesis we have discussed several structure-dependent electronic properties of oxides, including the spin-phonon coupling effect for 1:1 $SrMnO_3/LaMnO_3$ superlattice, ground state structure determination, the metal-insulator transition due to the nonpolar to polar structural transition for 1:1 $SrCrO_3/SrTiO_3$ superlattice, the optical interband transitions for tetragonal $SrVO_3$ thin film, and the surface polarization of the crystal whose surface in-plane mirror symmetry is broken.

These chapters have shown the importance of the structure of a crystal. It is usually related to many functional properties, and thus means of altering crystal structures may be considered tuning parameters to search for desirable properties. Currently, doping, temperature and pressure are still important techniques to control the structure of bulk materials, leading to changes of electronic states. With the development of epitaxy synthesis methods, heterostructures such as thin films and superlattices are also accessible, yielding many possibilities for a number of innovations. The two-dimensional confinement of superlattice and thin film structures lead to electronic structures distinct from the bulk state. Epitaxial strain that commonly exists for heterostructures has also become a very important and useful tuning parameter for inducing structural transitions, as studied in depth in the thesis, and also many previous references.

To further discover and innovate novel properties and functionalities, there are several points that are worth investigating in my opinion. First, superlattice of different constituent combinations. The large number of combinations of constituents give all kinds of possibilities to turn on novel properties in superlattices. In this thesis we have discussed three types of superlattices 1. $SrMnO_3/LaMnO_3$, a typical Mott insulating/Mott insulating and AFM/AFM superlattice, with the same B-site atom,

while different A-site atoms with different chemical valences that may lead to electron transfer. 2. $PbTiO_3/SrTiO_3$, a band insulating/band insulating, and ferroelectric/dielectric superlattice, with different A-site atoms but the same chemical valence. 3. $SrCrO_3/SrTiO_3$, a metallic/dielectric superlattice. Beyond these, there could be many other combinations such as metallic/Mott insulating superlattice, metallic/metallic superlattice with different magnetic ordering etc.

Second, different orientations of superlattices. Synthesis of superlattices in (111) orientation is a challenge. For (001) oriented perovskite superlattice, each atomic layer, both AO and BO_2 are usually charge neutral, or with alternating ± 1 valence. For (111) oriented superlattice, the atomic layers are either B or AO_3, the chemical valence can be alternating ± 3 or ± 4. These charged planes lead to problems in layered synthesis. Nonetheless, recent experimental successes indicate that this will soon become an active topic of investigation. A simple change of epitaxy orientation changes a lot. The most important aspect is the symmetry of the lattice. For example, for the cubic perovskite along [001], the d orbitals split into doubly degenerate e_g and triply degenerate t_{2g} due to the octahedral crystal field. For perovskites grown along [111], the most robust symmetry is a three fold rotational symmetry. In this case, the t_{2g} orbitals further split into one a_{1g} orbital and doubly degenerate e'_g orbitals, while e_g are still degenerate. Thus orbital orders or charge orders different from the [001] oriented structures may arise. More specifically, 1:1 perovskite superlattice in (111) orientation can be viewed as double perovskite in (111). 2:2 perovskite superlattice in (111) forms a buckled honeycomb lattice, for which topological properties are usually easy to establish. 3:3 superlattice then can form Kagome lattice. Currently most studies focus on the topological properties or the interplay of strong correlation and spin-orbit coupling effects that lead to the rich phase diagrams in the (111) oriented superlattices. The dimension, structural related properties have also been investigated in theory, but there are still many subjects to be studied.

Third, surface. Surface is an interface with vacuum, or air. The symmetry is lowered at the surface, possibly leading to the surface polarization as discussed in Chapter 7. The missing apical atoms at the surface may lead to the reconstruction of structure

and result in different electronic properties. Also, for the similar reasons of the second point, surfaces of different facets can have various properties. Recently many studies on the (111) surface of perovsites found 2D electron gas and other interesting results.

Last but not least, when using first-principles calculation for novel materials designing and searching, the ground state structure still leave problems. Even if we have developed the stacking method for the ground state structure determination for (001) perovksite superlattices, improvements are expected to generalize it to a broader range of systems. For example, how should we determine the ground state structures for superlattices oriented along directions other than [001]? Whether the stacking method works is a question. Moreover, even if stacking method works, whether we should have low energy structures for bulk materials with epitaxial strain other than (001) orientation will be another question.

Overall, transition metal oxide is not a new paradigm, but during the course of research we have been finding new tuning parameters to engineer the properties of TMOs. Even for just the subgroup of perovskites, there are many unsolved problems to be investigated and novel materials/functionalities to be discovered. Meanwhile, first principles calculations can give the ground state electronic structure of existing and hypothetical materials, provide valuable information to understand new phenomena and help discover novel functionalities. I hope this thesis has presented valuable results for the specific topics and will generate a lot of interests for further studies.

References

[1] S.-W. Cheong, "Transition metal oxides: The exciting world of orbitals," *Nature Materials*, vol. 6, pp. 927–928, DEC 2007.

[2] J. Ngai, F. Walker, and C. Ahn, "Correlated Oxide Physics and Electronics," *Annual Review of Materials Research*, vol. 44, no. 1, pp. 1–17, 2014.

[3] E. Dagotto, T. Hotta, and A. Moreo, "Colossal magnetoresistant materials: the key role of phase separation," *Physics Reports*, vol. 344, no. 13, pp. 1 – 153, 2001.

[4] M. Imada, A. Fujimori, and Y. Tokura, "Metal-insulator transitions," *Rev. Mod. Phys.*, vol. 70, pp. 1039–1263, Oct 1998.

[5] H. Y. Hwang, S.-W. Cheong, P. G. Radaelli, M. Marezio, and B. Batlogg, "Lattice Effects on the Magnetoresistance in Doped $LaMnO_3$," *Phys. Rev. Lett.*, vol. 75, pp. 914–917, Jul 1995.

[6] G. J. Snyder, R. Hiskes, S. DiCarolis, M. R. Beasley, and T. H. Geballe, "Intrinsic electrical transport and magnetic properties of $La_{0.67}Ca_{0.33}MnO_3$ and $La_{0.67}Sr_{0.33}MnO_3$ MOCVD thin films and bulk material," *Phys. Rev. B*, vol. 53, pp. 14434–14444, Jun 1996.

[7] A. Cho and J. Arthur, "Molecular beam epitaxy," *Progress in Solid State Chemistry*, vol. 10, Part 3, no. 0, pp. 157 – 191, 1975.

[8] J. H. Lee, L. Fang, E. Vlahos, X. Ke, Y. W. Jung, L. F. Kourkoutis, J.-W. Kim, P. J. Ryan, T. Heeg, M. Roeckerath, V. Goian, M. Bernhagen, R. Uecker, P. C. Hammel, K. M. Rabe, S. Kamba, J. Schubert, J. W. Freeland, D. A. Muller, C. J. Fennie, P. Schiffer, V. Gopalan, E. Johnston-Halperin, and D. G. Schlom, "A strong ferroelectric ferromagnet created by means of spin-lattice coupling," *Nature*, vol. 466, no. 7309, pp. 954–958, 2010.

[9] J. H. Lee and K. M. Rabe, "Epitaxial-strain-induced multiferroicity in $SrMnO_3$ from first principles," *Phys. Rev. Lett.*, vol. 104, p. 207204, May 2010.

[10] K. Gupta, P. Mahadevan, P. Mavropoulos, and M. Ležaić, "Orbital-Ordering-Induced Ferroelectricity in $SrCrO_3$," *Phys. Rev. Lett.*, vol. 111, p. 077601, Aug 2013.

[11] A. Ohtomo and H. Y. Hwang, "A high-mobility electron gas at the $LaAlO_3/SrTiO_3$ heterointerface.," *Nature*, vol. 427, no. 6973, pp. 423 – 426, 2004.

[12] E. J. Monkman, C. Adamo, J. A. Mundy, D. E. Shai, J. W. Harter, D. Shen, B. Burganov, D. A. Muller, D. G. Schlom, and K. M. Shen, "Quantum many-body interactions in digital oxide superlattices," *Nat. Mater.*, vol. 11, pp. 855–859, OCT 2012.

[13] C. J. Fennie and K. M. Rabe, "Magnetic and electric phase control in epitaxial eutio$_3$ from first principles," *Phys. Rev. Lett.*, vol. 97, p. 267602, Dec 2006.

[14] E. Bousquet, M. Dawber, N. Stucki, C. Lichtensteiger, P. Hermet, S. Gariglio, J.-M. Triscone, and P. Ghosez, "Improper ferroelectricity in perovskite oxide artificial superlattices," *Nature*, vol. 452, no. 7188, pp. 732–736, 2008.

[15] Y. Zhou and K. M. Rabe, "Epitaxial strain effects on magnetic ordering and spin-phonon couplings in the $(SrMnO_3)_1/(LaMnO_3)_1$ superlattice from first principles," *Phys. Rev. B*, vol. 88, p. 094416, Sep 2013.

[16] Y. Zhou and K. M. Rabe, "Determination of ground-state and low-energy structures of perovskite superlattices from first principles," *Phys. Rev. B*, vol. 89, p. 214108, Jun 2014.

[17] Y. Zhou and K. M. Rabe, "Coupled Nonpolar-Polar Metal-Insulator Transition in 1:1 $SrCrO_3/SrTiO_3$ Superlattices: A First-Principles Study," *Phys. Rev. Lett.*, vol. 115, p. 106401, Aug 2015.

[18] Y. Zhou, K. M. Rabe, and D. Vanderbilt, "Surface polarization and edge charges," *Phys. Rev. B*, vol. 92, p. 041102, Jul 2015.

[19] P. Hohenberg and W. Kohn, "Inhomogeneous electron gas," *Phys. Rev.*, vol. 136, pp. B864–B871, Nov 1964.

[20] W. Kohn and L. Sham, "Self-consistent equations including exchange and correlation effects," *Phys. Rev.*, vol. 140, pp. A1133–A1138, Nov 1965.

[21] L. Hedin and B. I. Lundqvist, "Explicit local exchange-correlation potentials," *Journal of Physics C: Solid State Physics*, vol. 4, no. 14, p. 2064, 1971.

[22] J. Perdew and A. Zunger, "Self-interaction correction to density-functional approximations for many-electron systems," *Phys. Rev. B*, vol. 23, pp. 5048–5079, May 1981.

[23] D. Langreth and J. Perdew, "Exchange-correlation energy of a metallic surface: Wave-vector analysis," *Phys. Rev. B*, vol. 15, pp. 2884–2901, Mar 1977.

[24] M. Payne, M. Teter, D. Allan, T. Arias, and J. Joannopoulos, "Iterative minimization techniques for *ab initio* total-energy calculations: molecular dynamics and conjugate gradients," *Rev. Mod. Phys.*, vol. 64, pp. 1045–1097, Oct 1992.

[25] J. Perdew, J. Chevary, S. Vosko, K. Jackson, M. Pederson, D. Singh, and C. Fiolhais, "Atoms, molecules, solids, and surfaces: Applications of the generalized gradient approximation for exchange and correlation," *Phys. Rev. B*, vol. 46, pp. 6671–6687, Sep 1992.

[26] G. Kresse and J. Hafner, "*Ab initio* molecular dynamics for liquid metals," *Phys. Rev. B*, vol. 47, pp. 558–561, Jan 1993.

[27] G. Kresse and J. Furthmüller, "Efficient iterative schemes for *ab initio* total-energy calculations using a plane-wave basis set," *Phys. Rev. B*, vol. 54, pp. 11169–11186, Oct 1996.

[28] D. R. Hamann, M. Schlüter, and C. Chiang, "Norm-conserving pseudopotentials," *Phys. Rev. Lett.*, vol. 43, pp. 1494–1497, Nov 1979.

[29] D. Vanderbilt, "Soft self-consistent pseudopotentials in a generalized eigenvalue formalism," *Phys. Rev. B*, vol. 41, pp. 7892–7895, Apr 1990.

[30] P. E. Blöchl, "Projector augmented-wave method," *Phys. Rev. B*, vol. 50, pp. 17953–17979, Dec 1994.

[31] G. Kresse and D. Joubert, "From ultrasoft pseudopotentials to the projector augmented-wave method," *Phys. Rev. B*, vol. 59, pp. 1758–1775, Jan 1999.

[32] V. Anisimov, J. Zaanen, and O. Andersen, "Band theory and mott insulators: Hubbard U instead of stoner I," *Phys. Rev. B*, vol. 44, pp. 943–954, Jul 1991.

[33] A. Liechtenstein, V. Anisimov, and J. Zaanen, "Density-functional theory and strong interactions: Orbital ordering in mott-hubbard insulators," *Phys. Rev. B*, vol. 52, pp. R5467–R5470, Aug 1995.

[34] S. L. Dudarev, G. A. Botton, S. Y. Savrasov, C. J. Humphreys, and A. P. Sutton, "Electron-energy-loss spectra and the structural stability of nickel oxide: an LSDA+U study," *Phys. Rev. B*, vol. 57, pp. 1505–1509, Jan 1998.

[35] P. Giannozzi, S. de Gironcoli, P. Pavone, and S. Baroni, "*Ab initio* calculation of phonon dispersions in semiconductors," *Phys. Rev. B*, vol. 43, pp. 7231–7242, Mar 1991.

[36] S. Baroni, S. de Gironcoli, A. Dal Corso, and P. Giannozzi, "Phonons and related crystal properties from density-functional perturbation theory," *Rev. Mod. Phys.*, vol. 73, pp. 515–562, Jul 2001.

[37] R. Resta and D. Vanderbilt, *Theory of Polarization: A Modern Approach*, vol. 105 of *Topics in Applied Physics*. Springer Berlin Heidelberg, 2007.

[38] R. D. King-Smith and D. Vanderbilt, "Theory of polarization of crystalline solids," *Phys. Rev. B*, vol. 47, pp. 1651–1654, Jan 1993.

[39] T. Katsufuji and H. Takagi, "Coupling between magnetism and dielectric properties in quantum paraelectric $EuTiO_3$," *Phys. Rev. B*, vol. 64, p. 054415, Jul 2001.

[40] J. Laverdière, S. Jandl, A. A. Mukhin, V. Y. Ivanov, V. G. Ivanov, and M. N. Iliev, "Spin-phonon coupling in orthorhombic $R\mathrm{MnO_3}$ (R = Pr, Nd, Sm, Eu, Gd, Tb, Dy, Ho, Y): A raman study," *Phys. Rev. B*, vol. 73, p. 214301, Jun 2006.

[41] C. J. Fennie and K. M. Rabe, "Magnetically induced phonon anisotropy in zncr2o4 from first principles," *Phys. Rev. Lett.*, vol. 96, p. 205505, May 2006.

[42] "Large spin-phonon coupling and magnetically induced phonon anisotropy in SrMO$_3$ perovskites (M=V,Cr,Mn,Fe,Co),,"

[43] J. H. Lee and K. M. Rabe, "Epitaxial-strain-induced multiferroicity in $SrMnO_3$ from first principles," *Phys. Rev. Lett.*, vol. 104, p. 207204, May 2010.

[44] J. H. Lee, K. T. Delaney, E. Bousquet, N. A. Spaldin, and K. M. Rabe, "Strong coupling of Jahn-Teller distortion to oxygen-octahedron rotation and functional properties in epitaxially strained orthorhombic $LaMnO_3$," *Phys. Rev. B*, vol. 88, p. 174426, Nov 2013.

[45] A. Kumar, C. J. Fennie, and K. M. Rabe, "Spin-lattice coupling and phonon dispersion of $CdCr_2O_4$ from first principles," *Phys. Rev. B*, vol. 86, p. 184429, Nov 2012.

[46] S. Bhattacharjee, O. Eriksson, and B. Sanyal, "First principles calculations of magnetism, dielectric properties and spinphonon coupling in double perovskite Bi_2CoMnO_6," *Journal of Physics: Condensed Matter*, vol. 24, no. 29, p. 295901, 2012.

[47] J. Hong, A. Stroppa, J. Íñiguez, S. Picozzi, and D. Vanderbilt, "Spin-phonon coupling effects in transition-metal perovskites: A DFT + U and hybrid-functional study," *Phys. Rev. B*, vol. 85, p. 054417, Feb 2012.

[48] D. G. Schlom, L.-Q. Chen, C.-B. Eom, K. M. Rabe, S. K. Streiffer, and J.-M. Triscone, "Strain tuning of ferroelectric thin films," *Ann. Rev. Mater. Res.*, vol. 37, pp. 589–626, 2007.

[49] J. M. Rondinelli and N. A. Spaldin, "Structure and properties of functional oxide thin films: Insights from electronic-structure calculations," *Advanced Materials*, vol. 23, no. 30, pp. 3363–3381, 2011.

[50] H. Wang, L. He, and X. Wu, "Interface enhancement of spin-polar phonon coupling in perovskite multiferroic superlattices," *EPL (Europhysics Letters)*, vol. 100, no. 1, p. 17005, 2012.

[51] M. Izumi, T. Manako, Y. Konishi, M. Kawasaki, and Y. Tokura, "$La_{1-x}Sr_xMnO_3$ superlattices composed of ferromagnetic $x = 0.4$ and antiferromagnetic $x = 0.55$ layers," *Phys. Rev. B*, vol. 61, pp. 12187–12195, May 2000.

[52] H. Yamada, M. Kawasaki, T. Lottermoser, T. Arima, and Y. Tokura, "$LaMnO_3/SrMnO_3$ interfaces with coupled charge-spin-orbital modulation," *Applied Physics Letters*, vol. 89, no. 5, p. 052506, 2006.

[53] A. Bhattacharya, S. J. May, S. G. E. te Velthuis, M. Warusawithana, X. Zhai, B. Jiang, J.-M. Zuo, M. R. Fitzsimmons, S. D. Bader, and J. N. Eckstein, "Metal-insulator transition and its relation to magnetic structure in $(LaMnO_3)_{2n}/(SrMnO_3)_n$ superlattices," *Phys. Rev. Lett.*, vol. 100, p. 257203, Jun 2008.

[54] C. Lin and A. J. Millis, "Theory of manganite superlattices," *Phys. Rev. B*, vol. 78, p. 184405, Nov 2008.

[55] T. S. Santos, S. J. May, J. L. Robertson, and A. Bhattacharya, "Tuning between the metallic antiferromagnetic and ferromagnetic phases of $La_{1-x}Sr_xMnO_3$ near $x = 0.5$ by digital synthesis," *Phys. Rev. B*, vol. 80, p. 155114, Oct 2009.

[56] T. S. Santos, B. J. Kirby, S. Kumar, S. J. May, J. A. Borchers, B. B. Maranville, J. Zarestky, S. G. E. te Velthuis, J. van den Brink, and A. Bhattacharya, "Delta doping of ferromagnetism in antiferromagnetic manganite superlattices," *Phys. Rev. Lett.*, vol. 107, p. 167202, Oct 2011.

[57] C. Adamo, X. Ke, P. Schiffer, A. Soukiassian, M. Warusawithana, L. Maritato, and D. G. Schlom, "Electrical and magnetic properties of $(SrMnO_3)_n/(LaMnO_3)_{2n}$ superlattices," *Applied Physics Letters*, vol. 92, no. 11, p. 112508, 2008.

[58] B. R. K. Nanda and S. Satpathy, "Effects of strain on orbital ordering and magnetism at perovskite oxide interfaces: $LaMnO_3/SrMnO_3$," *Phys. Rev. B*, vol. 78, p. 054427, Aug 2008.

[59] B. R. K. Nanda and S. Satpathy, "Electronic and magnetic structure of the $(LaMnO_3)_{2n}/(SrMnO_3)_n$ superlattices," *Phys. Rev. B*, vol. 79, p. 054428, Feb 2009.

[60] D. D. Belyea, T. S. Santos, and C. W. Miller, "Magnetocaloric effect in epitaxial $La_{0.56}Sr_{0.44}MnO_3$ alloy and digital heterostructures," *Journal of Applied Physics*, vol. 111, no. 7, p. 07A935, 2012.

[61] C. Loschen, J. Carrasco, K. M. Neyman, and F. Illas, "First-principles LDA + U and GGA + U study of cerium oxides: Dependence on the effective u parameter," *Phys. Rev. B*, vol. 75, p. 035115, Jan 2007.

[62] J. P. Perdew, K. Burke, and M. Ernzerhof, "Generalized gradient approximation made simple," *Phys. Rev. Lett.*, vol. 77, pp. 3865–3868, Oct 1996.

[63] A. M. Glazer, "The classification of tilted octahedra in perovskites," *Acta Crystallographica Section B*, vol. 28, pp. 3384–3392, Nov 1972.

[64] J. M. Rondinelli and C. J. Fennie, "Ferroelectricity: Octahedral rotation-induced ferroelectricity in cation ordered perovskites," *Advanced Materials*, vol. 24, no. 15, pp. 1918–1918, 2012.

[65] A. T. Mulder, N. A. Benedek, J. M. Rondinelli, and C. J. Fennie *arXiv*, vol. 1205.5526v2, 2012.

[66] N. A. Benedek, A. T. Mulder, and C. J. Fennie, "Polar octahedral rotations: A path to new multifunctional materials," *Journal of Solid State Chemistry*, vol. 195, no. 0, pp. 11 – 20, 2012.

[67] J. B. Goodenough, *Magnetism and the Chemical Bond*. New York, Interscience Publishers, 1963.

[68] Y. Zhou and K. M. Rabe *unpublished*.

[69] J. C. Jiang, X. Q. Pan, W. Tian, C. D. Theis, and D. G. Schlom, "Abrupt $PbTiO_3/SrTiO_3$ superlattices grown by reactive molecular beam epitaxy," *Appl. Phys. Lett.*, vol. 74, no. 19, 1999.

[70] D. Schlom, J. Haeni, J. Lettieri, C. Theis, W. Tian, J. Jiang, and X. Pan, "Oxide nano-engineering using {MBE}," *Mater. Sci. Eng. B*, vol. 87, no. 3, pp. 282 – 291, 2001.

[71] D. P. Norton, "Synthesis and properties of epitaxial electronic oxide thin-film materials," *Mater. Sci. Eng. R*, vol. 43, no. 56, pp. 139 – 247, 2004.

[72] J. B. Neaton and K. M. Rabe, "Theory of polarization enhancement in epitaxial $BaTiO_3/SrTiO_3$ superlattices," *Appl. Phys. Lett.*, vol. 82, no. 10, 2003.

[73] A. Ohtomo and H. Y. Hwang, "A high-mobility electron gas at the $LaAlO_3/SrTiO_3$ heterointerface," *Nature*, vol. 427, pp. 423–426, 2004.

[74] http://www.whitehouse.gov/mgi.

[75] S. M. Woodley and R. Catlow, "Crystal structure prediction from first principles," *Nat. Mater.*, vol. 7, pp. 937–946, DEC 2008.

[76] D. A. Coley, *An Introduction to Genetic Algorithms for Scientists and Engineers*. World Scientific, 1999.

[77] T. S. Bush, C. R. A. Catlow, and P. D. Battle, "Evolutionary programming techniques for predicting inorganic crystal structures," *J. Mater. Chem.*, vol. 5, pp. 1269–1272, 1995.

[78] D. C. Lonie and E. Zurek, "Xtalopt: An open-source evolutionary algorithm for crystal structure prediction," *Comput. Phys. Commun.*, vol. 182, no. 2, pp. 372 – 387, 2011.

[79] C. J. Pickard and R. J. Needs, "Ab initio random structure searching," *Journal of Physics: Condensed Matter*, vol. 23, no. 5, p. 053201, 2011.

[80] C. C. Fischer, K. J. Tibbetts, D. Morgan, and G. Ceder, "Predicting crystal structure by merging data mining with quantum mechanics," *Nat. Mater.*, vol. 5, pp. 641–646, AUG 2006.

[81] B. Meredig and C. Wolverton, "A hybrid computational-experimental approach for automated crystal structure solution," *Nat. Mater.*, vol. 12, pp. 123–127, FEB 2013.

[82] A. Van der Ven, M. K. Aydinol, G. Ceder, G. Kresse, and J. Hafner, "First-principles investigation of phase stability in $LixCoO_2$," *Phys. Rev. B*, vol. 58, pp. 2975–2987, Aug 1998.

[83] A. Predith, G. Ceder, C. Wolverton, K. Persson, and T. Mueller, "Ab initio," *Phys. Rev. B*, vol. 77, p. 144104, Apr 2008.

[84] K. M. Rabe, C. H. Ahn, and J. M. Triscone, *Physics of Ferroelectrics*. Springer, 2007.

[85] O. Diéguez, O. E. González-Vázquez, J. C. Wojdeł, and J. Íñiguez, "First-principles predictions of low-energy phases of multiferroic $bifeo_3$," *Phys. Rev. B*, vol. 83, p. 094105, Mar 2011.

[86] E. Bousquet, *Thesis of PhD.* Université de Liège, 2008.

[87] P. Aguado-Puente, P. Garcia-Fernandez, and J. Junquera, "Interplay of couplings between antiferrodistortive, ferroelectric, and strain degrees of freedom in monodomain pbtio$_3$/srtio$_3$ superlattices," *Phys. Rev. Lett.*, vol. 107, p. 217601, Nov 2011.

[88] S. Froyen and A. Zunger, "Polarization fields and band offsets in gainp/gaas and ordered/disordered gainp superlattices.," *Applied Physics Letters*, vol. 68, no. 20, p. 2852, 1996.

[89] C. V. Ciobanu and C. Predescu, "Reconstruction of silicon surfaces: a stochastic optimization problem," *Phys. Rev. B*, vol. 70, p. 085321, Aug 2004.

[90] R. A. P. M. Oganov, Artem R.Martok, "Anisotropy of earth's d layer and stacking faults in the $MgSiO_3$ post-perovskite phase.," *Nature*, vol. 438, no. 7071, pp. 1142 – 1144, 2005.

[91] http://spglib.sourceforge.net.

[92] D. M. Ceperley and B. J. Alder, "Ground state of the electron gas by a stochastic method," *Phys. Rev. Lett.*, vol. 45, pp. 566–569, Aug 1980.

[93] H. J. Monkhorst and J. D. Pack, "Special points for brillouin-zone integrations," *Phys. Rev. B*, vol. 13, pp. 5188–5192, Jun 1976.

[94] P. Ghosez, E. Cockayne, U. V. Waghmare, and K. M. Rabe, "Lattice dynamics of $BaTiO_3$, $PbTiO_3$, and $PbZrO_3$: a comparative first-principles study," *Phys. Rev. B*, vol. 60, pp. 836–843, Jul 1999.

[95] P. Ghosez, D. Desquesnes, X. Gonze, and K. M. Rabe, "First-principles study of lattice instabilities in $Ba_xSr_{1-x}TiO_3$," *AIP Conf. Proc.*, vol. 535, no. 1, pp. 102–110, 2000.

[96] N. A. Pertsev and V. G. Koukhar, "Polarization instability in polydomain ferroelectric epitaxial thin films and the formation of heterophase structures," *Phys. Rev. Lett.*, vol. 84, pp. 3722–3725, Apr 2000.

[97] Y. L. Li, S. Y. Hu, Z. K. Liu, and L. Q. Chen, "Phase-field model of domain structures in ferroelectric thin films," *Appl. Phys. Lett.*, vol. 78, no. 24, 2001.

[98] O. Diéguez, K. M. Rabe, and D. Vanderbilt, "First-principles study of epitaxial strain in perovskites," *Phys. Rev. B*, vol. 72, p. 144101, Oct 2005.

[99] C. Bungaro and K. M. Rabe, "Epitaxially strained [001] $(PbTiO_3)_1(PbZrO_3)_1$ superlattice and $PbTiO_3$ from first principles," *Phys. Rev. B*, vol. 69, p. 184101, May 2004.

[100] C. Bungaro and K. M. Rabe, "Coexistence of antiferrodistortive and ferroelectric distortions at the $PbTiO_3$ [001] surface," *Phys. Rev. B*, vol. 71, p. 035420, Jan 2005.

[101] R. A. Evarestov, E. Blokhin, D. Gryaznov, E. A. Kotomin, and J. Maier, "Phonon calculations in cubic and tetragonal phases of $SrTiO_3$ a comparative LCAO and plane-wave study," *Phys. Rev. B*, vol. 83, p. 134108, Apr 2011.

[102] A. Antons, J. B. Neaton, K. M. Rabe, and D. Vanderbilt, "Tunability of the dielectric response of epitaxially strained $SrTiO_3$ from first principles," *Phys. Rev. B*, vol. 71, p. 024102, Jan 2005.

[103] Y. L. Li, S. Choudhury, J. H. Haeni, M. D. Biegalski, A. Vasudevarao, A. Sharan, H. Z. Ma, J. Levy, V. Gopalan, S. Trolier-McKinstry, D. G. Schlom, Q. X. Jia, and L. Q. Chen, "Phase transitions and domain structures in strained pseudocubic (100) $SrTiO_3$ thin films," *Phys. Rev. B*, vol. 73, p. 184112, May 2006.

[104] H. T. Stokes, B. J. Campbell, and D. M. Hatch, "Order parameters for phase transitions to structures with one-dimensional incommensurate modulations," *Acta Crystallogr. Sect. A*, vol. 63, pp. 365–373, Jul 2007.

[105] http://stokes.byu.edu/iso/isotropy.php.

[106] See the Supplementary materials for Wyckoff positions.

[107] We have to know that in average it requires 200 loops for the structural optimization if one relaxes the 2:2 PTO/STO from a random configuration, with the wall clock time 18 hours on 16 cores of x86-64 AMD Opteron. With the same computer resources, the computation cost for the ones with lowest symmetry, such as Cm and Pc, in the stacking approach, is less than 4.2 hours for the same precision. The reduced computation time shows the importance of a reasonable initial configuration, and this advantage will be even amplified for large superlattices and high-throughput studies.

[108] R. F. Berger, C. J. Fennie, and J. B. Neaton, "Band Gap and Edge Engineering via Ferroic Distortion and Anisotropic Strain: The Case of $SrTiO_3$," *Phys. Rev. Lett.*, vol. 107, p. 146804, Sep 2011.

[109] F. Wang, I. Grinberg, and A. M. Rappe, "Band gap engineering strategy via polarization rotation in perovskite ferroelectrics," *Appl. Phys. Lett.*, vol. 104, no. 15, p. 152903, 2014.

[110] H.-T. Kim, B.-G. Chae, D.-H. Youn, G. Kim, K.-Y. Kang, S.-J. Lee, K. Kim, and Y.-S. Lim, "Raman study of electric-field-induced first-order metal-insulator transition in VO_2-based devices," *Appl. Phys. Lett.*, vol. 86, no. 24, p. 242101, 2005.

[111] Z. Yang, C. Ko, and S. Ramanathan, "Oxide electronics utilizing ultrafast metal-insulator transitions," *Ann. Rev. Mater. Res.*, vol. 41, no. 1, pp. 337–367, 2011.

[112] B. Chamberland, "Preparation and properties of $SrCrO_3$," *Solid State Commun.*, vol. 5, no. 8, pp. 663 – 666, 1967.

[113] A. C. Komarek, T. Möller, M. Isobe, Y. Drees, H. Ulbrich, M. Azuma, M. T. Fernández-Díaz, A. Senyshyn, M. Hoelzel, G. André, Y. Ueda, M. Grüninger, and M. Braden, "Magnetic order, transport and infrared optical properties in the $ACrO_3$ system (A = Ca, Sr, and Pb)," *Phys. Rev. B*, vol. 84, p. 125114, Sep 2011.

[114] L. Ortega-San-Martin, A. J. Williams, J. Rodgers, J. P. Attfield, G. Heymann, and H. Huppertz, "Microstrain sensitivity of orbital and electronic phase separation in srcro$_3$," *Phys. Rev. Lett.*, vol. 99, p. 255701, Dec 2007.

[115] K.-W. Lee and W. E. Pickett, "Orbital-ordering driven structural distortion in metallic srcro$_3$," *Phys. Rev. B*, vol. 80, p. 125133, Sep 2009.

[116] Z.-L. Zhu, J.-H. Gu, Y. Jia, and X. Hu, "A comparative study of electronic structure and magnetic properties of $SrCrO_3$ and $SrMoO_3$," *Physica B*, vol. 407, no. 12, pp. 1990 – 1994, 2012.

[117] J.-S. Zhou, C.-Q. Jin, Y.-W. Long, L.-X. Yang, and J. B. Goodenough, "Anomalous electronic state in $CaCrO_3$ and $SrCrO_3$," *Phys. Rev. Lett.*, vol. 96, p. 046408, Feb 2006.

[118] J. Rondinelli and N. Spaldin, "Electron-lattice instabilities suppress cuprate-like electronic structures in $SrFeO_3/SrTiO_3$ superlattices," *Phys. Rev. B*, vol. 81, p. 085109, Feb 2010.

[119] M. Verissimo-Alves, P. García-Fernández, D. Bilc, P. Ghosez, and J. Junquera, "Highly confined spin-polarized two-dimensional electron gas in srtio$_3$/srruo$_3$ superlattices," *Phys. Rev. Lett.*, vol. 108, p. 107003, Mar 2012.

[120] G. Song and W. Zhang, "First-principles study on the phase diagram and multiferroic properties of $(SrCoO_3)_1/(SrTiO_3)_1$ superlattices," *Sci. Rep.*, vol. 4, APR 4 2014.

[121] N. A. Pertsev, A. G. Zembilgotov, and A. K. Tagantsev, "Effect of mechanical boundary conditions on phase diagrams of epitaxial ferroelectric thin films," *Phys. Rev. Lett.*, vol. 80, pp. 1988–1991, Mar 1998.

[122] T. Hashimoto, S. Ishibashi, and K. Terakura, "Jahn-teller distortion and magnetic structure in lamno$_3$: A first-principles theoretical study with full structure optimizations," *Phys. Rev. B*, vol. 82, p. 045124, Jul 2010.

[123] D. S. Ginley and C. Bright, "Transparent conducting oxides," *MRS Bulletin*, vol. 25, pp. 15–18, 8 2000.

[124] K. Ellmer, "Past achievements and future challenges in the development of optically transparent electrodes," *Nature Photonics*, vol. 6, pp. 808–816, DEC 2012.

[125] D. N. Basov, R. D. Averitt, D. van der Marel, M. Dressel, and K. Haule, "Electrodynamics of correlated electron materials," *Rev. Mod. Phys.*, vol. 83, pp. 471–541, Jun 2011.

[126] M. Gajdoš, K. Hummer, G. Kresse, J. Furthmüller, and F. Bechstedt, "Linear optical properties in the projector-augmented wave methodology," *Phys. Rev. B*, vol. 73, p. 045112, Jan 2006.

[127] P. Wissgott, J. Kuneš, A. Toschi, and K. Held, "Dipole matrix element approach versus peierls approximation for optical conductivity," *Phys. Rev. B*, vol. 85, p. 205133, May 2012.

[128] R. D. King-Smith and D. Vanderbilt, "Theory of polarization of crystalline solids," *Phys. Rev. B*, vol. 47, pp. 1651–1654, Jan 1993.

[129] R. Resta, "Macroscopic polarization in crystalline dielectrics: the geometric phase approach," *Rev. Mod. Phys.*, vol. 66, pp. 899–915, Jul 1994.

[130] D. Vanderbilt and R. King-Smith, "Electric polarization as a bulk quantity and its relation to surface charge," vol. 48, pp. 4442–4455, 1993.

[131] L. Bányai, P. Gilliot, Y. Z. Hu, and S. W. Koch, "Surface-polarization instabilities of electron-hole pairs in semiconductor quantum dots," *Phys. Rev. B*, vol. 45, pp. 14136–14142, Jun 1992.

[132] W. Wen, X. Huang, S. Yang, K. Lu, and P. Sheng, "The giant electrorheological effect in suspensions of nanoparticles," *Nat. Mater.*, vol. 2, pp. 727–730, Nov 2003.

[133] Y. Okada, M. Serbyn, H. Lin, D. Walkup, W. Zhou, C. Dhital, M. Neupane, S. Xu, Y. J. Wang, R. Sankar, F. Chou, A. Bansil, M. Z. Hasan, S. D. Wilson, L. Fu, and V. Madhavan, "Observation of dirac node formation and mass acquisition in a topological crystalline insulator," *Science*, vol. 341, no. 6153, pp. 1496–1499, 2013.

[134] C. Sgiarovello, M. Peressi, and R. Resta, "Electron localization in the insulating state: Application to crystalline semiconductors," *Phys. Rev. B*, vol. 64, p. 115202, Aug 2001.

[135] X. Wu, O. Diéguez, K. M. Rabe, and D. Vanderbilt, "Wannier-based definition of layer polarizations in perovskite superlattices," *Phys. Rev. Lett.*, vol. 97, p. 107602, Sep 2006.

[136] A. A. Soluyanov and D. Vanderbilt, "Computing topological invariants without inversion symmetry," *Phys. Rev. B*, vol. 83, p. 235401, JUN 2 2011.

[137] M. Taherinejad, K. F. Garrity, and D. Vanderbilt, "Wannier center sheets in topological insulators," *Phys. Rev. B*, vol. 89, p. 115102, Mar 2014.

[138] N. Marzari and D. Vanderbilt, "Maximally localized generalized wannier functions for composite energy bands," *Phys. Rev. B*, vol. 56, pp. 12847–12865, Nov 1997.

[139] J. D. Joannopoulos and M. L. Cohen, "Intrinsic surface states of (110) surfaces of group iv and iii-v semiconductors," *Phys. Rev. B*, vol. 10, pp. 5075–5081, Dec 1974.

[140] J. Bennetto and D. Vanderbilt, "Semiconductor effective charges from tight-binding theory," *Phys. Rev. B*, vol. 53, pp. 15417–15420, Jun 1996.

[141] N. Marzari, A. A. Mostofi, J. R. Yates, I. Souza, and D. Vanderbilt, "Maximally localized wannier functions: Theory and applications," *Rev. Mod. Phys.*, vol. 84, pp. 1419–1475, Oct 2012.

[142] G. Valdrè, "Electric force microscopy," *Imaging & Microscopy*, vol. 8, no. 3, pp. 44–46, 2006.

[143] D. Wolf, H. Lichte, G. Pozzi, P. Prete, and N. Lovergine, "Electron holographic tomography for mapping the three-dimensional distribution of electrostatic potential in III-V semiconductor nanowires," *Applied Physics Letters*, vol. 98, no. 26, p. 264103, 2011.